Production of polyanionic clusters in ion traps

I n a u g u r a l d i s s e r t a t i o n

zur

Erlangung des akademischen Grades eines

Doktors der Naturwissenschaften
(Dr. rer. nat)

der

Mathematisch-Naturwissenschaftlichen Fakultät

der

Universität Greifswald

vorgelegt von

Steffi Bandelow

Greifswald, 05. Oktober 2023

Dekan:	Prof. Dr. Gerald Kerth
1. Gutachter:	Prof. Dr. Lutz Schweikhard
2. Gutachter:	Prof. Dr. Bernd von Issendorff
Tag der Promotion:	05. Januar 2024

Contents

List of figures

Nomenclature

AC ..... alternating current

C ..... correction electrode

DC ..... direct current

EC ..... endcap electrode

PT ..... Penning trap

RE ..... ring electrode

δ ..... electron spill-out

ϵ_0 ..... vaccuum permittivity

Φ ..... trapping potential

$\eta = x, y, z$ cartesian coordinates

$\nu_{\mathrm{r,z}}$ ..... ion motional frequencies

ξ ..... time related substitution parameter

ρ_{em} ..... electron emission rate

τ ..... cluster lifetime for $T \neq 0\,\mathrm{K}$

τ_0 ..... cluster lifetime for $T = 0\,\mathrm{K}$

$\omega_{\pm}, \omega_{\mathrm{c}}, \omega_{\mathrm{r}}, \omega_{\mathrm{z}}$ angular frequencies of ion motions

Ω ..... angular frequency of the radiofrequency guiding signal

a_η ..... storage parameter

$b_{\mathrm{r,z}}$ ..... order of radial and axial instabilities, $b_{\mathrm{r,z}} \in \mathbb{N}_0$

B ..... magnetic field

c ..... order of Fourier component, $c \in \mathbb{N}_0$

d ..... duty cycle

d_{PT} ..... geometry parameter of a Penning trap

e ..... elementary charge

E ..... electron energy

E_{C} ..... cluster energy

EA ..... electron affinity

$f(t)$ ..... digital signal

FE ..... temperature dependent field emission

g ..... running index, $g \in \mathbb{Z}$

h ..... Planck constant

$\hbar$ ..... reduced Planck constant

j ..... $0 \leq j < 1$, $j \in \mathbb{R}$

k ..... order of motional frequency, $k \in \mathbb{Z}$

k_{B} ..... Boltzmann constant

L ..... probability of thermal excitation

m ..... mass

m_{e} ..... electron mass

M ..... cluster mass

M_c ..... magnitude of Fourier components

n ..... cluster size

$n_{\mathrm{app},\tau}$ .... lifetime dependent appearance size

n_{min} ..... minimum cluster size

P ..... electron tunnelling probability

Q ..... ion charge

r_0 ..... minimum distance between trap centre and radial electrode

$r, r_1, r_2 \ldots$ distances / radial direction

R ..... cluster radius

R_{WS} ..... Wigner-Seitz radius

$S(t)$ ..... Fourier series

t ..... time

T ..... temperature

T_Ω ..... period of radiofrequency guiding signal

T_0 ..... 0 V duration of 3-state digital radiofrequency guiding signal

T_{H} ..... high-phase duration of digital radiofrequency guiding signal

U_0 ..... amplitude of the DC trapping voltage

V_0 ..... amplitude of the harmonic radiofrequency trapping voltage

V_{C} ..... Coulomb potential

$V_{\mathrm{C,max}}$ ... maximum of the Coulomb potential

V_{R} ..... amplitude of the digital radiofrequency trapping voltage

W ..... work function

z ..... charge state / axial direction

z_{η} ..... storage parameter

z_0 ..... minimum distance between trap centre and axial electrodes

1 Introduction

Atomic clusters are ensembles composed of a finite number of atoms. Their cluster size, defined by the number of constituents, typically ranges from a few atoms to several thousands [1, 2]. They are distinguished by the types of atomic bonds [3, 4] and investigated within different environments [3, 5–7]. However, even for clusters of the same type in the same environment, their properties are dependent on their geometric and electronic structures, which in turn vary with the cluster size and charge state [8]. This gives rise to an extensive field of research with numerous free parameters. Therefore, the present work focuses only on a small subset of that area, specifically the investigation of charged metal clusters in the gas phase.

Singly charged metal gas-phase systems can be reliably produced for an extended cluster size range by a variety of sources [1, 4]. Thus, their cluster-size dependent key characteristics as for example the electronic [9–12] and geometric [13–15] structure as well as fragmentation behaviour with respect to collisions and laser-irradiation [16–18] have been central aspects of cluster research. Nevertheless, an equally substantial change in the cluster properties can be observed when changing the charge state [19–21].

Generating highly charged systems in the gas phase, however, presents a significant technical challenge and is feasible only within specific boundaries of cluster size or for a restricted duration as increasing Coulombic forces affect the cluster stability [22]. Beyond these boundaries, highly positively charged systems experience spontaneous Coulomb explosion, fission or the evaporation of charged monomers to decrease their charge-to-size ratio [20, 23–26]. While negatively charged systems have the same options, they feature the additional and strongly competing decay pathway of electron emission [19, 27, 28].

In order to anticipate the stability of multiply negatively charged particles, criterions based on the Rayleigh limit [29] or the valence state parabola model [30] have been developed. Furthermore, computer-based calculations using for example the ab initio Hartree-Fock self-consistent field method [31], the shell correction method [28] or the density functional theory [32] have been conducted. While the Rayleigh limit is applicable to a wide range of charge states and cluster sizes and can predict the stability of polycations, it overestimates the stability of polyanions since it does not consider the decay pathway of electron emission [33]. Simultaneously, computer-based calculations as well as the valence state parabola model are typically constrained by the system size and therefore, computational effort, or limited to charge states of di- and trianions, as further experimental benchmark data is needed.

A reliable, experimental technique to produce polyanionic metal clusters in the gas phase has been to spatially overlap anionic clusters with low-energetic electrons for an extended period of time [34–38]. This so-called electron-bath technique is performed in a Penning trap [39–41], an ion trap device which limits the motion of both, the charged clusters and electrons to a confined volume by superposition of static magnetic and electric fields. Within the 12-T Penning trap at the ClusterTrap setup in Greifswald [42], the attachment of electrons to clusters of e.g. copper, gold, silver and aluminium has been probed as function of the cluster size [43, 44], reaching up to hexaanionic charge states in the case of gold clusters [37]. However, a functional relationship between the charge state and the appearance size, i.e., the minimum cluster size required to accommodate a certain number of electrons for a given duration, has not been experimentally investigated yet. As this knowledge is crucial to identify suitable cluster candidates for future research interests, this challenge will be addressed within the scope of this thesis.

Furthermore, it is intended to make polyanionic gas-phase systems accessible to a broader research community by developing an new production-technique apart from Penning traps. For this purpose, the use of radiofrequency ion traps [40, 41, 45] is especially suitable, which, as a versatile instrument with various designs and sizes, has continuously gained popularity across a variety of research fields [46–50].

The present work is divided into the following parts: The beginning focuses on the mathematical treatment of multiply negatively charged metal clusters, particularly on the significance of their Coulomb barrier. This property is inherent in all such systems and can critically influence the stability of polyanionic clusters (Article 1). Subsequently, a short introduction to the ClusterTrap setup is provided, which is used for all cluster measurements in this study. Thereafter, each of the two different ion trap types used for polyanion production is treated in detail:

Measurements utilising a 12-T Penning trap enabled the investigation of electron-attachment dynamics and the production of multiple new charge states of aluminium clusters. For the first time, the analysis of these datasets allows to observe a functional relationship between the charge states and their appearance sizes, which is then compared to theoretical considerations (Article 1).

Following that, the utilisation of radiofrequency ion traps is addressed, which predominantly employ AC-guiding fields for particle storage. Because simultaneous storage of clusters and electrons is not feasible in this trap type, its AC-guiding fields are modified in a two-stage process (Articles 2 and 3) to guide a low-energy electron beam through the trap in which monoanionic clusters are stored. This marked the basis of the first production of polyanionic clusters in radiofrequency ion traps (Article 4).

2 (Meta-) Stability of polyanionic metal clusters (Article 1)

In this work, it is assumed that a z-fold negatively charged metal cluster as for example Al_n^{-z} ($z > 1$) is a metal sphere and that its radius can be expressed as $R = R_{\mathrm{WS}} \cdot n^{1/3} + \delta$, where $R_{\mathrm{WS}} = 0.158\,\mathrm{nm}$ represents the element-specific Wigner-Seitz radius for aluminium [51], n denotes the cluster size, and δ accounts for some electronic spill-out [52]. To describe the stability of this cluster with respect to electron emission as summarised in [37, 38], the system is examined as a combination of two components: a precursor cluster of identical size, $Al_n^{-(z-1)}$, and a single electron. Due to the cluster's charge, the electron experiences the influence of a Coulomb potential, $V_{\mathrm{C}}(r)$, as schematically illustrated in the inset of Fig. 2.1:

$$V_{\mathrm{C}}(r) = \frac{e^2}{4\pi\epsilon_0} \cdot \left(\frac{z-1}{r} - \frac{R^3}{2r^2(r^2 - R^2)} \right) \quad , \tag{2.1}$$

where r is the distance between the centre of the cluster and the electron, e the elementary charge and ϵ_0 denotes the vacuum permittivity. Moreover, in the cluster ground state, this electron possesses a binding energy E, which is linked to the electron affinity EA of the $(z-1)$-fold charged cluster [53]:

$$E = -EA(z-1) = -\left(W - \left((z-1) + \frac{1}{2} \right) \frac{e^2}{4\pi\epsilon_0 R} \right) \tag{2.2}$$

and is dependent on the element-specific work function (e.g., $W_{\mathrm{Al}} = 4.28\,\mathrm{eV}$ [54]).

Based on the binding energy of the electron, three cases can be distinguished: If $E < 0$ with respect to the vacuum level, the electron is stably bound. On the contrary, if the electron binding energy exceeds the height of the Coulomb barrier, i.e. $E > V_{\mathrm{C,max}}$, the electron is not bound to the cluster. For all energies in between, $0 < E < V_{\mathrm{C,max}}$, the electron can exit the cluster by tunnelling through the Coulomb barrier. Similar to the alpha decay of radioactive nuclei, a metastable system is formed. The tunnelling probability P strongly depends on the barrier height and width $r_2 - r_1$ and, thus, the energy of the electron ($V_{\mathrm{C}}(r_1) = V_{\mathrm{C}}(r_2) = E$). A higher energy results in a smaller barrier width to be traversed, leading to a higher tunnelling probability [55], as approximated by the Wentzel-Kramers-Brillouin approach

$$P(E) = \exp\left[-\int_{r_1}^{r_2} \left(\frac{8m_{\mathrm{e}}}{\hbar} (V_{\mathrm{C}}(r) - E) \right)^{1/2} dr \right] \quad , \tag{2.3}$$

whereby m_e is the electron mass and r_1 describes the barrier distance from the centre of the cluster regarding an electron of energy E. Depending on this tunnelling probability, the lifetime τ_0 of a metastable, multiply negatively charged cluster can be determined in analogy to the decay lifetime in the context of an alpha decay [56, 57]. Here, the index 0 refers to the considered cluster temperature of 0 K, as any thermal excitation is neglected:

$$\tau_0(E) = \frac{2r_1(E)}{\sqrt{2E/m_e}\,P(E)} \ . \tag{2.4}$$

On the other hand, starting from a lifetime τ_0, this formula can also be used to calculate the minimum cluster size that allows to maintain a specific charge state for the chosen duration. Figure 2.1 displays these so-called appearance sizes of polyanionic aluminium clusters as a function of the square of the charge state z^2 for a variety of different lifetimes τ_0 (grey symbols). The dashed lines are included to guide the eye.

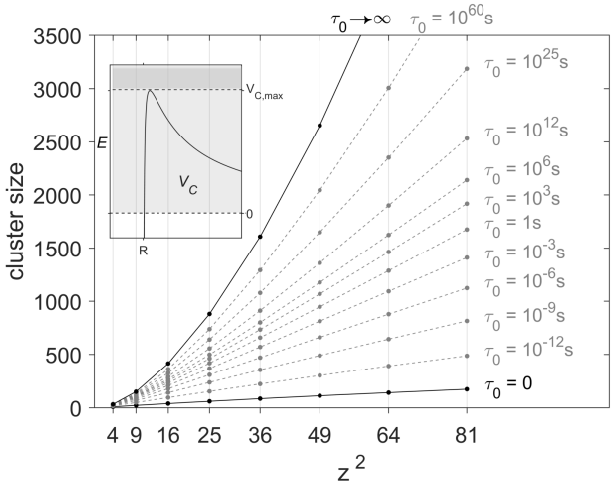

Figure 2.1: Appearance sizes of aluminium clusters (grey symbols) as determined from calculated lifetimes τ_0 (Eq.2.4) as a function of z^2. The limiting cases for $\tau_0 = 0$ and $\tau_0 \to \infty$ (black symbols) are highlighted. The inset shows a Coulomb barrier potential (Eq. 2.1). Adapted from [38].

The graph illustrates that larger clusters, at a given charge state, have a longer lifetime than smaller ones. Furthermore, at a constant lifetime, an increasing cluster size is required to reach the next higher charge state. When considering experimentally accessible lifetimes around $\tau_0 = 1\,\mathrm{s}$, the calculated sizes appear to exhibit a linear relationship in Fig. 2.1, suggesting an almost quadratic correlation to the charge state. However, examining the extreme case of $\tau_0 \to \infty$ determined by $E = |EA| = 0$ (upper black line), it becomes evident that the relationship is of a higher order. Conversely, in the limiting scenario of $\tau_0 = 0$ determined by $|EA| = V_{\mathrm{C,max}}$ (lower black line), the relationship is less than quadratic. This indicates a lifetime-dependent shift of the exponent in the relationship between the cluster appearance size and charge state, caused by a complex interplay between

cluster size, electron energy and tunneling probability through the Coulomb-barrier.

Up to this point, cluster temperatures of 0 K have been assumed. However, at the ClusterTrap setup (Chap. 3), which is used for experimental polyanion production, clusters are at room or even higher temperatures. Therefore, a probability of thermal excitation L of the electrons is introduced [58, 59], which, combined with the tunnelling probability, provides a measure of temperature-dependent field emission FE [37]:

$$L(T,E) = \ln\left(1 + \exp\left[-\frac{E + EA}{k_\mathrm{B}T}\right]\right) \quad \text{and} \tag{2.5}$$

$$FE(T,E) = \int_0^{V_{C,\max}} L(T,E) \cdot P(E) \cdot \mathrm{d}E \ . \tag{2.6}$$

With this, the electron emission rate ρ_em can be derived, providing an estimation for the lifetime τ of an excited, metastable, multiply negatively charged cluster.

$$\rho_\mathrm{em} = \frac{4\pi m_\mathrm{e} kT}{h^3} \cdot FE \ , \tag{2.7}$$

$$\tau = \frac{1}{4\pi R^2 \rho_\mathrm{em}} \ . \tag{2.8}$$

Figure 2.2 displays the calculated cluster appearance sizes for aluminium systems at a temperature of 600 K and a spillout of $\delta = 1$ Å, as these values have typically been estimated from fit routines to polyanion abundance curves of aluminium clusters [38].

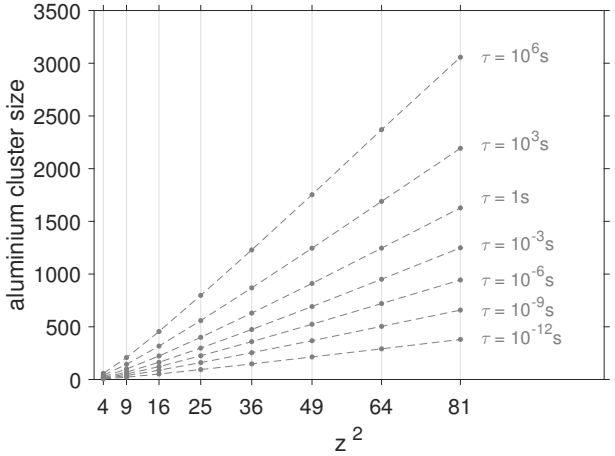

Figure 2.2: Appearance sizes of aluminium clusters at 600 K and with a spillout of $\delta = 1$ Å (grey symbols) as determined from calculated lifetimes τ (Eq. 2.8) as a function of z^2.

Again, a nearly quadratic relationship for lifetimes around 1 s can be observed. However, the previously recognised power-law transition across the family of curves is less pronounced and fewer lifetime curves can be represented for the same range of cluster sizes, as the curves are more seperated from each other. The higher temperature of the cluster results in the occupancy of higher-energy electron states, which is reflected in an increased tunnelling probability. Thus, a cluster of the same size and charge has a shorter lifetime at 600 K compared to 0 K. To achieve the same lifetime, the cluster needs to consist of more atoms. The introduction of a spillout reduces this effect.

In summary, the appearance of a polyanionic cluster is influenced not only by element-specific parameters such as the work function and Wigner-Seitz radius. Depending on the cluster size, its appearance is particularly determined by its metastability with respect to electron emission. When conducting experimental investigations of appearance sizes, the temperature of a cluster, serving as a measure of its internal excitation, must also be taken into account.

3 ClusterTrap setup

Measurements regarding the production and investigation of polyanions were conducted at the ClusterTrap experiment in Greifswald, which has undergone continuous development since the 1990s [42, 60–63]. The present configuration, comprising a cluster source with multiple ion traps (Fig. 3.1), has been specifically designed to investigate charged gas-phase particles and their interactions with light, neutral gases, and electrons in a vacuum surrounding.

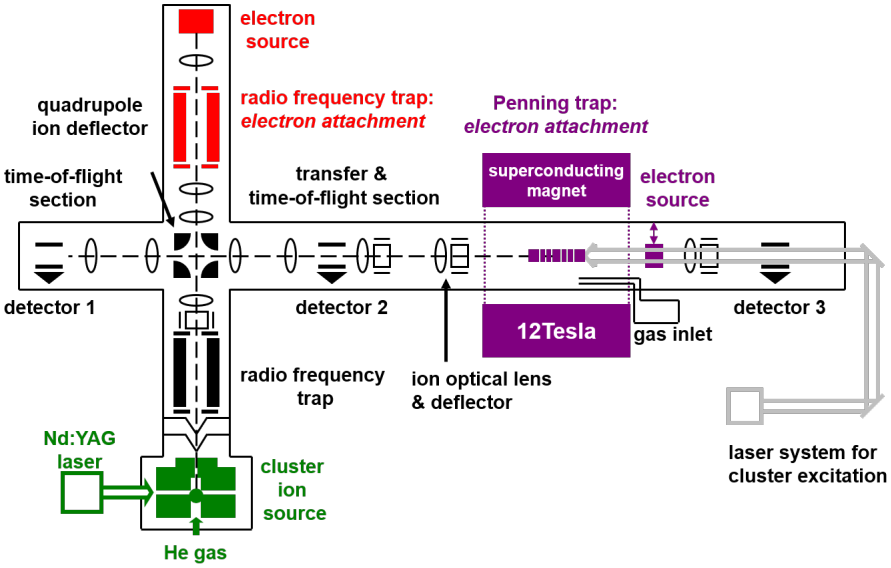

Figure 3.1: Schematic of the ClusterTrap setup. Adapted from [42].

Metallic mono-anionic clusters are produced using a laser vaporisation source [64], as depicted in Fig. 3.1 (green). The process involves directing a laser pulse onto the surface of a metal wire, leading to the evaporation of material. Subsequently, the evaporated atoms aggregate into clusters within an introduced helium gas-pulse, which also accelerates the clusters towards the source exit. The emitted clusters are than transferred to and captured in the first radiofrequency ion trap.

Within the first radiofrequency ion trap, clusters produced by multiple consecutive laser pulses are accumulated and bunched, prior to being transferred to either the Penning trap (Fig. 3.1, purple) or a second radiofrequency ion trap (Fig. 3.1, red). In the vicinity to both of these traps, electron sources are installed which can provide electrons for in-trap electron-cluster interactions. To identify interaction effects, all clusters are subsequently ejected from the used trap towards a microchannel-plate detector with a conversion dynode for time-of-flight analysis (e.g. detector 1, Fig.

3.1).

A measurement cycle as this is iterated multiple times to enhance ion count statistics and mitigate fluctuations in the monoanion source signal. Due to the limited resolving power of the time-of-flight detection of ≈ 100, the measured abundance spectra typically contain ion signals with a full-width-half-maximum signal-distribution bigger than a single cluster size. Therefore, investigated cluster sizes are given with uncertainties throughout the text. The next chapters provide an overview of the general operation of both ion-trap types and the production of polyanions within them.

4 Polyanions in Penning traps (Article 1)

A superposition of static magnetic and electric fields is used for a three-dimensional confinement of charged particles in a Penning trap [39]. While the homogeneous magnetic field B restricts the ion motion in the radial plane, the axial confinement is enabled by a quadrupolar electric field, the polarity of which also determines whether positively or negatively charged particles can be trapped. The electric field causes the particles to oscillate axially with the angular frequency ω_z

$$\omega_z = \sqrt{\frac{Q \cdot U_0}{M \cdot d_{PT}^2}} \quad , \tag{4.1}$$

which depends on the trap-geometry parameter d_{PT} , the axial trapping voltage U_0, the mass of the cluster M, and the cluster charge $Q = z \cdot e$. In an undisturbed cyclotron motion, charged particles move with the cyclotron frequency $\omega_c = QB/M$. However, the combination of the magnetic and electric fields results in a radial motion that involves both cyclotron motion with a reduced cyclotron frequency (ω_+) and magnetron motion with a magnetron frequency (ω_-)

$$\omega_\pm = \frac{\omega_c}{2} \pm \sqrt{\frac{\omega_c^2}{4} - \frac{\omega_z^2}{2}} \quad . \tag{4.2}$$

From the requirement that the square root term of Equation 4.2 is positive, the M/Q storage limit of a single particle in a Penning trap can be directly derived utilising Equation 4.1:

$$\frac{M}{Q} \leq \frac{B^2 \cdot d_{PT}^2}{2U_0} \quad . \tag{4.3}$$

It is crucial to note that for a given charge state in Penning traps, only an upper mass limit exists. Particles of all masses can be stored, individually or collectively, up to this limit.

The Penning trap at the ClusterTrap setup consists of a series of cylindrical electrodes in a homogeneous 12 -T magnetic field [42]. Fig. 4.1a, top, shows an axial cross-section of the electrode geometry. There are four endcap electrodes on each side (EC1-8) surrounding a central ring electrode (RE) where the stored ions reside. Correction electrodes (C1-4) between the ring and the endcap electrodes allow for adjustments to form a nearly harmonic potential (Fig 4.1a, bottom). The axial trapping depth of this arrangement is ca. $0.93 \cdot U_0$ and the trap parameter $d_{PT} \approx 26.65\,\text{mm}$ [42].

In order to test the storage limit, the maximum cluster-size of monoanionic aluminium clusters that could be stored at trapping voltages of $U_0 = 80\,\mathrm{V}$, $90\,\mathrm{V}$, and $100\,\mathrm{V}$ is determined (Fig. 4.1b in black, blue and red, respectively). The measured storage limits of approximately 1720(12), 1540(10), and 1440(10) aluminium atoms per cluster average at 75 % of the theoretical expectation, calculated using the atomic mass of aluminium $m_{\mathrm{Al}} = 26.98\,\mathrm{amu}$. This behaviour may result from two factors: deviations from the harmonic potential due to the cylindrical trap design and space charge effects caused by simultaneously storing multiple particles, which alter the effective trapping depth.

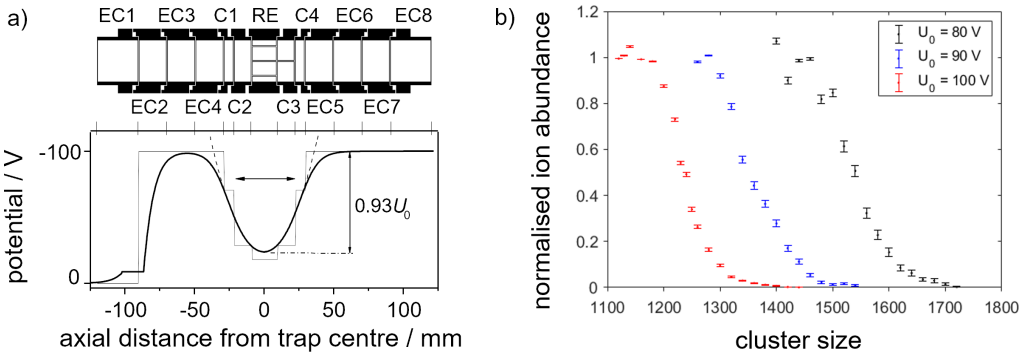

Figure 4.1: a) Axial cross section of the Penning trap electrodes at ClusterTrap (top) and the storage potential (bottom), both adapted from [42]. b) Ion abundance of monoanionic aluminium clusters as a function of the cluster size for Penning-trap voltages 80 V, 90 V, and 100 V in black, blue and red, respectively.

Within the trap, ion motions are influenced by the admittance of argon buffer gas, resulting in damping of both the axial and cyclotron motional amplitudes. Simultaneously, the radius of magnetron motion is increased. The splitting of the central ring electrode (RE), as indicated in Fig. 4.1a, is utilised for the application of an alternating quadrupolar field at the cyclotron angular frequency (ω_c) corresponding to the cluster size of interest. This radial excitation leads to a conversion between the radial motions [65]. If the conversion from magnetron to cyclotron motion and the cooling via buffer gas occur faster than the expansion of the magnetron motion, it results in the centring of a desired ion species [66].

4.1 Electron bath

The electron-bath technique is a method of simultaneous storage of anionic clusters and electrons in a Penning trap [34–38]. Initially, monoanionic clusters of a specific size or with minimal size distribution are selected and centred by radial excitations in an argon buffer-gas environment within the Penning trap. Subsequently, an electron beam with a kinetic energy of typically 60 eV is directed through the trap along the magnetic field axis for a duration of 20 ms. Along its path, the electron beam ionises buffer-gas atoms, thus producing secondary electrons with various energies

depending on their position of origin. While the positively charged argon ions immediately exit the trap due to their charge sign, secondary electrons with energies up to the typically used trapping depth of 23 eV remain trapped ($U_0 = 25$ eV), which can then interact with stored clusters to form multiply negatively charged particles. The time interval between the end of the electron beam passing through the trap and the ejection of the stored particles is referred to as the electron-bath duration.

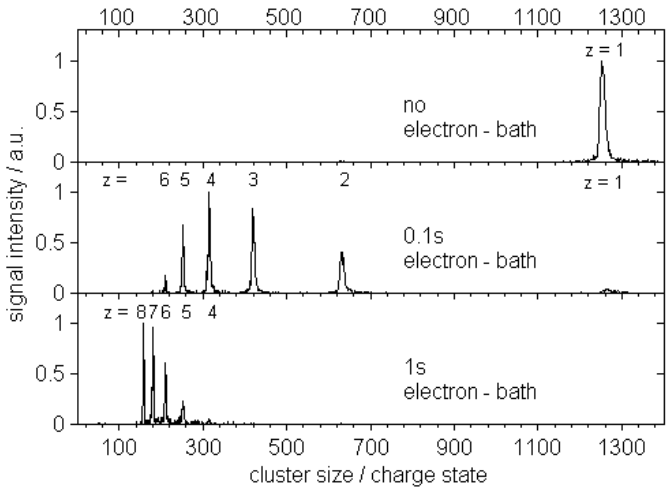

Figure 4.2: Abundance spectra of negatively-charged aluminium clusters $Al^{-z}_{1250\pm8}$ without (top), after an electron-bath of 0.1 s (centre) and 1 s (bottom). Figure adapted from [38].

The upper diagram in Figure 4.2 presents a reference abundance spectrum of size-selected $Al^{-1}_{1250\pm8}$ clusters. Since there is no interaction between the clusters and electrons, higher charge states are not detected. As with every subplot, the spectrum is normalised to the height of its most abundant peak.
For the middle part of Figure 4.2, the monoanionic clusters are subjected to a 0.1s electron-bath. Due to electron attachment, the abundance of monoanions in this spectrum is significantly reduced (down to approximately 2 %), while higher charge states up to $z = 6$ are detected. The highest relative abundance is observed for $z = 4$, with a value of 31 %.
Finally, the bottom diagram of Figure 4.2, displays a spectrum after exposing the clusters to an electron-bath duration of 1 s. In this case, mono-, di-, and trianions are no longer detected. While the peak of the $z = 8$ signal is the highest, its relative abundance of 29 % is slightly lower than that of the charge state, $z = 7$, which has a relative abundance of 33 %. Overall, the application of a specific electron-bath duration can lead to a dominant formation of a specific range of charge states.

4.2 Evolution of charge states

It has been observed in Fig. 4.2, that the distribution of charge states formed in the electron bath depends on the duration of the electron bath. To examine this relationship more closely, the interaction time between clusters and electrons was systematically varied. Figure 4.3 illustrates the progression of polyanion abundances as a function of electron-bath duration up to 10 s for exemplary cluster sizes between 700 and 1250 atoms. The abundance of each charge state at a specific electron-bath duration is normalised relative to the sum of all signals in the corresponding mass spectrum. Solid lines are implemented for an enhanced visibility of trends. They represent moving averages over five data points.

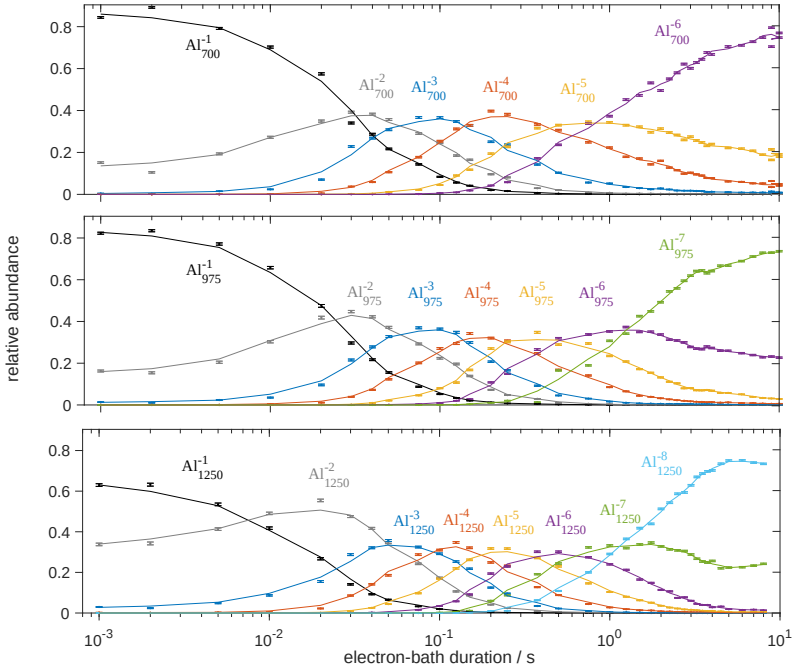

Figure 4.3: Ion abundance of (poly)anionic clusters as a function of the electron-bath duration of the cluster sizes $n = 700 \pm 5$ (top), 975 ± 6 (centre), and 1250 ± 8 (bottom). For clarity, moving averages of five data points are added as solid lines. The bottom figure is taken from [38].

In general, longer interaction times between electrons and cluster ions lead to the formation of higher negative charge states until a cluster-size dependent maximum is reached. Concurrently, the abundance of lower charge states decreases due to ongoing conversions. As the increase of each abundance curve corresponds to the decrease of the preceding charge state, a sequential electron attachment process is indicated.

As previously observed [67, 68], the electron attachment dynamics extend over several seconds and surpass the measured range of electron-baths durations for

$n = 700 \pm 5$ and 975 ± 6. However, for the cluster size 1250 ± 8, the production of octaanions stagnate for durations that exceed 4 s, as observed by the saturation of both, the octaanion signal, and the heptaanion signal as respective charge state. Possible reasons for this behaviour are loss of trapped particles, ions or electrons, electron energies that are insufficient for electron attachment, or a combination of multiple factors. However, a decrease in the absolute numbers of detected ions at extended electron-bath durations has not been observed, which also justifies its representation as a relative abundance in Fig. 4.3. Besides, a loss of electrons from the electron bath to the point of the stagnation of polyanion formation after an interaction time of 4 s is unlikely, as electron attachment is observed for up to 10 s under identical electron-bath conditions to other cluster sizes (Fig. 4.3 top and middle subplot). Furthermore, it is known that electron energies decrease over time while stored in the Penning trap [68, 69], which would halt the electron attachment process, as soon as the electrons cannot overcome the Coulomb barrier heights of the clusters anymore (Sec. 2). These limits are given by 3.7 eV, 4.0 eV and 4.3 eV to form Al_{700}^{-6}, Al_{975}^{-7} and Al_{1250}^{-8}, respectively (Sec. 2). As the production of the octaanionic system requires the highest electron energy, it would be the first attachment process to stop.

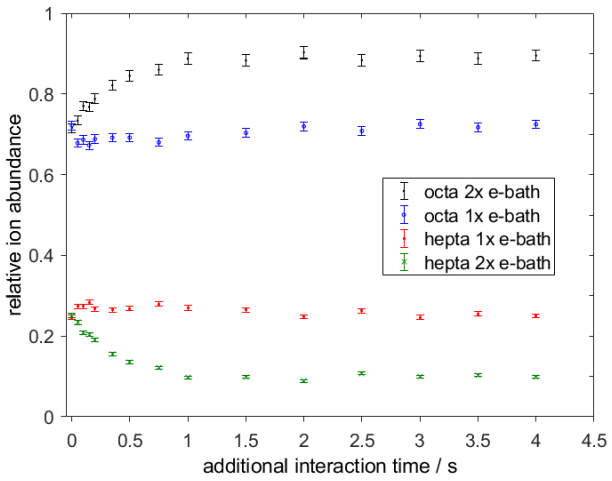

Figure 4.4: Ion abundances of hepta- and octa-anionic clusters of $n = 1250 \pm 8$ with (green and black marker) or without (red and blue marker) the application of a 2nd electron bath after a previous electron-cluster interaction time of 4 s.

To test if the production of octaanions can be restarted, a second electron bath was initiated for Al_{1250} after a first electron-cluster interaction time of 4 s (Fig. 4.4, black and green marker). In contrast to the scenario with only one electron bath (blue and red marker), the relative abundance of octaanions can indeed be further increased from 70 % to 90 %, whereas the abundance of hepta-anionic clusters decreased by the same extent. While it cannot be determined whether the higher number of electrons or their higher energy lead to this effect, the stagnation of the octaanion

production can be traced to the properties of the electron-bath. Additionally it should be noted, that even after the application of a second electron bath, no higher charge state is produced, as the appearance of aluminium clusters with nine excess electrons requires a cluster size beyond $n = 1250$ (Sect. 4.3).

Another observation from the analysis of Fig. 4.3 is an accelerated dynamic of electron-attachment processes with increasing cluster size. This is particularly evident at the very beginning of the electron-bath duration. Here, the initial ion-abundance distribution is determined by the 20 ms long electron pulse prior to the interaction time, during which attachments already occur. The relative dianion abundance at $n = 700 \pm 5$ at the start of the electron-bath period is approximately 18 %, but this ratio almost doubles to 35 % for $n = 1250 \pm 8$. Albeit harder to observe due to the logarithmic scale, this effect also causes a shift of the moving averages of a certain charge state to shorter electron-bath durations when investigating bigger clusters. For example, the abundance maxima for tetraanions are reached at 250 ms, 200 ms, and 125 ms for $n = 700 \pm 5$, 975 ± 6, and 1250 ± 8 respectively.

This change in the attachment dynamic is presumably caused by the interplay of several factors. Firstly, as the cluster size increases, the potential height of the Coulomb barrier that the electron must overcome for the attachment decreases. Consequently, as the electrons of the electron bath have an energy distribution up to the trapping depth of the Penning trap (Sect. 4.1), a larger proportion of electrons within the electron bath becomes available for the attachment process. Simultaneously, as the number of atoms in the cluster increases, so does the number of degrees of freedom in which the cluster can distribute the energy of the attaching electron, thereby increasing the probability of polyanion formation. Lastly, with increasing cluster size, the minimum energy of the attached electron ($E = -EA$) decreases, reducing the tunneling probability of the excess electron and, as a result, increasing the clusters stability.
Based on the enhanced attachment-rates, the highest attainable charge state in Fig. 4.3 is approximately as abundant as its precursor after an interaction time of 1 s in all shown cases. This electron-bath duration is used for further investigations of polyanionic appearance sizes.

4.3 Lifetime-dependent appearance sizes

The first production of polyanionic metal clusters in a Penning trap was pioneered by A. Herlert and coauthors at the ClusterTrap setup using the element gold [70]. Thereafter, various elements and charge states have been examined [19, 28, 43, 71, 72]. Of particular relevance to this thesis is the investigation of polyanionic aluminium clusters, which started with the first observation of dianionic systems Al^{-2}_{34-80} produced in a 5-T Penning-trap setup [67]. These studies have been extended up to the fifth charge state in the following years [35, 36, 44]. However, due to the mass-to-charge limit of the 5-T Penning trap, the production of pentaanionic aluminium clusters were only possible in a two-step electron bath with an intermediate

increase of the trapping voltage [44]. Since then, the Penning trap at ClusterTrap has been upgraded to 12-T setup with a new trap-electrode design [42], shifting the mass-to-charge limit by a factor of ~ 20. With this improved trap configuration, the emergence of higher negative charge states has been investigated in this thesis, building upon the previously studied pentaanionic aluminium clusters.

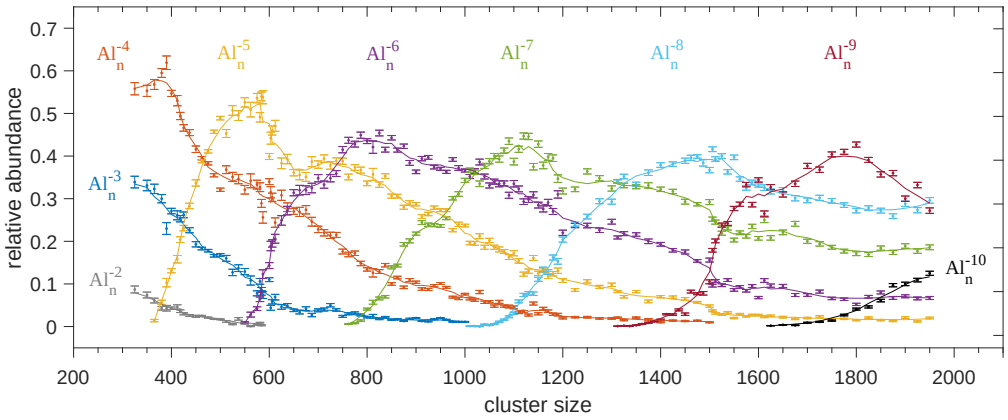

Figure 4.5: Relative abundances of polyanions of different charge states z as a function of cluster size after an interaction time of 1 s. Solid lines to guide the eye are moving averages over five data points. In the decreasing part of the curves data are shown for relative abundances above 1 %. Fig. taken from [38].

Figure 4.5 provides an overview of the polyanion abundance across the range of cluster sizes from 325 to 1950, as discussed in detail in [38]. The polyanion abundances of the observed charge states are normalised to the total number of detected ions. The trend in abundance of each charge state is represented by moving averages calculated over five data points (solid lines). For the smallest cluster size examined, n=325±4, only di-, tri-, and tetraanions were observed, with relative abundances of 9 %, 34 %, and 56 % respectively. Higher charge states appear one by one as soon as respective cluster-size limits, referred to as minimum cluster sizes (n_{min}), are reached. Beyond this value, the abundance of the polyanionic charge state increases with cluster size, as will be further discussed below. This trend is only reversed, when the next higher charge state is formed. For the largest cluster size investigated, $n = 1950 \pm 16$, charge states $z = 5 - 10$ are detected, with relative abundances of 2 %, 7 %, 18 %, 29 %, 27 %, and 13 %, respectively.

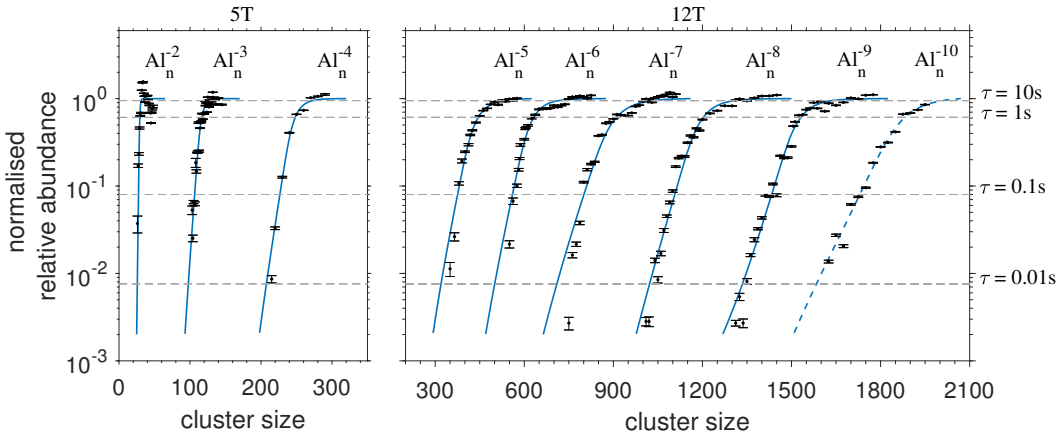

Figure 4.6: Log-scale representation of rel. abundances of charge states $z = 2 - 10$ as a function of the cluster size (black symbols), normalised to the saturation levels obtained from fits to the data (blue curves). Abundance data for $z = 2 - 4$ measured previously with a 5-T Penning-trap setup are reevaluated here. The dashed horizontal lines connect clusters of different size and charge state, but equal lifetime. Fig. adapted from [38].

For Fig. 4.6, the ascending regions of the curves in Fig. 4.5 are investigated using the temperature-dependent tunnel model as described in Sec. 2. This model is fitted to the polyanion abundance data (Fig. 4.6, blue curves) and thus assigns a lifetime to each relative abundance with respect to the saturation level. It becomes evident, that the increase of their abundance is strongly coupled to an enhanced polyanion meta-stability with respect to electron emission, ranging from approximately 10 ms to 30 ms for $n_{\min}$ and above 10 s in the saturation region. However, deca-anionic clusters are excluded from further analysis as their abundance did not reached saturation within the size range under investigation. In addition, previously at the ClusterTrap setup examined appearances of di- to tetra-anionic aluminium clusters are reevaluated [35, 36, 44, 67], resulting in a unique dataset of polyanion abundances in the appearance region spanning eight consecutive charge states.

Each horizontal line in Fig. 4.6 indicate clusters of different sizes and charge states, but sharing the same lifetime. These values have been used in Figure 4.7 (left), which displays the appearance sizes for di- to nonaanionic charge states of aluminium clusters for lifetimes of 0.1 s, 1 s and 10 s in blue, red and orange, respectively. In accordance with Chapter 2, the lifetime-dependent appearance sizes exhibit a systematic trend as function of their charge state. Additionally, it can be observed that for higher charge states, a larger cluster size range is required to cover the same lifetime interval. This behaviour is also evident in Figure 4.6, where the slope of the abundance curves become less steep as the charge state increases. This is reasonable since, in general, the addition of one atom to the cluster has a greater impact on cluster properties at smaller cluster sizes than in larger systems. Figure 4.7 (right) shows calculated appearance sizes of aluminium clusters with various

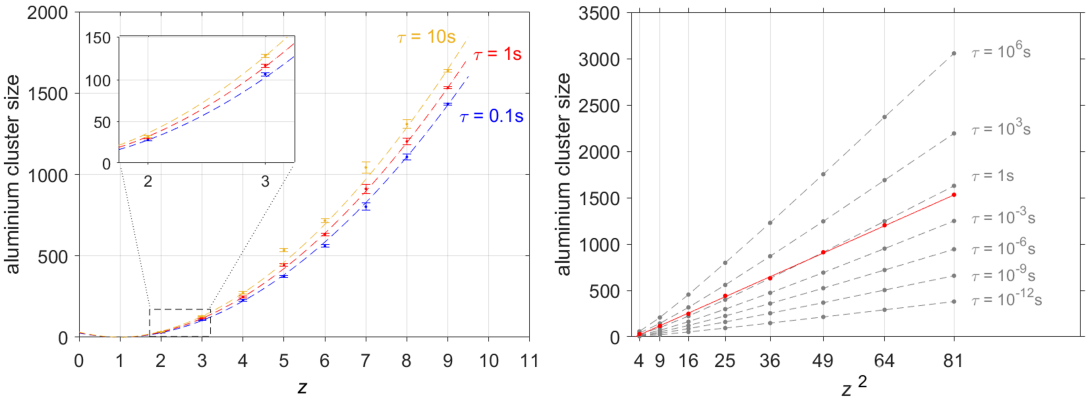

Figure 4.7: Left: Lifetime dependent appearance sizes $n_{\mathrm{app},\tau}$ as a function of the charge state z for $\tau = 0.1\,\mathrm{s}$ (blue), $1\,\mathrm{s}$ (red) and $10\,\mathrm{s}$ (orange), respectively. Dashed lines are fits to the data as discussed in [38]. Plot taken from [38]. Right: Calculated appearance sizes as function of z^2 as established in Chap. 2, Fig. 2.2. In red, experimental values for $\tau = 1\,\mathrm{s}$ are included.

lifetimes (grey), as already presented in Figure 2.2. In red, the experimentally determined appearance sizes for $\tau = 1\,\mathrm{s}$ have been added for comparison, revealing an overall agreement between experimental data and the model from Chapter 2.

To test if the model can be applied to metal clusters of other elements, lifetime-dependent appearance size calculations were examined using gold clusters, for which an experimental dataset of five polyanionic appearance sizes is available for comparison ($z = 2 - 6$ [37, 43]). Considering only the very similar Wigner-Seitz radii of both elements ($R_{\mathrm{WS,Al}} = 0.158\,\mathrm{nm}$ and $R_{\mathrm{WS,Au}} = 0.159\,\mathrm{nm}$ [51]), the model results for gold would hardly change. However, the difference in the work function ($W_{\mathrm{Al}} = 4.28\,\mathrm{eV}$ [54] and $W_{\mathrm{Au}} = 5.38\,\mathrm{eV}$ [73]) significantly impacts the binding energy (Eq. 2.2) and thus both, the tunneling probability of the excess electron (Eq. 2.3) and the lifetime of the polyanionic cluster (Eq. 2.8).
Fig. 4.8 illustrates the comparison between calculated lifetime-dependent appearance sizes (grey) and measured appearance sizes (red) of gold clusters. In the model, a temperature of $T = 485\,\mathrm{K}$ and a spillout of $\delta = 0.267\,\mathrm{Å}$ are used, as these values have been estimated on average from fit routines applied to polyanion abundance curves of gold cluster charge states $z = 4 - 6$ [37]. Similar to aluminium, curves of theoretical appearance sizes as a function of the charge state are observable for various lifetimes (grey lines). However, due to the increased work function of gold, the appearance sizes are significantly smaller, e.g., $n_{\mathrm{app},\tau=1\,\mathrm{s}} = 352$ and 630 for hexaanionic gold and aluminium clusters, respectively.

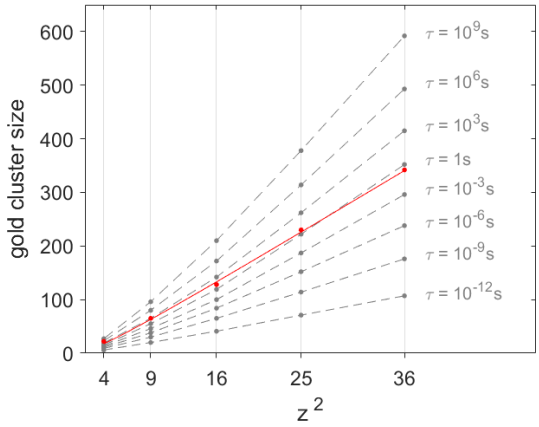

Figure 4.8: Calculated appearance sizes of gold clusters (grey) as a function of z^2 compared to experimental appearance sizes for $\tau = 1\,\mathrm{s}$ taken from [37] (red).

Comparing experimental and calculated values for a lifetime of $\tau = 1\,\mathrm{s}$ demonstrates a similar agreement for gold as it has been observed for aluminium clusters. Minor discrepancies between calculated and experimental values for gold are mainly noticeable at lower charge states and cluster sizes, where the experimental appearance sizes are above the calculated values. On an even smaller scale, these deviations can also be observed for aluminium and attributed to the assumptions used in the model, as for example that of a spherical shaped system, which is hardly applicable for small clusters. For large clusters within the investigated size range, the use of the model allows for reliable predictions of appearance sizes for different materials and charge states.

5 Polyanions in radiofrequency ion traps (Article 2-4)

Radiofrequency ion traps employ temporally oscillating potentials $\Phi(t)$ to confine charged particles [45, 74, 75]. The radiofrequency ion trap utilised in Sect. 5-5.1 is an independent setup, not included in ClusterTrap. Its configuration with a hyperbolic electrode design as depicted in Fig. 5.1 (left) can bind charged particles in three dimensions to the trap's centre by a quadrupolar trapping potential, applied between the ring- and endcap electrodes:

$$\Phi(x,y,z,t) = \frac{U_0 + V_0 \cdot cos(\Omega t)}{2(r_0^2/2 + z_0^2)} \, (x^2 + y^2 - 2z^2) \quad , \tag{5.1}$$

whereby $r_0 = 7\,\mathrm{mm}$ and $z_0 = 4.9\,\mathrm{mm}$ are the minimum distances between the trap's centre and the ring or the endcap electrodes, respectively. In addition to the harmonic alternating voltage of amplitude V_0 and angular frequency Ω, a DC voltage component of amplitude U_0 can be utilised to further influence the storage conditions. The equation of motion of a charged particle within a radiofrequency ion trap is described by the Mathieu equation

$$\frac{\mathrm{d}^2\eta}{\mathrm{d}\xi^2} + (a_\eta - 2q_\eta \, cos(2\xi))\eta = 0 \quad \text{with} \quad \eta = x, y, z \quad , \tag{5.2}$$

where $\xi = 0.5 \cdot \Omega t$ and the dimensionless storage parameters a_η and q_η are employed for particles of mass m and charge $Q = z \cdot e$ [41]:

$$a_\mathrm{z} = -2a_\mathrm{x,y} = -\frac{8\,Q\,U_0}{m(r_0^2/2 + z_0^2)\Omega^2} \quad , \quad q_\mathrm{z} = -2q_\mathrm{x,y} = \frac{4\,Q\,V_0}{m(r_0^2/2 + z_0^2)\Omega^2} \quad . \tag{5.3}$$

Describing a low-energetic ion in an ideal quadrupolar field, the combination of parameters a_η and q_η is sufficient to define the stability of an ions trajectory [75]. The boundaries between stable and instable conditions can be approximated using a power series expansion of the Mathieu's differential equation (Eq. 5.2) as performed by McLachlen [76]. For positive ions, this leads to a theoretical stability diagram as depicted using red lines and axes in Fig. 5.1, right. For negative ions, the stable region is equivalent, but inverted with respect to the $a_\eta = 0$ axis.
Additionally, a measured stability diagram is included into Fig. 5.1 (right) using greyscale values. For this measurement, argon ions Ar^+ are repeatedly created and stored using various combinations of amplitudes U_0 and V_0 (black axes) [77]. The number of ions detected for each combination of DC and AC amplitudes are normalised to the maximal detected ion number of all storage parameters.

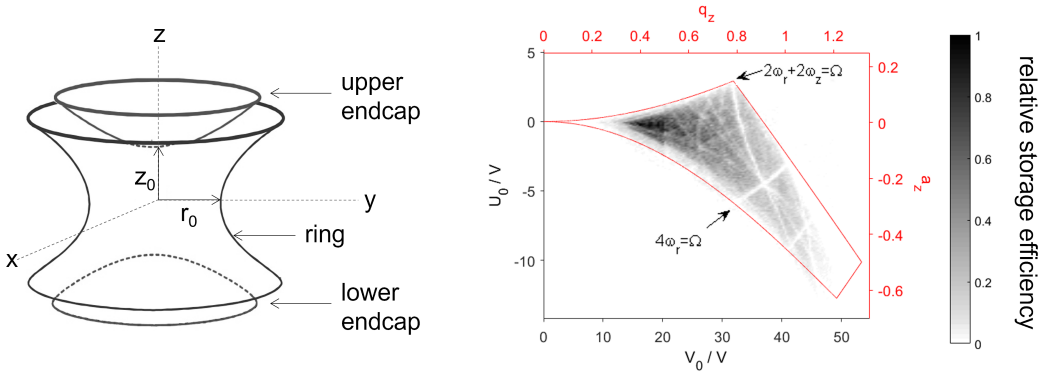

Figure 5.1: Left: Schematic of a radiofrequency ion trap with hyperbolic electrode design, consisting of a ring and two endcap electrodes. Right: Measured stability diagram of argon ions in a harmonically driven ion trap with $\Omega = 2\pi \cdot 450\,\mathrm{kHz}$ plotted as a function of guiding field voltages (black axes) and stability parameters (red axes). Red lines represent the theoretical borders of stability [76]. Two instability lines are marked. Both pictures taken from [77].

While theoretical predictions and measured values are in good agreement, white lines of reduced storage efficiency are observable throughout the diagram. These instability lines are caused by deviations of the trap potential from the ideal quadrupolar form and connected to the motional frequencies of trapped ions [41, 78]:

$$\omega_{\mathrm{k},\eta} = 2\pi\nu_{\mathrm{k},\eta} = (2k \pm \beta_\eta)\,\frac{\Omega}{2} \quad \text{with} \quad k = 0, \pm1, \pm2, \ldots \quad , \tag{5.4}$$

where β_η are functions of a_η and q_η only [79, 80]. The ion motions in x, y and z can be excited independently [81]. Nevertheless, due to the symmetry in the x- and y-planes, the radial motional frequencies have the same values and are summarised to $\omega_{\mathrm{k,r}}$. The measured instability lines occur, when the sum of integer multiples of the motional angular frequencies equals the angular driving field frequency, $b_\mathrm{r}\omega_\mathrm{r} + b_\mathrm{z}\omega_\mathrm{z} = \Omega$. In these cases ions can resonantly gain energy from the guiding field, increasing the amplitude of their trajectory up to ion loss [82, 83]. Two dominant lines are identified and labelled in Fig. 5.1 (right) as $2\omega_\mathrm{r} + 2\omega_\mathrm{z} = \Omega$ and $4\omega_\mathrm{r} = \Omega$.

When considering the radiofrequency ion trap for polyanion production, it must also be noted that in real experimental conditions, both a lower and an upper mass-to-charge limit exist for all storage parameters [41]. Thus, while particles with mass-to-charge ratios as low as electrons and as high as singly charged metal clusters with thousands of atoms can be individually stored in radiofrequency ion traps [38, 84], it is not possible to simultaneously store both species. This prevents the application of the electron-bath technique, as used in the Penning trap for generating polyanionic clusters. Instead, for a controlled polyanion production process, the guiding field of a radiofrequency ion trap must be modified in such a way that

one interaction partner can pass through the trap unhindered at specific, 0 V time-intervals in each cycle of the guiding field while the other remains stored within it [85, 86].

5.1 2- and 3-state digital ion trap

In order to allow for the implementation of extended time-intervals with a constant potential in each cycle of the guiding field, the harmonic AC voltages for ion storage are, in a first step, replaced by square wave voltages [87–90], as depicted in Fig. 5.2, left. The square wave, or digital, guiding field voltages are realised using voltage-switches replacing the resonance circuits, conventionally used for the generation of the harmonic AC-guiding voltages. In a beneficial manner, the use of voltage switches also allows an effortless change of the guiding-field frequency and thus, a change of the mass-to-charge range that can be stored. Since a modification of the guiding field always entails a change in the storage conditions, it is crucial to investigate these effects.

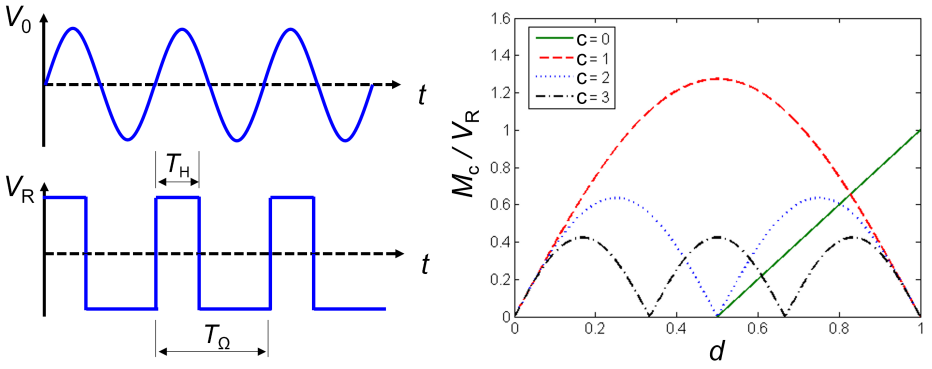

Figure 5.2: Left: Schematics of harmonic and digital guiding-field voltages. Right: Magnitudes of Fourier Components M_c of the digital driving voltages, normalised to V_R (adapted from [77]).

As for harmonically driven radiofrequency ion traps, storage parameters can be adjusted by the AC frequency Ω and voltage amplitude (now V_R) as well as by a DC voltage U_0. Furthermore, this signal waveform also allows for the manipulation of storage conditions through its duty cycle $d = T_\mathrm{H}/T_\Omega$, which represents the fraction of time the high phase T_H occupies within one period T_Ω of the signal (Fig. 5.2, bottom left).
Mathematically, the digital signal $f(t)$ can be described as

$$f(t) = \begin{cases} +V_R & for \quad gT_\Omega < t \leq gT_\Omega + T_\mathrm{H} \\ -V_R & for \quad gT_\Omega + T_\mathrm{H} < t \leq (g+1)T_\Omega \end{cases}, \tag{5.5}$$

where g is an integer ($g \in \mathbb{Z}$).
In order to compare the digital with a harmonic driving signal, a Fourier analysis is

conducted [77], revealing all harmonic components of the digital signal [91]:

$$\begin{aligned} S(t) &= \frac{A_0}{2} + \sum_{c=1}^{\infty} \left[A_c \, cos(c\,\Omega\, t) + B_c \, sin(c\,\Omega\, t) \right] \quad \text{with} \\ A_c &= \frac{1}{\pi} \int_0^{2\pi/\Omega} f(t) \cdot cos(c\,\Omega\, t)\ \Omega\ dt \quad \text{and} \\ B_c &= \frac{1}{\pi} \int_0^{2\pi/\Omega} f(t) \cdot sin(c\,\Omega\, t)\ \Omega\ dt \quad . \end{aligned} \tag{5.6}$$

A_c and B_c are the Fourier coefficients of order $c \in \mathbb{N}_0$, from which the magnitudes M_c of the Fourier components can be derived. For the square-wave signal in Eq. 5.5, the following results are obtained:

$$\begin{aligned} M_0 &= A_0/2 = (2d-1) \cdot V_{\mathrm{R}} \qquad\qquad\qquad\qquad \text{and} \\ M_c &= \sqrt{A_c^2 + B_c^2} = 4/c\pi \cdot |\sin(c\pi d)| \cdot V_{\mathrm{R}} \qquad \text{for} \quad c > 0 \quad . \end{aligned} \tag{5.7}$$

The magnitudes $M_c > 0$ of the first four Fourier components with $0 \leq c \leq 3$ are summarised in (Fig. 5.2, right). All magnitudes of Fourier components are a function of the duty cycle. For $d \neq 0.5$ an AC-voltage dependent DC component M_0 is generated by the guiding field (green line). The shown trend of M_0 continues for values below $d < 0.5$. However, for a better visibility of the higher orders, the diagram has been limited to positive Fourier-magnitude values.
A comparison of the first order Fourier magnitudes M_1 of a harmonic and digital driving signal with identical amplitudes $V_0 = V_{\mathrm{R}}$ for $d = 0.5$ reveals an increased amplitude of the digital signal component by a factor of $4/\pi \approx 1.27$ (maximum of red line). Additionally, a series of Fourier components with angular frequencies $c \cdot \Omega$ and $c > 1$ are embedded in the digital guiding signal, also potentially affecting the ion storage.

To investigate the influence of the modified guiding field, the stability diagram of argon ions in a digitally operated trap with a duty cycle of $d = 0.5$ has been measured (Fig. 5.3, left). Comparing it to the stability diagram measured using harmonic radiofrequency voltages (Fig. 5.1, right), identical structures are observed. These structures occur for digital AC voltage amplitudes, that are reduced by the factor $4/\pi$ compared to the harmonic case, i.e. when the magnitudes of the 1st order Fourier components of both guiding fields are equal. In fact, the measured stability diagram can be transformed into the harmonically known limits of the $a_{\mathrm{z}} - q_{\mathrm{z}}$ parameter-space (red lines in Fig. 5.3, left) by only replacing the harmonic radiofrequency amplitude V_0 with the first order Fourier magnitude M_1 of the digital guiding voltages in the q_{z} calculation, as an influence of the higher-order Fourier components $c > 1$ is not visible.
For duty cycles $d \neq 0.5$ the additional DC component of the AC voltage signal, given by M_0, results in a rotation of the stability diagram in the $U_0 - V_{\mathrm{R}}$ region with respect to the point of origin and needs to be considered in the a_{z} calculation

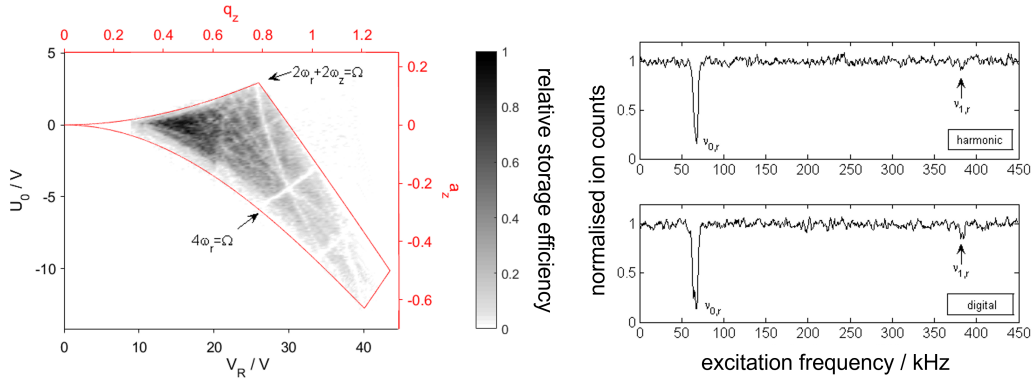

Figure 5.3: Left: Measured stability diagram of argon ions in a digitally driven ion trap with $d = 0.5$ and $\Omega = 2\pi \cdot 450\,\mathrm{kHz}$, plotted as a function of guiding field voltages (black axes) and stability parameters (red axes). Red lines represent the theoretical borders of stability [76]. Two instability lines are marked. Right: Ion counts as a function of excitation frequency for argon ions confined by harmonic (top) and digital $d = 0.5$ (bottom) trapping fields ($a_z, q_z = 0.00, 0.81$), respectively. Both pictures taken from [77].

as described in [77]:

$$a_{z,\mathrm{DIT}} = -\frac{8\,Q\,(U_0 + M_0)}{m(r_0^2/2 + z_0^2)\Omega^2} \quad , \quad q_{z,\mathrm{DIT}} = \frac{4\,Q\,M_1}{m(r_0^2/2 + z_0^2)\Omega^2} \quad . \tag{5.8}$$

To ensure that the higher-order Fourier components do not have a significant impact on ion storage, the radial motional frequencies are measured [92] by radial dipolar excitation in a harmonically and digitally operated radiofrequency ion trap. For this comparison, the same setup is used, driven by guiding fields of 450 kHz, without DC-component. The magnitude of the first order Fourier components are matched by operating the digitally driven ion trap at $V_\mathrm{R} = V_0/(4/\pi)$ for a duty cycle of $d = 0.5$ and thus, applying the same values $(a_{z,\mathrm{DIT}}; q_{z,\mathrm{DIT}}) = (0; 0.81)$. To enable the radial dipolar excitation of the stored ions, a feature of the setup is utilised: a segmentation of the ring-electrode, which is divided into four equal parts. This allows the generation of radial dipolar and quadrupolar fields. For the employed dipolar excitation, two adjacent segments received an identical AC excitation signal of fixed frequency for 10 ms during the storage time. The remaining two segments receive the signal with a phase shift of 180 °. At the end of the storage time, the remaining ions are ejected from the trap and detected. Subsequently, the measurement is repeated for other excitation frequencies to obtain an excitation spectrum (Fig. 5.3, right).
If the frequency of the excitation signal matches the motional frequency of the stored ions in the radial direction, energy absorption and an increase of the amplitude of the ion trajectory occurs leading to ion loss [77, 82, 83, 93]. In that case, a reduced number of particles is detected. Both for harmonically and digitally operated ion traps, two dips in the ion count rate at the 0th and 1st order motional frequencies

$\nu_{0,r} \approx 67\,\mathrm{kHz}$ and $\nu_{1,r} = \Omega/2\pi - \nu_{0,r} \approx 383\,\mathrm{kHz}$ are detected (compare Eq. 5.4). Additionally, the relative reduction in the ion signal is comparable in both measurements, further confirming the equality of the guiding field components relevant for ion storage.

The use of digital driving signals as described in Eq. 5.5, however, was only the first step in generating suitable AC-voltage pattern for polyanion production in radiofrequency ion traps. In a second step, the guiding signal is further modified by incorporating 0 V time-intervals T_0, allowing for controlled passage of an interaction partner through the trap [94].

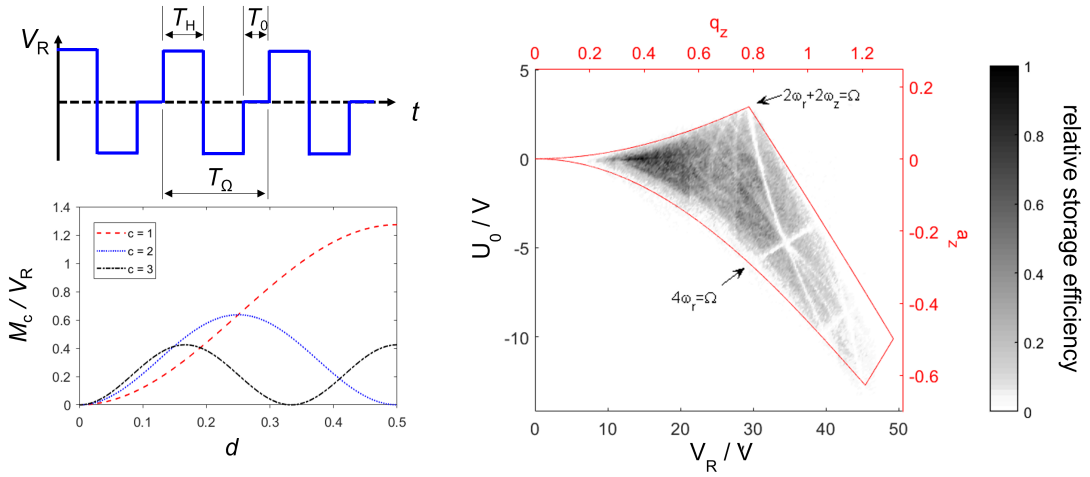

Figure 5.4: Left top: Schematics of 3-state digital guiding-voltages. Left bottom: Magnitudes of Fourier Components M_c of the 3-state digital driving voltages, normalised to V_R. Right: Measured stability diagram of argon ions, confined in a 3-state digital ion trap with $d = 0.4$ and $\Omega = 2\pi \cdot 450\,\mathrm{kHz}$, plotted as a function of guiding field voltages (black axes) and stability parameters (red axes). Red lines represent theoretical borders of stability [76]. Two instability lines are marked. (All subplots adapted from [95]).

While there are different options for the incorporation of the time-interval T_0 [95] into the digital waveform, only the implementation as shown in Fig. 5.4 (top left) is considered here. The definition of the duty cycle $d = T_\mathrm{H}/T_\Omega$ remains unchanged, but is limited to values $0 \leq d \leq 0.5$. An exemplary duty cycle of $d = 0.4$ now signifies that 40 % of the guiding field period T_Ω is occupied by $+V_\mathrm{R}$, followed by an additional 40 % time interval with $-V_\mathrm{R}$. The remaining 20 % of the guiding field period is labeled as T_0 and held at $V_\mathrm{R} = 0\,\mathrm{V}$. Due to the equal duration of the $\pm V_\mathrm{R}$ segments, no additional DC component is generated by use of this 3-state digital signal form. The magnitudes of the AC Fourier components with $c \geq 1$ can be calculated as $M_\mathrm{c} = 4/c\pi \cdot \sin^2(c\pi d) \cdot V_\mathrm{R}$ and are displayed in Fig. 5.4 (bottom left).

Using 3-state digital guiding-voltages with $d = 0.4$, the stability diagram of argon ions has been measured once again (Fig. 5.4, right). Identical structures and instability lines as the ones measured with harmonic or two-state digital guiding voltages are observed. Yet again, these structures occur at different AC voltage amplitudes V_{R} as the magnitude of the first order Fourier component of the guiding signal is enlarged by a factor of 1.15 compared to the harmonic signal. Using this first-order Fourier magnitude, the stability diagram can be mapped into the conventional limits in the $a_{\mathrm{z}} - q_{\mathrm{z}}$ parameter-space (Fig. 5.4, right, red lines) by adjusting the radiofrequency voltage-amplitude in the q_{z} parameter (Eq. 5.8).

5.2 First polyanion production in a radiofrequency ion trap

The modifications to the guiding field voltages have been adapted to a linear radiofrequency ion trap, which has been specifically integrated into the ClusterTrap setup for investigating interactions between electrons and clusters (Fig. 3.1, red-marked components). In a linear radiofrequency ion-trap design ions are confined radially by the AC and DC voltages as describes in Chap. 5, while their axial ion motion is limited by additional DC potentials.

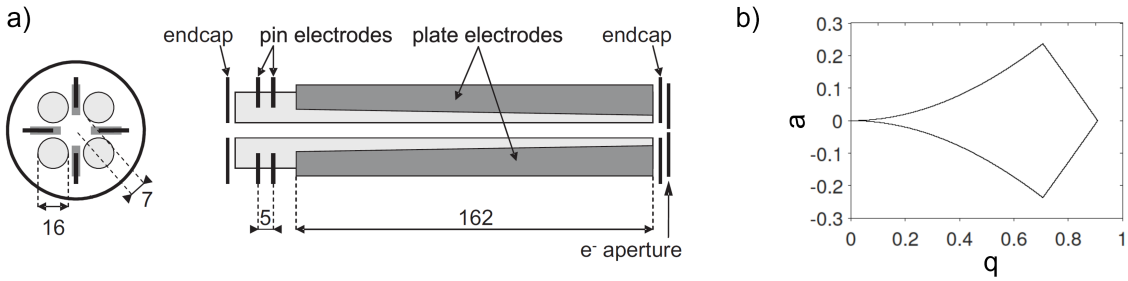

Figure 5.5: a) Schematic views of the linear radiofrequency trap used for polyanion production. Pin (black) and plate electrodes (dark grey) are located between the radiofrequency-rods (light grey). The longitudinal view additionally shows the endcap electrodes and an electron aperture. Dimensions are given in mm. Adapted from [42]. b) Theoretical stability diagram of a linear radiofrequency ion trap [76].

The linear radiofrequency ion trap consists of four rods of 16 mm diameter that are installed parallel to the axial trap axis (Fig. 5.5, a)). The trap size is determined by the minimal distance from this central axis to the rod surfaces ($r_0 = 7\,\mathrm{mm}$). Opposite rods form pairs, driven with identical radiofrequency signals, while neighbouring rods receive signals with a 180° phase shift, creating a quadrupole potential that enables radial ion confinement. Analogous to the trap-design with one ring and two endcap electrodes described before (Chap. 5), the application of a DC voltage difference between the guiding field electrodes (rod pairs) generates an a-parameter, restricting the range of simultaneously storable mass-to-charge ratios. Additionally, for axial confinement, endcap electrodes with DC voltages are utilised, limiting the

simultaneous storage to ions with a specific charge sign. To further manipulate the ion cloud's axial position within the trap, plate and pin electrodes are introduced between the rods. DC voltages at these elements enable to control the axial position of the ion cloud within the trap, e.g. for adjusting the target density prior to interaction studies or as preparational step prior to the ion ejection.

The stability diagram (Fig. 5.5b) characterises the radial storage in the linear radiofrequency ion trap and is symmetric with respect to the q-axis. The storage parameters are given by:

$$a = a_{\mathrm{x,lin}} = -a_{\mathrm{y,lin}} = -\frac{8\,Q\,(U_0 + M_0)}{m r_0^2 \Omega^2} \quad \text{and} \quad q = q_{\mathrm{x,lin}} = -q_{\mathrm{y,lin}} = \frac{4\,Q\,M_1}{m r_0^2 \Omega^2} \quad , \quad (5.9)$$

where M_0 and M_1, as described in Chapter 5.1, correspond to the magnitudes of the zeroth and first-order Fourier components of the two- or three-state digital guiding signal, that is chosen for the radiofrequency ion trap operation.
As pin and plate electrodes are located between the rods, which are used to create the radial storage potential, DC voltages applied to these additional elements are known to alter the storage conditions [96, 97]. Due to the shielding effect of pin and plate electrodes, ions can be stored at AC voltage amplitudes beyond the stability limits (e.g., up to $q \approx 0.95$ instead of $q = 0.908$ for $a = 0$). Therefore, stability parameters are given as a lower estimate of the storage conditions in the following.

For the production of polyanionic clusters in a linear radiofrequency ion trap, electrons are guided through the trap along the central axis, while clusters are stored. This approach allows for the sequential attachment of multiple electrons to a cluster and the accumulation of clusters with higher charge states for subsequent collective ejection from the trap. Since the storage parameters scale linearly with the charge state (Eq. 5.9), the maximum charge state that can be simultaneously stored with its monoanionic precursors after electron attachment, depends on the a and q values of the monoanionic particles. For example, a cluster with charge $z = 1$ stored at $(a; q) = (0; 0.25)$ can be trapped simultaneously with polyanions of charge states $z = 2$ and 3 at $(a; q) = (0; 0.5)$ and $(a; q = 0; 0.75)$, respectively. However, simultaneous confinement with tetraanions ($z = 4$) is not possible, as their storage parameters of $(a; q) = (0; 1)$ are beyond the stability boundary.

As electron emitter, a pin-based halogen lamp with opened glass-cover is used. The resistively heated, coiled tungsten-filament has a length of approximately 5 mm. Its electron energy distribution is determined by the voltage drop between the filament ends, resulting in an energy spread of about 6 eV for typical electron-filament parameters [98]. For reduction of the emission cone of the extended filament, a 1.5 mm aperture has been installed in front of the electron-filament sided endcap-electrode of the linear radiofrequency ion trap (comp. Fig. 5.5a).
To guide the electron beam along the central trap-axis, the vacuum vessel of the linear radiofrequency ion trap has been overlaid with the magnetic field from two coils in a Helmholtz-like arrangement [98]. The connections and mountings of the

vacuum vessel prevent the coils from being aligned in an exact Helmholtz configuration, causing the generated magnetic field to be non-uniform over the entire trap length. Specifically, two magnetic-field maxima are close to the positions of the endcap electrodes, where the electrons enter and leave the trapping volume. In between, the field strength decreases to about 80 % of the maximum [99]. An influence of an magnetic field of up to 25 mT on cluster storage has not been observed.
Tests without application of a radiofrequency guiding field (comparable to the 0 V phase of the 3-state digital voltage signal) show that the electron current transmitted through the trap improves with increasing magnetic field strength, up to and beyond the typically used 20 mT, indicating a high divergence of the incoming electron beam.
Depending on the angle of the electron path with respect to the magnetic field axis, the magnetic field inhomogeneity affects both the axial kinetic energy of the electrons within the ion trap and their gyroradii around the magnetic field lines. Near the endcap electrodes, in regions with magnetic field maxima, the electron beam is compressed for efficient entry and exit. However, the magnetic field gradients can also lead to electron reflection, preventing their passage. In contrast, reduced magnetic field strength between the endcap electrodes enlarges the electron beam radii, increasing the possibility of electron interaction with trap components and potentially causing charging.

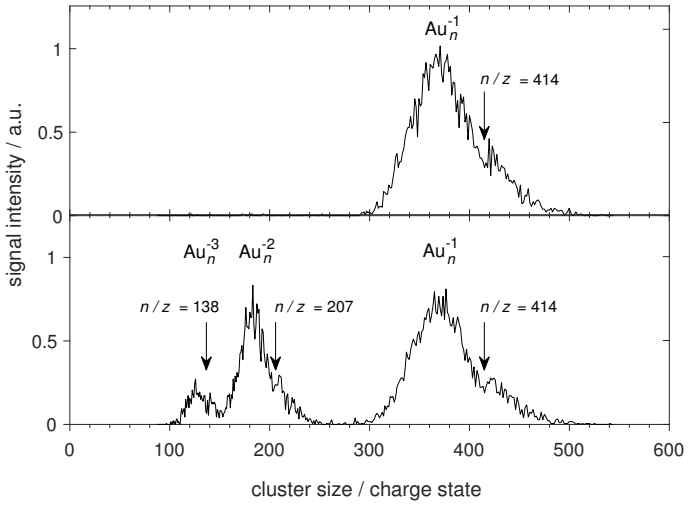

Figure 5.6: Abundance spectra of gold clusters stored in a 2-state digital ion trap with $d = 0.5$, $\Omega = 2\pi \cdot 35\,\mathrm{kHz}$ and $V_\mathrm{R} = 85\,\mathrm{V}$ without (top) and with electron interaction (bottom). Di- and tri-anions are produced after exposing the gold monoanions to an 45 eV electron beam for 200 ms which is guided through the trap by a magnetic field of $\approx 20\,\mathrm{mT}$. An indentation at $n/z \approx 414$, caused by an instability during the accumulation of monoanionic cluster in the first linear radiofrequency ion trap (compare Fig. 3.1), is reproduced for the higher charge states (arrows). Fig. adapted from [100].

Initially, the electron attachment has been tested in a 2-state digital ion trap with a duty cycle of $d = 0.5$. To this end, monoanionic gold clusters of cluster sizes ranging from 300 to 500 and an intensity maximum at $n \sim 370$, have been stored for 270 ms at a driving field frequency of $\Omega = 2\pi \cdot 35\,\mathrm{kHz}$ and a digital voltage amplitude of $V_\mathrm{R} = 85\,\mathrm{V}$ (Fig. 5.6, top). Their storage parameter can be estimated to $(a; q) \approx (0; 0.18 - 0.30)$ (Eq. 5.9). During the storage period, the axial position of the clusters is controlled using the plate-electrodes to accumulate them at the end of the trap facing the electron filament. In a second measurement cycle, electrons with 45 eV are guided into the trap for 200 ms after identical preparational steps, leading to electron attachment to the stored clusters (Fig. 5.6, bottom). Both measurement cycles have been repeated 120 times with an average detection rate of 90 clusters per cycle.
Ion selection has not been employed for this measurement to achieve a maximum target density. Instead, the initial distribution of monoanionic clusters has been marked using an instability (Chap. 5) in the first linear radiofrequency ion trap used for accumulating and bunching of clusters emitted from the source (Chap. 3). The resulting indentation for monoanions at $n/z \approx 414$ also appears in the distributions of di- and trianions at the expected positions of $n/z \approx 207$ and 138, respectively (arrow markers in Fig. 5.6).

In the measurement cycle without electron interaction, only monoanionic clusters are detected. In contrast, in the measurement cycle with electron interaction, just 55 % of the clusters remain singly charged. Dianionic clusters make up 36 % of the detected distribution, trianions constitute 9 %. Although tetra-, penta-, and hexaanions are expected in this size range [37], gold clusters with five or more excess electrons in this size range have charge-to-mass ratios beyond the stability limit ($q > 0.9$, Eq. 5.9). For tetraanions larger than approximately $n \sim 400$, the calculated storage conditions would be suitable, but their absence in the detection could be attributed to insufficient interaction time between the reactants as well as electron energies and trajectories that are not suitable for the attachment process, or a combination of these factors.
With respect to the electron energies, it should be emphasised that although the formation of di- and trianions has been successful, the electron energies of 45 eV were significantly above the required Coulomb barrier heights for generating polyanions of these clusters given by approximately 0.7 eV and 1.6 eV for the production of Au_{370}^{-2} and Au_{370}^{-3}, respectively (compare Chap. 2). In fact, the electron energy was sufficient for the electrons to pass through the endcap electrodes with voltages of $-25\,\mathrm{V}$. Consequently, electrons could enter and exit the trap without adjustments of the endcap voltages. However, even when the endcap-electrode voltages were reduced in each radiofrequency cycle during the time of electron passage, lower electron energies did not result in polyanion production, as the electron energies and trajectories, despite the additional magnetic field, were not suitable for their attachment to the stored clusters.

One possible reason for the necessity of high electron energies could be the geometric overlap between electrons and clusters in the vicinity of the radiofrequency voltages.

As demonstrated by M. Lubs through simulations using sinusoidal trapping voltages, the storage signal, electron energy, and magnetic field influence the depth to which electrons penetrate the trap volume [99]. The influence of the phase of the storage voltages is especially pronounced. Except for brief time intervals around the zero crossings of the radiofrequency voltages, electron penetration into the trap is limited to a few centimeters. These relationships also apply to digital storage signals. It is only through the accumulation of clusters near the electron-filament sided endcap in conjunction with increased electron energy, and thus, penetration depth, that an overlap between the interacting partners becomes possible. Therefore, the actual interaction conditions, including the interaction time, are unknown. This can be circumvented by using the 3-state digital ion trap.

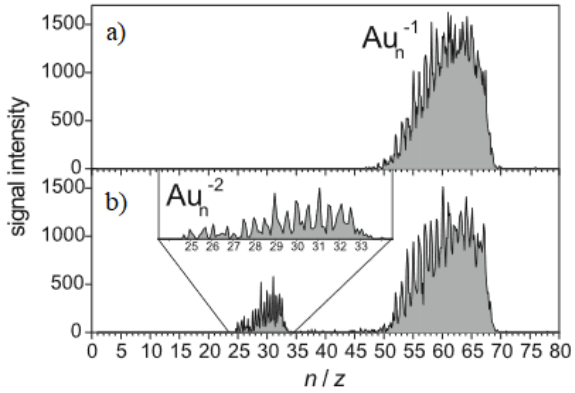

Figure 5.7: Abundance spectra of gold clusters stored for 2.6 s in a 3-state digital ion trap with $d = 0.4$, $\Omega = 2\pi \cdot 65\,\mathrm{kHz}$ and $V_\mathrm{R} = 70\,\mathrm{V}$ without (top) and with electron interaction (bottom). For b), electrons with the energy of 17 eV pass the trap for 2 µs in 20000 consecutive radiofrequency cycles, leading to a total electron-cluster interaction time of 40 ms and the production of dianionic gold clusters. A magnetic field of $\approx 20\,\mathrm{mT}$ is applied to guide the electrons. Figure taken from [98].

Finally, the electron attachment process has been tested in a 3-state digital ion trap with implemented field-free time slots T_0 ($V_\mathrm{R} = 0\,\mathrm{V}$) in which the electrons pass the trap volume. Figure 5.7 (top) displays a distribution of monoanionic gold clusters with sizes ranging from 50 to 70. Clusters are stored in a digital 3-state trap with a duty cycle of $d = 0.4$, a guiding field frequency of $\Omega = 2\pi \cdot 65\,\mathrm{kHz}$, and an amplitude of $V_\mathrm{R} = 70\,\mathrm{V}$ ($(a; q) \approx (0; 0.28 - 0.39)$). With these settings, there exists a time interval of approximately 3 µs within each guiding field period in which the amplitudes of the AC guiding-voltages are zero.

In a second measurement cycle, an electron beam of $\sim 17\,\mathrm{eV}$ has been guided through the trap for 2 µs within these intervals of 20,000 consecutive guiding-field cycles. To allow electrons to pass through the trapping volume, the endcap-electrode voltages were reduced from −25,V to −7,V during the time of electron passage. Within the

cumulative interaction time of 40 ms, gold dianions with a relative abundance of 9 % have been produced (Figure 5.7, bottom).

This measurement confirms the principle of polyanion production in radiofrequency ion traps, where significantly lower electron energies were required for attachment due to the implemented field-free time slots within the guiding field voltage waveforms. However, two issues persist: the energy spread of the filament of multiple electron volts prevents a detailed investigation of attachment conditions and therefore insight into the Coulomb barrier heights of polyanionic clusters, and the strong divergence of the electron beam, leading to charge buildup and signal loss within the 3-state operated digital trap during attachment studies. Both aspects can be improved by replacing the filament with an indirectly heated one, which can exhibit energy spreads well below 1 eV.

To further develop and utilise this technique, it has been successfully transferred to the collaborating research group of Prof. Meiwes-Broer at the University of Rostock. There, after further development steps, silver clusters were charged up to the 7th negative charge state in a linear radiofrequency ion trap which was followed by photoelectron-spectroscopy studies on polyanionic metal clusters [21, 101, 102].

6 Summary and outlook

This thesis presents a comprehensive study on the production of polyanionic clusters within two distinct types of ion storage devices: the Penning and the radiofrequency ion trap.

Through the application of the electron-bath technique in a 12-T Penning trap, the accessible range of polyanionic charge states for aluminium clusters has been expanded up to the 10th charge state. In particular, abundance curves for clusters with 5 to 9 excess electrons have been measured and analysed with respect to their lifetime-dependent appearance sizes. In conjunction with reevaluated charge states ($z = 2$ - 4), these appearance size data reveal a nearly quadratic dependence on the charge state for experimentally accessible lifetimes of approximately 0.1 s to 10 s, enabling predictions of lifetime-dependent appearance sizes for even higher charge states. The exponent of this dependency evolves with varying lifetimes, ranging from $n \sim z^{1.6}$ at the limiting case of $\tau_0 = 0$ s to $n \sim z^3$ for infinite cluster lifetimes when cluster temperature and spillout are not considered.
For clusters with lifetimes of approximately 10 seconds, attachment dynamics have unveiled a sequential attachment behaviour of electrons to already negatively charged clusters. These attachment dynamics exhibit size-dependent characteristics, suggesting that larger clusters can incorporate electrons from the electron bath at an accelerated rate compared to smaller clusters. The question of whether attachment times and sequential behaviour differ for clusters with shorter lifetimes remains open for future research.

With respect to the radiofrequency ion trap, a deeper understanding of digitally operated ion traps has been achieved, which has become a trusted method for an increased range of research fields. Rotational and compressing (or stretching) effects observed in stability diagram measurements within the $U_0 - V_\mathrm{R}$ plane can be attributed to the zeroth and first-order Fourier components of the digital guiding signal. This connection ensures the consistency of the well-established stability diagram within the $a - q$ plane across all considered cases of 2- and 3-state digital guiding signals, thereby enabling statements about storage conditions, motional frequencies, and lines of instabilities.
Finally, the transition from a digital 2-state to a 3-state ion trap has facilitated the controlled production of polyanionic metal clusters within a radiofrequency ion trap. This breakthrough extends the realm of research possibilities for multiply negatively charged gas-phase clusters and is also applicable to polycationic systems as well as other research domains exploring interactions between charged partners with varying mass-to-charge ratios in the gas phase.

7 Bibliography

[1] W. A. de Heer, The physics of simple metal clusters: experimental aspects and simple models, Rev. Mod. Phys. 65 (1993) 611–676. doi:10.1103/RevModPhys.65.611.

[2] H. Haberland, Clusters of Atoms and Molecules: Theory, Experiment, and Clusters of Atoms, no. Bd. 1 in Applications of Mathematics, Springer-Verlag, 1994.

[3] R. L. Johnston, Atomic and Molecular Clusters, 1st Edition, CRC Press, 2002, an optional note. doi:10.1201/9780367805814.

[4] J. Alonso, Structure and Properties of Atomic Nanoclusters, 2nd Edition, EngineeringPro collection, Imperial College Press, 2005.

[5] W. E. Ernst, A. W. Hauser, Metal clusters synthesized in helium droplets: structure and dynamics from experiment and theory, Phys. Chem. Chem. Phys. 23 (2021) 7553–7574. doi:10.1039/D0CP04349D.

[6] C. Rajesh, S. Nigam, C. Majumder, The structural and electronic properties of Au_n clusters on the α-$Al_2O_3(0001)$ surface: a first principles study, Phys. Chem. Chem. Phys. 16 (2014) 26561–26569. doi:10.1039/C4CP02137A.

[7] K. Koyasu, T. Tsukuda, Gas-phase studies of chemically synthesized Au and Ag clusters, The Journal of Chemical Physics 154 (14) (2021) 140901. doi:10.1063/5.0041812.

[8] P. Jena, A. Castleman, Nanoclusters: A Bridge across disciplines, Vol. 1, Elsevier, 2010. doi:10.1016/B978-0-444-53440-8.00001-X.

[9] M. M. Kappes, M. Schär, P. Radi, E. Schumacher, On the manifestation of electronic structure effects in metal clusters, The Journal of Chemical Physics 84 (3) (1986) 1863–1875. doi:10.1063/1.450434.

[10] A. W. Castleman, K. H. Bowen, Clusters: structure, energetics, and dynamics of intermediate states of matter, The Journal of Physical Chemistry 100 (31) (1996) 12911–12944. doi:10.1021/jp961030k.

[11] B. v. Issendorff, O. Cheshnovsky, Metal to insulator transitions in clusters, Annual Review of Physical Chemistry 56 (1) (2005) 549–580. doi:10.1146/annurev.physchem.54.011002.103845.

[12] V. Senz, T. Fischer, P. Oelßner, J. Tiggesbäumker, J. Stanzel, C. Bostedt, H. Thomas, M. Schöffler, L. Foucar, M. Martins, J. Neville, M. Neeb, T. Möller, W. Wurth, E. Rühl, R. Dörner, H. Schmidt-Böcking, W. Eberhardt, G. Ganteför, R. Treusch, P. Radcliffe, K.-H. Meiwes-Broer, Core-hole screening as a probe for a metal-to-nonmetal transition in lead clusters, Phys. Rev. Lett. 102 (2009) 138303. doi:10.1103/PhysRevLett.102.138303.

[13] R. Kelting, A. Baldes, U. Schwarz, T. Rapps, D. Schooss, P. Weis, C. Neiss, F. Weigend, M. M. Kappes, Structures of small bismuth cluster cations, The Journal of Chemical Physics 136 (15) (2012) 154309. doi:10.1063/1.3703014.

[14] T. Rapps, R. Ahlrichs, E. Waldt, M. M. Kappes, D. Schooss, On the structures of 55-atom transition-metal clusters and their relationship to the crystalline bulk, Angewandte Chemie International Edition 52 (23) (2013) 6102–6105. doi:10.1002/anie.201302165.

[15] I. Barke, H. Hartmann, D. Rupp, L. Flückiger, M. Sauppe, M. Adolph, S. Schorb, C. Bostedt, R. Treusch, C. Peltz, S. Bartling, T. Fennel, K.-H. Meiwes-Broer, T. Möller, The 3d-architecture of individual free silver nanoparticles captured by x-ray scattering, Nature Communications 6 (1) (2015) 6187. doi:10.1038/ncomms7187.

[16] S. Becker, G. Dietrich, H.-U. Hasse, N. Klisch, H.-J. Kluge, D. Kreisle, S. Krückeberg, M. Lindinger, K. Lützenkirchen, L. Schweikhard, H. Weidele, J. Ziegler, Collision induced dissociation of stored gold cluster ions, Zeitschrift für Physik D Atoms, Molecules and Clusters 30 (4) (1994) 341–348. doi:10.1007/BF01426399.

[17] M. Vogel, A. Herlert, L. Schweikhard, Photodissociation of small group-11 metal cluster ions: fragmentation pathways and photoabsorption cross sections, J.Am. Soc. Mass Spectrom. 14 (6) (2003) 614–621. doi:10.1016/S1044-0305(03)00203-4.

[18] M. Wolfram, S. König, S. Bandelow, P. Fischer, A. Jankowski, G. Marx, L. Schweikhard, Disentangling the photodissociation pathways of small lead clusters by time-resolved monitoring of their delayed decays: the case of, Journal of Physics B: Atomic, Molecular and Optical Physics 51 (4) (2018) 044005. doi:10.1088/1361-6455/aa9801.

[19] S. König, A. Jankowski, G. Marx, L. Schweikhard, M. Wolfram, Fission of polyanionic metal clusters, Phys. Rev. Lett. 120 (2018) 163001. doi:10.1103/PhysRevLett.120.163001.

[20] C. Harris, A. J. Stace, Coulomb fission in multiply-charged ammonia clusters: Accurate measurements of the rayleigh instability limit from fragmentation patterns, J. Phys. Chem. A 122 (10) (2018) 2634–2644. doi:10.1021/acs.jpca.8b00815.

[21] F. Martinez, N. Iwe, M. Müller, K. Raspe, L. Schweikhard, J. Tiggesbäumker, K.-H. Meiwes-Broer, Cresting the Coulomb barrier of polyanionic metal clusters, Phys. Rev. Lett. 126 (2021) 133001. doi:10.1103/PhysRevLett.126.133001.

[22] O. Echt, P. Scheier, T. D. Märk, Multiply charged clusters, Comptes Rendus Physique 3 (3) (2002) 353–364. doi:10.1016/S1631-0705(02)01325-7.

[23] O. Schapiro, P. J. Kuntz, K. Möhring, P. A. Hervieux, D. H. E. Gross, M. E. Madjet, Fragmentation phase transitions in atomic clusters iii, Zeitschrift für Physik D Atoms, Molecules and Clusters 41 (3) (1997) 219–227. doi:10.1007/s004600050314.

[24] U. Näher, S. Bjørnholm, S. Frauendorf, F. Garcias, C. Guet, Fission of metal clusters, Phys. Rep. 285 (6) (1997) 245–320. doi:10.1016/s0370-1573(96)00040-3.

[25] F. Chandezon, T. Bergen, A. Brenac, C. Guet, B. A. Huber, H. Lebius, A. Pesnelle, Fission channels of multiply charged sodium clusters near the rayleigh limit, Phys. Rev. A 63 (2001) 051201. doi:10.1103/PhysRevA.63.051201.

[26] I. Last, Y. Levy, J. Jortner, Beyond the Rayleigh instability limit for multicharged finite systems: From fission to Coulomb explosion, Proc. Natl. Acad. Sci. USA 99 (14) (2002) 9107–9112. doi:10.1073/pnas.142253999.

[27] A. Dreuw, L. S. Cederbaum, Nature of the repulsive coulomb barrier in multiply charged negative ions, Phys. Rev. A 63 (2000) 012501. doi:10.1103/PhysRevA.63.012501.

[28] C. Yannouleas, U. Landman, A. Herlert, L. Schweikhard, Multiply charged metal cluster anions, Phys. Rev. Lett. 86 (2001) 2996–2999. doi:10.1103/PhysRevLett.86.2996.

[29] L. R. F.R.S., Xx. on the equilibrium of liquid conducting masses charged with electricity, The London, Edinburgh, and Dublin Philosophical Magazine and Journal of Science 14 (87) (1882) 184–186. doi:10.1080/14786448208628425.

[30] L. v. Szentpály, Universal method to calculate the stability, electronegativity, and hardness of dianions, The Journal of Physical Chemistry A 114 (40) (2010) 10891–10896. doi:10.1021/jp107177d.

[31] M. Scheller, L. Cederbaum, A construction principle for stable multiply charged molecular anions in the gas phase, Chemical Physics Letters 216 (1) (1993) 141–146. doi:10.1016/0009-2614(93)E1259-J.

[32] A. J. Cohen, P. Mori-Sánchez, W. Yang, Insights into current limitations of density functional theory, Science 321 (5890) (2008) 792–794. doi:10.1126/science.1158722.

[33] S. König, Lead-cluster investigations, Ph.D. thesis, University of Greifswald (2017).

[34] A. Herlert, R. Jertz, J. Alonso Otamendi, A. González Martínez, L. Schweikhard, The influence of the trapping potential on the attachment of a second electron to stored metal cluster and fullerene anions, International Journal of Mass Spectrometry 218 (3) (2002) 217–225. doi:10.1016/S1387-3806(02)00723-6.

[35] N. Walsh, F. Martinez, G. Marx, L. Schweikhard, F. Ziegler, Multiply negatively charged aluminium clusters II. - production of Al_n^{3-}, Eur. Phys. J. D 52 (1-3) (2009) 27–30. doi:10.1140/epjd/e2008-00255-3.

[36] N. Walsh, F. Martinez, G. Marx, L. Schweikhard, F. Ziegler, First observation of a tetra-anionic metal cluster, Al_n^{4-}, J. Chem. Phys. 132 (1) (2010) 014308. doi:10.1063/1.3270153.

[37] F. Martinez, S. Bandelow, G. Marx, L. Schweikhard, A. Vass, Abundances of tetra-, penta-, and hexa-anionic gold clusters, J. Phys. Chem. C 119 (20) (2015) 10949–10957. doi:10.1021/jp510947p.

[38] S. Bandelow, F. Martinez, S. König, L. Schweikhard, Production of polyanionic aluminium clusters with up to 10 excess electrons, Int. J. Mass Spectrom. 473 (2022) 116780. doi:10.1016/j.ijms.2021.116780.

[39] L. S. Brown, G. Gabrielse, Geonium theory: Physics of a single electron or ion in a penning trap, Rev. Mod. Phys. 58 (1986) 233–311. doi:10.1103/RevModPhys.58.233.

[40] P. K. Ghosh, Ion Traps, 1st Edition, Clarendon Press, Oxford University Press, 1995.

[41] F. Major, G. Viorica, G. Werth, Charged Particle Traps, Springer Berlin Heidelberg New York, 2005. doi:10.1007/b137836.

[42] F. Martinez, S. Bandelow, C. Breitenfeldt, G. Marx, L. Schweikhard, A. Vass, F. Wienholtz, Upgrades at ClusterTrap and latest results, Int. J. Mass Spectrom. 365-366 (2014) 266–274. doi:10.1016/j.ijms.2013.12.018.

[43] A. Herlert, L. Schweikhard, Production of dianionic and trianionic noble metal clusters in a Penning trap, Int. J. Mass Spectrom. 229 (1) (2003) 19–25. doi:10.1016/S1387-3806(03)00251-3.

[44] F. Martinez, S. Bandelow, C. Breitenfeldt, G. Marx, L. Schweikhard, F. Wienholtz, F. Ziegler, Appearance size of poly-anionic aluminum clusters, Al_n^{z-}, z=2-5, Eur. Phys. J. D 67 (2) (feb 2013). doi:10.1140/epjd/e2012-30265-3.

[45] W. Paul, H. Steinwedel, Notizen: Ein neues massenspektrometer ohne magnetfeld, Zeitschrift für Naturforschung A 8 (7) (1953) 448–450. doi:10.1515/zna-1953-0710.

[46] H. S. Margolis, Frequency metrology and clocks, JOURNAL OF PHYSICS B-ATOMIC MOLECULAR AND OPTICAL PHYSICS 42 (15) (AUG 14 2009). doi:10.1088/0953-4075/42/15/154017.

[47] M. Kumph, M. Brownnutt, R. Blatt, Two-dimensional arrays of radio-frequency ion traps with addressable interactions, New Journal of Physics 13 (7) (2011) 073043. doi:10.1088/1367-2630/13/7/073043.

[48] S. Willitsch, Coulomb-crystallised molecular ions in traps: methods, applications, prospects, International Reviews in Physical Chemistry 31 (2) (2012) 175–199. doi:10.1080/0144235X.2012.667221.

[49] D. Nolting, R. Malek, A. Makarov, Ion traps in modern mass spectrometry, Mass Spectrometry Reviews 38 (2) (2019) 150–168. doi:10.1002/mas.21549.

[50] G. C. Roesch, E. Garand, Tandem mass-selective cryogenic digital ion traps for enhanced cluster formation, The Journal of Physical Chemistry A 127 (36) (2023) 7665–7672. doi:10.1021/acs.jpca.3c04706.

[51] C. Kittel, Einführung in die Festkörperphysik, 14th Edition, Oldenbourg Wissenschaftsverlag: London, U.K., 1994.

[52] D. R. Snider, R. S. Sorbello, Density-functional calculation of the static electronic polarizability of a small metal sphere, Phys. Rev. B 28 (1983) 5702–5710. doi:10.1103/PhysRevB.28.5702.

[53] J. P. Perdew, Energetics of charged metallic particles: From atom to bulk solid, Phys. Rev. B 37 (11) (1988) 6175–6180. doi:10.1103/physrevb.37.6175.

[54] M. A. Hoffmann, G. Wrigge, B. v. Issendorff, Photoelectron spectroscopy of Al^-_{32000} : Observation of a "Coulomb staircase" in a free cluster, Phys. Rev. B 66 (2002) 041404. doi:10.1103/PhysRevB.66.041404.

[55] X.-B. Wang, L.-S. Wang, Experimental search for the smallest stable multiply charged anions in the gas phase, Phys. Rev. Lett. 83 (17) (1999) 3402–3405. doi:10.1103/physrevlett.83.3402.

[56] G. Gamow, Zur Quantentheorie des Atomkernes, Z. Phys. 51 (3) (1928) 204–212. doi:10.1007/BF01343196.

[57] R. W. Gurney, E. U. Condon, Quantum mechanics and radioactive disintegration, Phys. Rev. 33 (1929) 127–140. doi:10.1103/PhysRev.33.127.

[58] M. S. Sodha, P. K. Kaw, Field emission from negatively charged solid particles, J. Phys. D 1 (10) (1968) 1303–1307. doi:10.1088/0022-3727/1/10/310.

[59] E. L. Murphy, R. H. Good, Thermionic emission, field emission, and the transition region, Phys. Rev. 102 (1956) 1464–1473. doi:10.1103/PhysRev.102.1464.

[60] S. Becker, K. Dasgupta, G. Dietrich, H. Kluge, S. Kuznetsov, M. Lindinger, K. Lützenkirchen, L. Schweikhard, J. Ziegler, A Penning trap mass spectrometer for the study of cluster ions, Review of Scientific Instruments 66 (10) (1995) 4902–4910. doi:10.1063/1.1146172.

[61] L. Schweikhard, S. Becker, K. Dasgupta, G. Dietrich, H.-J. Kluge, D. Kreisle, S. Krückeberg, S. Kuznetsov, M. Lindinger, K. Lützenkirchen, B. Obst, C. Walther, H. Weidele, J. Ziegler, Trapped metal cluster ions, Physica Scripta 1995 (T59) (1995) 236. doi:10.1088/0031-8949/1995/T59/032.

[62] L. Schweikhard, S. Krückeberg, K. Lützenkirchen, C. Walther, The Mainz cluster trap, Eur. Phys. J. D 9 (1) (1999) 15–20. doi:10.1007/s100530050391.

[63] L. Schweikhard, K. Hansen, A. Herlert, G. Marx, M. Vogel, New approaches to stored clusterions, The European Physical Journal D - Atomic, Molecular, Optical and Plasma Physics 24 (1) (2003) 137–143. doi:10.1140/epjd/e2003-00181-x.

[64] H. Weidele, U. Frenzel, T. Leisner, D. Kreisle, Production of "cold/hot" metal cluster ions: a modified laser vaporization source, Z Phys D Atom Mol Cl 20 (1991) 411–412. doi:10.1007/BF01544024.

[65] G. Bollen, R. B. Moore, G. Savard, H. Stolzenberg, The accuracy of heavy-ion mass measurements using time of flight-ion cyclotron resonance in a Penning trap, Journal of Applied Physics 68 (9) (1990) 4355–4374. doi:10.1063/1.346185.

[66] G. Savard, S. Becker, G. Bollen, H.-J. Kluge, R. Moore, T. Otto, L. Schweikhard, H. Stolzenberg, U. Wiess, A new cooling technique for heavy ions in a penning trap, Phys. Lett. A 158 (5) (1991) 247–252. doi:10.1016/0375-9601(91)91008-2.

[67] N. Walsh, F. Martinez, G. Marx, L. Schweikhard, Multiply negatively charged aluminium clusters, The European Physical Journal D 43 (1) (2007) 241–245. doi:10.1140/epjd/e2007-00114-9.

[68] L. Schweikhard, A. Herlert, G. Marx, Simultaneous Trapping of Electrons and Anionic Clusters in a Penning Trap, AIP Conference Proceedings 692 (1) (2003) 203–210. doi:10.1063/1.1635176.

[69] T. M. O'Neil, Cooling of a pure electron plasma by cyclotron radiation, The Physics of Fluids 23 (4) (1980) 725–731. doi:10.1063/1.863044.

[70] A. Herlert, S. Krückeberg, L. Schweikhard, M. Vogel, C. Walther, First observation of doubly charged negative gold cluster ions, Phys. Scr. T80 (B) (1999) 200. doi:10.1238/physica.topical.080a00200.

[71] A. Herlert, K. Hansen, L. Schweikhard, M. Vogel, Multiply charged titanium cluster anions: production and photodetachment, Hyperfine Interactions 127 (1) (2000) 529–532. doi:10.1023/A:1012654825860.

[72] S. König, M. Wolfram, S. Bandelow, G. Marx, L. Schweikhard, Interaction of anionic tin clusters Sn_n^-, $n = 7 - 75$ with electrons - polyanion production and cluster decay, The European Physical Journal D 72 (9) (2018) 153. doi:10.1140/epjd/e2018-90158-y.

[73] D. R. Lide, CRC handbook of chemistry and physics, Vol. 71, CRC press: Boca Raton, Ann Arbor, Boston, 1990.

[74] R. E. March, An introduction to quadrupole ion trap mass spectrometry, Journal of Mass Spectrometry 32 (4) (1997) 351–369. doi:10.1002/(SICI)1096-9888(199704)32:4<351::AID-JMS512>3.0.CO;2-Y.

[75] D. Gerlich, Inhomogeneous RF Fields: A Versatile Tool for the Study of Processes with Slow Ions, John Wiley & Sons, Ltd, 1992, Ch. II & III, pp. 1–98. doi:10.1002/9780470141397.ch1.

[76] N. W. McLachlan, Theory and application of Mathieu functions, 1st Edition, Oxford University Press, Oxford, 1951.

[77] S. Bandelow, G. Marx, L. Schweikhard, The stability diagram of the digital ion trap, Int. J. Mass Spectrom. 336 (2013) 47–52. doi:10.1016/j.ijms.2012.12.013.

[78] X. Chu, M. Holzki, R. Alheit, G. Weitha, Observation of high-order motional resonances of an ion cloud in a paul trap, Int. J. Mass Spectrom. Ion Process 173 (1) (1998) 107–112. doi:10.1016/S0168-1176(97)00262-0.

[79] R. E. March, J. F. J. Todd, Practical Aspects of Ion Trap Mass Spectrometry, CRC Press, 1995.

[80] F. Roßbach, Nichtlineare Dynamik in der Paulschen Ionenfalle, Vol. 5501 of Wissenschaftliche Berichte. FZKA, Universität Karlsruhe (TH), 1995. doi:10.5445/IR/270037283.

[81] S. Bandelow, G. Marx, L. Schweikhard, A split-ring paul trap for dipolar excitation of the radial ion motion and ellipticity studies, The European Physical Journal D 61 (2) (2011) 315–320. doi:10.1140/epjd/e2010-10467-5.

[82] R. Alheit, S. Kleineidam, F. Vedel, M. Vedel, G. Werth, Higher order nonlinear resonances in a paul trap, Int. J. Mass Spectrom. Ion Process 154 (3) (1996) 155–169. doi:10.1016/0168-1176(96)04380-7.

[83] Y. Wang, J. Franzen, K. Wanczek, The non-linear resonance ion trap. part 2. a general theoretical analysis, Int. J. Mass Spectrom. Ion Process 124 (2) (1993) 125–144. doi:10.1016/0168-1176(93)80004-X.

[84] C. Matthiesen, Q. Yu, J. Guo, A. M. Alonso, H. Häffner, Trapping electrons in a room-temperature microwave paul trap, Phys. Rev. X 11 (2021) 011019. doi:10.1103/PhysRevX.11.011019.

[85] S. Sadat Kiai, J. Andre, Y. Zerega, G. Brincourt, R. Catella, Study of a quadrupole ion trap supplied with a periodic impulsional potential, Int. J. Mass Spectrom. Ion Process 107 (2) (1991) 191–203. doi:10.1016/0168-1176(91)80058-U.

[86] S. Sadat Kiai, Y. Zerega, G. Brincourt, R. Catella, J. Andre, Experimental study of a r.f. quadrupole ion trap supplied with a periodic impulsional potential, Int. J. Mass Spectrom. Ion Process 108 (1) (1991) 65–73. doi:10.1016/0168-1176(91)87007-N.

[87] J. Richards, R. Huey, J. Hiller, A new operating mode for the quadrupole mass filter, Int. J. Mass Spectrom. Ion Phys. 12 (4) (1973) 317–339. doi:10.1016/0020-7381(73)80102-0.

[88] F. L. Brancia, B. McCullough, A. Entwistle, J. G. Grossmann, L. Ding, Digital asymmetric waveform isolation (dawi) in a digital linear ion trap, Journal of the American Society for Mass Spectrometry 21 (9) (2010) 1530–1533. doi:10.1016/j.jasms.2010.05.003.

[89] K. W. Lee, C. P. Harrilal, L. Fu, G. S. Eakins, S. A. McLuckey, Digital ion trap mass analysis of high mass protein complexes using ir activation coupled with ion/ion reactions, International Journal of Mass Spectrometry 458 (2020) 116437. doi:10.1016/j.ijms.2020.116437.

[90] F. Simke, P. Fischer, G. Marx, L. Schweikhard, Simulations of a digital ion filter and a digital ion trap for heavy biomolecules, International Journal of Mass Spectrometry 473 (2022) 116779. doi:10.1016/j.ijms.2021.116779.

[91] I. N. Bronstein, K. A. Semendjajew, G. Musiol, H. Mühlig, Taschenbuch der Mathematik, 5th ed., Verlag Harri Deutsch, Frankfurt am Main (2001) 436.

[92] S. A. McLuckey, D. E. Goeringer, G. L. Glish, Selective ion isolation/rejection over a broad mass range in the quadrupole ion trap, Journal of the American Society for Mass Spectrometry 2 (1) (1991) 11–21. doi:10.1016/1044-0305(91)80056-D.

[93] A. Drakoudis, M. Söllner, G. Werth, Instabilities of ion motion in a linear paul trap, International Journal of Mass Spectrometry 252 (1) (2006) 61–68. doi:10.1016/j.ijms.2006.02.006.

[94] M. Anrdt, An ion-trap setup for interaction studies of clusters with intense laser light, Ph.D. thesis, University of Greifswald (2011).

[95] S. Bandelow, G. Marx, L. Schweikhard, The 3-state digital ion trap, International Journal of Mass Spectrometry 353 (2013) 49–53. doi:10.1016/j.ijms.2013.06.003.

[96] A. Vass, Wiederaufbau der ClusterTrap-Apparatur, Diploma thesis (Feb 2009).

[97] S. Menk, P. Bertier, Y. Enomoto, T. Masunaga, T. Majima, Y. Nakano, T. Azuma, A cryogenic linear ion trap beamline for providing keV ion bunches, Review of Scientific Instruments 89 (11) (2018) 113110. doi:10.1063/1.5051044.

[98] F. Martinez, S. Bandelow, G. Marx, L. Schweikhard, A. Vass, Electron attachment to anionic clusters in ion traps, in: M. Wada, P. Schury, Y. Ichikawa (Eds.), TCP 2014, Springer International Publishing, Cham, 2017, pp. 19–27.

[99] M. Lubs, Anlagerung von Elektronen an in einer Hochfrequenzfalle gespeicherten Clustern, Bachelor's thesis (Feb 2012).

[100] F. Martinez, S. Bandelow, G. Marx, L. Schweikhard, Production of multiply-charged metal-cluster anions in Penning and radio-frequency traps, AIP Conference Proceedings 1521 (1) (2013) 230–239. doi:10.1063/1.4796079.

[101] K. Raspe, M. Müller, N. Iwe, R. N. Wolf, P. Oelßner, F. Martinez, L. Schweikhard, K.-H. Meiwes-Broer, J. Tiggesbäumker, A versatile setup for studying size and charge-state selected polyanionic nanoparticles, Review of Scientific Instruments 93 (4) (2022) 043301. doi:10.1063/5.0085187.

[102] N. Iwe, K. Raspe, M. Müller, F. Martinez, L. Schweikhard, K.-H. Meiwes-Broer, J. Tiggesbäumker, Size and charge-state dependence of detachment energies of polyanionic silver clusters, The Journal of Chemical Physics 155 (16) (2021) 164303. doi:10.1063/5.0068278.

8 Thesis articles

Author contribution

Article I: Production of polyanionic aluminium clusters with up to 10 excess electrons
S. Bandelow, F. Martinez, S. König, L. Schweikhard, *Int. J. Mass Spectrom.*, **473** (2022)
S.B. performed the measurements and data evaluation. S.B. and F.M. discussed the physical background, developed the mathematical description and wrote the manuscript, which was edited by all co-authors.

Article II: The stability diagram of the digital ion trap
S. Bandelow, G. Marx, L. Schweikhard, *Int. J. Mass Spectrom.*, **336**, 47-52 (2013)
G.M. conceived the idea. S.B. performed the measurements, data-analysis, and developed the mathematical description. The manuscript was written by S.B. and edited by all co-authors.

Article III: The 3-state digital ion trap
S. Bandelow, G. Marx, L. Schweikhard, *Int. J. Mass Spectrom.*, **353**, 49-53 (2013)
L.S. developed the idea. S.B. performed the measurements, data-analysis, and developed the mathematical description. The manuscript was written by S.B. and edited by all co-authors.

Article IV: Electron attachment to anionic clusters in ion traps
F. Martinez, S. Bandelow, G. Marx, Lutz Schweikhard, A. Vass *Hyperfine Interact.*, **236**, 19-27 (2015)
F.M. and S.B. performed equal parts of the measurements. In particular, S.B. executed the poly-anion production measurements in the 3-state digital ion trap. The manuscript was written by F.M. and edited by all co-authors.

Confirmed:

Greifswald, den Steffi Bandelow Lutz Schweikhard

Article I

International Journal of Mass Spectrometry 473 (2022) 116780

Contents lists available at ScienceDirect

International Journal of Mass Spectrometry

journal homepage: www.elsevier.com/locate/ijms

Production of polyanionic aluminium clusters with up to 10 excess electrons

Steffi Bandelow [a,*], Franklin Martinez [b], Stephan König [a], Lutz Schweikhard [a]

[a] Institute of Physics, University of Greifswald, 17489, Greifswald, Germany
[b] Institute of Physics, University of Rostock, 18051, Rostock, Germany

ARTICLE INFO

Article history:
Received 24 August 2021
Received in revised form
14 December 2021
Accepted 18 December 2021
Available online 27 December 2021

Keywords:
Metal clusters
Aluminium
Polyanions
Field emission
Appearance sizes
Meta-stability

ABSTRACT

The appearance sizes of polyanionic metal clusters are investigated with respect to their charge states. To this end, free gas-phase aluminium clusters with up to 10 excess electrons have been produced by use of the Penning-trap based electron-bath method. Cluster sizes, forming a meta-stable polyanionic cluster with lifetimes of 0.1 s, 1 s or 10 s, show a systematic dependence on the charge state, which is described by a model for electron-emission. The origin of the observed dependence is discussed.

1. Introduction

The field of cluster physics provides a link between the characteristics of atoms and molecules on the one hand side and of bulk material on the other. Increasing the number of atoms n in a cluster changes its structure and electronic configuration [1–3]. Properties, as for example fragmentation patterns may change with only one atom added to the cluster [4–7] constituting well-defined cluster-size thresholds. However, considering the appearance of free polyanionic clusters, the definition of a size-limit is ambiguous, as the stability of the polyanions with respect to electron emission has to be considered.

In general, an electron is bound to a cluster if its binding energy is below the vacuum level, which is here considered as a positive value of the electron affinity EA [8,9]. This condition defines an obvious minimum cluster-size limit for electron attachment. However, it overestimates experimentally observed appearance sizes [10,11] because it neglects the Coulomb barrier. This barrier stabilises polyanionic systems with electron binding energies above the vacuum level [12–14]. Following classical physics, the Coulomb barrier stabilises an electron with binding levels up to its potential maximum. However, this picture underestimates experimental appearance sizes. A proper description is obtained by quantum mechanics, i.e. when taking electron tunneling through the finite-size barrier into account [15].

With respect to measurements, it is tempting to take the smallest detectable polyanionic cluster as a size limit [12,16–18]. However, it is not always convenient as such a “minimum cluster size” n_{min} depends strongly on experimental constraints and prevents a proper comparison between different experimental studies. Therefore, it is more appropriate to take into account the electron tunneling, i.e. to describe the appearance of polyanionic clusters with respect to their lifetime τ. Such an approach leads to a corresponding “appearance size” $n_{\mathrm{app},\tau}$, whose determination - however - depends on theoretical input. Yet, $n_{\mathrm{app},\tau}$ is expected to be less sensitive to experimental conditions than the minimum cluster size, n_{min}.

In the present work, the appearance sizes $n_{\mathrm{app},\tau}$ for anionic charge states up to $z = 9$ of aluminium clusters are determined, taking into account the electron tunneling through the Coulomb barrier. We briefly introduce the experimental setup, outline the model for polyanion stability, and analyse the derived appearance sizes with respect to meta-stability. Finally, the relation between appearance size and charge state is discussed.

* Corresponding author.
E-mail address: bandelows@uni-greifswald.de (S. Bandelow).

https://doi.org/10.1016/j.ijms.2021.116780
1387-3806/

2. Experimental setup and procedure

The experiments were performed using the electron-bath technique at the ClusterTrap setup [18–22]. The procedures have been reported in detail, before [22].

In short: Monoanionic aluminium clusters are produced in a laser-vaporisation source [23] and accumulated in a digitally operated linear radio-frequency trap [24–26]. The clusters are then transferred into a Penning trap with a cylindrical electrode design and a magnetic field of 12 T. The source produces clusters of a broad range of sizes. Their capture is partially selective due to their different flight times from the radio-frequency trap to the Penning trap. For further selection of the size of interest as well as for centering them in the Penning trap, monoanionic clusters are subjected to quadrupole-excitation assisted buffer-gas cooling [27].

For the conversion into polyanionic clusters, the electron-bath is used [18,28], in which the clusters are stored simultaneously with electrons in a trapping potential of 23 eV. To produce the "electron-bath", a 60-eV electron beam is guided through the trap for 20 ms along the magnetic-field axis, ionising argon buffer-gas atoms along its path. While the positively charged argon ions leave the trap immediately, secondary electrons of sufficiently low energy remain stored. In the following interaction time of typically 1 s, polyanions are formed by sequential electron attachment to the monoanionic precursors (Appendix A). After the electron-bath, all clusters are ejected axially from the trap towards a micro-channel plate detector with conversion dynode for time-of-flight analysis. Finally, the abundances of all detected ion species are determined from the time-of-flight spectra. Typically, this experimental cycle is repeated 25 times, to improve ion-count statistics. To compensate for fluctuations in the monoanion signal during the measurements, between each repetition of the experimental cycle, an identical cycle but without application of the electron-beam pulse is implemented.

Fig. 1a shows such a reference abundance spectrum of size-selected $Al^{-1}_{1250\pm8}$ clusters. Due to the resolving power of the time-of-flight detection (R_{ToF} ~ 100), the ion signal covers a range of cluster sizes with a FWHM of $w_n = 16$. As no cluster-electron interaction takes place, higher charge states are not detected. In each subplot, the spectrum is normalised to the height of its most-abundant peak.

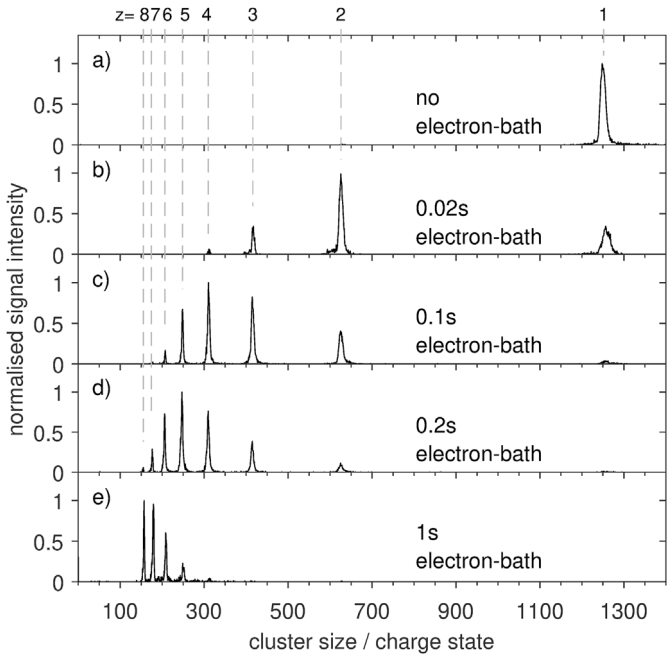

Fig. 1. Abundance spectra of negatively-charged aluminium clusters $Al^{-z}_{1250\pm8}$ without (a) and after an electron-bath of 0.02 s (b), 0.1 s (c), 0.2 s (d) and 1 s (e).

In Fig. 1b, the monoanionic clusters are exposed to an electron-bath for 20 ms (i.e. the same duration as the electron-beam pulse). In comparison to Fig. 1a, the relative share of the monoanion signal is reduced to 27 % as the clusters are converted to di- (55 %), tri- (16 %) and tetraanions (2 %).

For 100 ms electron-cluster interaction (Fig. 1c), the distribution shifts to charge states up to $z = 6$ (4 %), while hardly any mono-anions remain (~ 2 %). The highest abundance with respect to the sum of all detected ions is observed for $z = 4$ with 31 %. A comparable proportion of 32 % for the next higher charge state $z = 5$ is reached for 200 ms (Fig. 1d), while charge states up to $z = 8$ are now observed (< 1 %). At last, Fig. 1e shows a spectrum after an electron-bath with a duration of 1 s. Here, mono-, di- and trianions are not detected anymore, while the charge states $z = 7$ and 8 dominate the spectrum with relative abundances of 33 % and 29 %, respectively. Applying even longer interaction times increases the relative abundance of $z = 8$, but does not result in the production of higher charge states (Appendix A). All measurements presented in the following were taken at an electron-bath duration of 1 s.

3. Experimental results

Fig. 2 summarises the results of the present measurements. For each of the 116 cluster sizes investigated within the range of $325 \leq n \leq 1950$, polyanions are produced as described in Section 2. The polyanion abundances are normalised to the sum of all detected ions and displayed as a function of the cluster size. Note, that data points with zero-abundance are omitted from the plot. In the exemplary case of the smallest investigated cluster size $n = 325 \pm 4$, only di-, tri-, and tetraanions were detected, with relative abundances of 9 %, 34 % and 56 %, respectively. Clusters with $z \geq 5$ are not observed. Fig. 2 shows the changes of the charge-state distribution as a function of cluster size. To map these changes in detail, the increment of the cluster size, for which the polyanion abundances are measured, is adapted. For example, for $n < 600$ steps of $\Delta n = 3$ were chosen because of the steep abundance rise of the penta- and hexaanions. For $n > 1650$ steps of $\Delta n = 25$ were sufficient to monitor the abundance behaviour.

With increasing cluster size, higher and higher charge states are observed (Fig. 2, coloured data points). The evolution of each charge state is visualised by moving averages over 5 data points (solid lines). The smallest cluster size, for which a charge state is experimentally detected, is identified as the minimum cluster size, n_{min} (Table 1, Fig. 2). For larger clusters, the relative ion abundance of the polyanionic charge state increases until conversion into the next higher charge state sets in. The cluster size with the maximum abundance of the moving averages n_{max} (Table 1) marks the transition from an increasing abundance to a slowly decreasing one, as the next higher charge state is produced by further electron attachment. The uncertainties of n_{min} and n_{max} are discussed in Appendix B. For the highest cluster size studied, $n = 1950 \pm 16$, only the charge states $z = 5$ to 10 were detected, with the relative abundances of 2 %, 7 %, 18 %, 29 %, 27 % and 13 %, respectively.

In Fig. 3 the threshold values n_{min} (blue symbols), and also n_{max} (black symbols) from Table 1 are plotted over the charge state z. As noted above, the threshold size increases with z. But it becomes obvious that this behaviour is not simply linear, but of some higher order. Indeed, for highly positively charged clusters, stability is limited by fission processes which show a quadratic relationship between critical particle size and charge [29,30]. The Coulomb energy of the repelling charges destabilises a cluster, while the

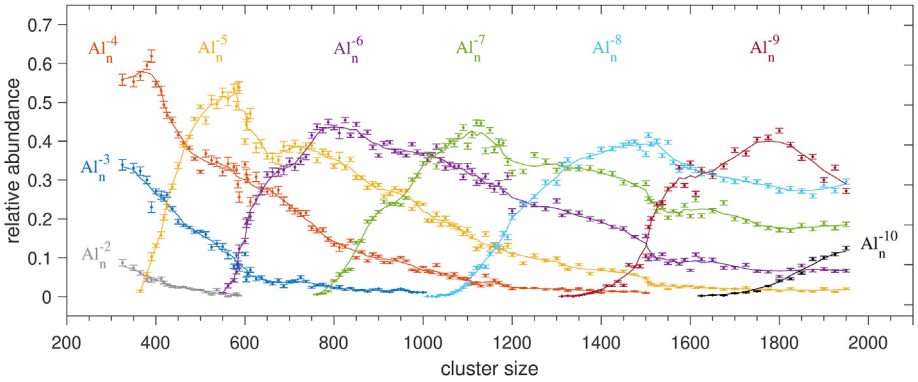

Fig. 2. Relative abundances of polyanions of different charge states as a function of cluster size. Solid lines to guide the eye are moving averages over 5 data points. In the decreasing part of the curves data are shown only for relative abundances above 1 %.

Table 1
Minimum cluster size n_{min} and cluster size n_{max}, marking the maximum abundance of the moving average for aluminium clusters of negative charge states $z = 5$ to 10. For $z = 10$, a value for n_{max} could not be assigned in the size range under investigation. Critical sizes with respect to cluster fission, n_{crit}, have been estimated for comparison.

z	5	6	7	8	9	10
n_{min}	365(4)	550(4)	762(5)	1010(6)	1312(9)	1625(11)
n_{max}	581(12)	800(25)	1110(20)	1506(25)	1775(50)	–
n_{crit}	50	72	98	128	162	200

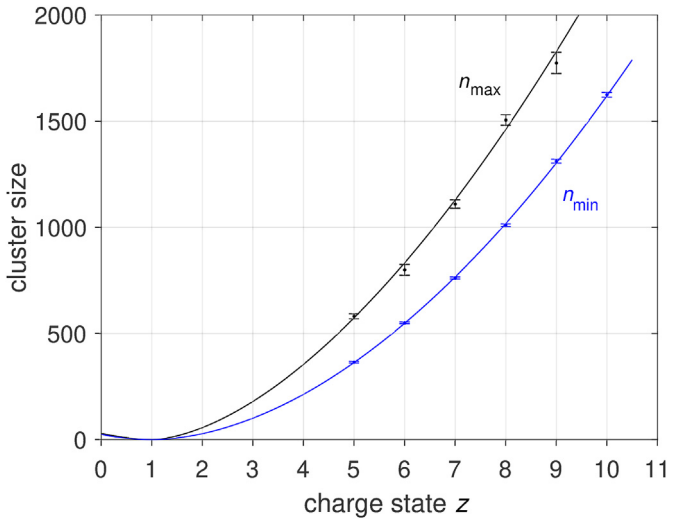

Fig. 3. Minimum cluster size n_{min} (blue) and cluster size of maximum moving-average abundance n_{max} (black) as a function of the charge state. Solid lines are fits to the data. See text for details.

surface energy has a stabilising effect [31,32]. Fission occurs, if a limit of charges per cluster size is exceeded and the system disintegrates into two, lower charged fragments. In literature, a rough approximation states for the critical size of metal clusters a relation $n_{crit} \approx 2 \cdot z^2$ [4].

Negatively charged clusters, as observed in Fig. 2, however, appear only far above this fission limit (Table 1). The difference is caused by the competing decay channel of electron emission, which does not exist for positively charged species. It destabilises polyanions already at cluster sizes far above the fission limit. Regarding this electron emission, we have previously shown that the increasing part of an abundance curve - as shown in Fig. 2 - is basically determined by two aspects, being electron tunneling and cluster temperature [33]. Hence, such a complex interplay should also be reflected in the positions of n_{min} and n_{max} in Fig. 3. We will get back to this presumption for the discussion in Section 5.2.

As for the moment, we take a basic assumption and apply a fit equation of the form $n(z) = a \cdot (z-1)^b$ to the data in Fig. 3 (solid lines). This fit ansatz follows a power function, as a more generalised approach with regard to the most common z-dependency, the Coulomb's law. The shift term takes into account, that the stability of a z-charged anionic cluster is considered as emission of an electron from the potential of a $(z-1)$-charged anion. The fitting yields the equations $n_{min} = 28.10 \cdot (z-1)^{1.85}$, and $n_{max} = 56.34 \cdot (z-1)^{1.67}$. The obtained exponents b are to some extent in the vicinity of a quadratic relation, which is not surprising as the Coulomb energy is the driving, destabilising component in the polyanion. The deviation from an exponent value of 2 does indicate, however, that the counteracting, stabilising component is also dependent on the charge state, although its origin is not obvious from the mere values of b. However, based on previous work [10,14,22,33,34] we assume that the Coulomb barrier potential and the related electron-tunneling are responsible for this charge-dependent stabilising component. Thus, meta-stability comes into play, which suggests, that the parameters a and b in the fit functions are related to mean lifetimes of the respectively sized cluster polyanions. In order to follow this line of arguments, the corresponding (meta-)stability model for polyanions [22] is shortly reviewed and applied to the present data in Sections 4 and 5, respectively.

4. Theoretical methods

Determination of the appearance sizes under the consideration of polyanion lifetimes requires a theoretical input for data evaluation. A recently developed approach [22] determines polyanion abundances by two contributions: A cluster-size dependent decay rate for electron emission by tunneling and a size-independent rate for polyanion formation. This approach is fitted to the experimental polyanion yields, thus relating relative abundances to mean lifetimes of the polyanionic clusters and providing respective appearance sizes $n_{app,\tau}$. The approach is briefly outlined in the following, for more details refer to Ref. [22].

For calculation of the emission rate with respect to electron tunneling, the polyanionic cluster is assumed to be a metal sphere of radius $R = R_{WS} \cdot n^{1/3} + \delta$ with the Wigner-Seitz radius of aluminium, $R_{WS} = 0.158$ nm [35], and some electronic spill-out δ. A z-fold negatively charged cluster is treated as an electron bound in

the single-particle potential V_C of a $(z-1)$-charged cluster. This Coulomb-barrier potential is obtained by superposition of the Coulomb repulsion of a point charge and an image-charge contribution [36]:

$$V_C(r) = \frac{e^2}{4\pi\varepsilon_0}\cdot\left(\frac{z-1}{r} - \frac{R^3}{2r^2(r^2-R^2)}\right) . \quad (1)$$

The emission of an electron with mass m_e from the cluster by tunneling through this barrier is treated as a one-dimensional process, i.e. the electron motion is considered to be perpendicular to the cluster surface. Thus, the electron hits the potential barrier with its energy E. The probability for the tunneling process is calculated by the Wentzel-Kramers-Brillouin (WKB) approximation [16].

$$P_{WKB}(E) = \exp\left[-\int_{r_1}^{r_2}\left(\frac{8m_e}{\hbar^2}(V_C(r)-E)^{1/2}\right)dr\right] . \quad (2)$$

The integration is carried out in the range from r_1 to r_2, i.e. the distances at which $V_C(r) = E$. The binding energy of the electron is given by the electron affinity [37],

$$EA = W - \left((z-1)+\frac{1}{2}\right)\frac{e^2}{4\pi\varepsilon_0 R} , \quad (3)$$

if the $(z-1)$-charged cluster is in the ground state. Here, W is the bulk work function (for aluminium $W = 4.28$ eV [38]). However, as the clusters in the ClusterTrap experiments are close to room temperature due to thermalisation by buffer gas [22], a probability for thermal excitation is introduced [39],

$$L(T,E) = \ln\left(1+\exp\left[-\frac{E+EA}{kT}\right]\right) . \quad (4)$$

In combining both, the probabilities for tunneling (Eq. (2)) and for thermal excitation (Eq. (4)) for each electron energy (E) between 0 eV (vacuum level) and the maximum of the Coulomb barrier $V_{C,max}$, a term for a temperature-dependent field emission (FE) is obtained [22],

$$FE(T) = \int_0^{V_{C,max}} L(T,E)\cdot P_{WKB}(E)\cdot dE . \quad (5)$$

In addition, an expression for a thermionic emission (TE) above the Coulomb barrier is included in the model:

$$TE(T) = kT\cdot\exp\left[-\frac{EA+V_{C,max}}{kT}\right] . \quad (6)$$

However, TE is by more than six orders of magnitude smaller than FE for cluster temperatures well below 1000 K, as discussed in Ref. [22]. Both, field and thermionic emission are then combined to an electron emission density

$$\rho_{em} = \frac{4\pi m_e kT}{h^3}\cdot(TE+FE) , \quad (7)$$

which leads to an electron-emission rate

$$k_n = 4\pi R^2\rho_{em} \quad (8)$$

for a spherical cluster, that strongly depends on the cluster radius R (see also Eqs. (1) and (3)), and thus on the cluster size n.

Assuming an exponential polyanion decay by electron-emission, the respective emission rate describes a time-dependent polyanion abundance. Our analysis will address only the maximum charge state obtained for a given cluster size, because the less charged species will be stable ($EA \geq 0$) or close to stability ($EA \lesssim 0$), i.e. their electron emission is neglectable.

For the analysis of the experimental results, the formation rate of the highest-charged species has to be taken into account. Due to the complexity of simultaneous ion and electron storage and sequential electron attachment, the actual electron-attachment rates in the experiments are not known. From the duration of up to a few seconds required for the formation of higher charge states (Appendix A), we assume attachment rates on the same order of magnitude. Furthermore, the attachment rates have a size-dependency, too, as cross sections for the electron-cluster interaction have to be taken into account [22]. However, the attachment rates are considered to be nearly proportional to the cross-sectional area of the cluster, which is less sensitive to the cluster size than the electron-emission rates, the latter of which change over orders of magnitude in a range of only a few cluster sizes (Fig. 5). Therefore, the electron-attachment rates k_0 in the model are set to be size-independent. Overall, the size- and time-dependent polyanion abundance $A_{seq}(n, t)$ of the highest observed charge state is approximated by a two-step process, involving electron attachment and subsequent electron emission [22]. Note, that a feedback contribution of precursor ions $(z-1)$ - produced by electron emission from the z-ions - to the attachment rate is neglected. Similar to the Bateman-equation of nuclear physics [40,41], this ansatz yields

$$A_{seq}(n,t) = \frac{k_0}{k_n-k_0}\cdot\left(e^{-t\cdot k_0} - e^{-t\cdot k_n}\right) . \quad (9)$$

The abundance is calculated for an electron-bath duration $t = 1$ s, utilising the size-independent electron-attachment rate k_0 and an electron-emission rate, k_n, of Eq. (8). Thus, we obtain a polyanion abundance that is strongly related to the electron-emission rate and allows the assignment of a respective polyanion lifetime, $\tau_n = 1/k_n$, to a given cluster size. In the fit procedure of Eq. (9) to the experimental abundances, the electron-attachment rate k_0, the temperature T and the spill-out δ are used as free fit parameters.

5. Discussion

5.1. Appearance sizes of polyanionic clusters

The application of the field-emission approach (Section 4) to the present data sets (Section 3) requires the specification of a cluster-size range for the fit routine. To investigate the appearance of a charge state, the lower cluster-size limit for the fit routine is given by the minimum cluster size n_{min} (Table 1). In the exemplary case of $z = 8$, this is $n_{min} = 1010$. As the approach comprises the final electron attachment step to reach a charge state z, as well as the possibility of an electron-emission event, but does not include a 'decay' of the charge state by another electron attachment, an obvious choice for the upper cluster-size limit is given by the minimum cluster size of the next higher charge state, e.g. $n_{min} = 1312$ for $z = 9$ (Table 1). However, such a limit would cut the abundance curve of $z = 8$, even though the influence of the next higher charge state to the abundance of $z = 8$ might be marginal (Fig. 4). Another option for the upper cluster-size limit in the fit routine is the cluster size with the maximum abundance of the moving averages, e.g. $n_{max} = 1506$ for $z = 8$ (Fig. 2 and Table 1). But in this case, a significant nonaanion abundance of 18% affects the abundance curve of interest (Fig. 4). Thus, the cluster size $n_{max}(z)$ is not appropriate for the further evaluation. Instead, the upper cluster-size limit used for the fit routine has been chosen to be the

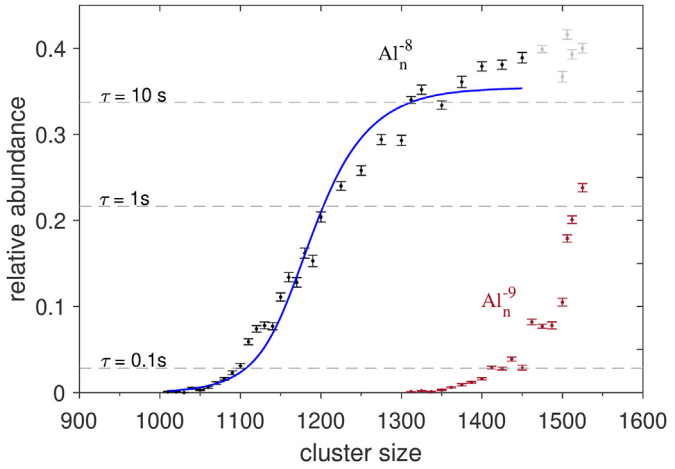

Fig. 4. Extraction from Fig. 2. Abundances of octaanionic clusters as a function of cluster size (black symbols) fitted by the field-emission approach (blue curve, $T = 558(22)$ K, $\delta = 0.98(9)$ Å, $k_0 = 0.44(2)$ s^{-1}). Grey symbols picture data points of Al_n^{-8} that have been excluded from the fit due to the uprising abundance of the next higher charge state, Al_n^{-9} (brown symbols).

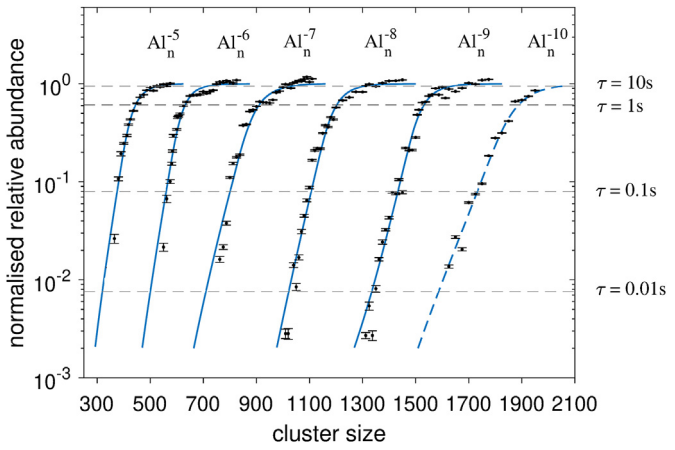

Fig. 5. Log-scale representation of relative abundances of charge states $z = 5$ to 10 as a function of the cluster size (black symbols), normalised to the saturation levels obtained from fits to the data (Eq. (9), blue curves). A horizontal line connects clusters of different size and charge state, but equal lifetime. The lifetime of 1 s (black line), coincides with the duration of the electron-bath. See text for further details.

cluster size, at which the abundance of the next higher charge state reaches 4%. At this abundance level, the influence of the next higher charge state is considered to be still neglectable. Thus, in case of octaanionic clusters, the relative abundances of $1010 \leq n \leq 1450$ are used for the application of the fit routine (Fig. 4).

The progression of the relative abundances is fitted using the field-emission approach (blue curve) with the resulting fit parameters temperature $T = 558(22)$ K, spill-out $\delta = 0.98(9)$ Å and electron-attachment rate $k_0 = 0.44(2)$ s^{-1}. The electron-attachment rate influences the saturation level of the fit curve, while the position and the slope of its increase are largely determined by both, temperature and spill-out. For example, a temperature of 0 K corresponds to a rather steep abundance increase of a polyanionic charge state. With increasing temperature, the slope of the abundance curve decreases, and the position of the rising slope is shifted to higher cluster-size values. This shift, however, is compensated by the spill-out parameter, i.e. by increasing the effective cluster radius. Therefore, the temperature and the spill-out parameters are strongly correlated. In Fig. 4, the curve assigns a mean lifetime τ to each relative abundance with respect to the fit saturation level. Note, that in the model approach the abundance of the saturation level corresponds to an infinite lifetime, i.e. stable polyanions. For example, Al_{1250}^{-8} has a mean lifetime of $\tau = 2.9$ s and, therefore, ions of this species created during the 1 s electron-bath are more likely to remain stable until their detection than the minimum cluster size Al_{1010}^{-8}, with $\tau = 7$ ms. All cluster sizes used for the fit routine are meta-stable, and thus can emit a surplus electron during the measurement cycle. The resulting heptaanion remains trapped and contributes to the signal of the precursor ions $(z - 1)$. Thus, such an emission is properly accounted for in the resulting relative polyanion abundance. In grey, data points of octaanions with $n > 1450$ are shown, which are excluded from the fit due to more and more competing abundance of nonaanions (Fig. 4, brown symbols).

In previous publications [11,22,33], the focus has been on the appearance sizes for $\tau = 1$ *s*, as it relates to the electron-bath duration of the experiment, t = 1 s. The cluster size with this lifetime ($n_{app,1s} = 1203(20)$, for $z = 8$) is identified by its relative abundance of $(1 - 1/e) \approx 63$ % with respect to the saturation level of the fit (Eq. (9), [22]). For the subsequent evaluation, other appearance sizes $n_{app,0.1s} = 1108(17)$ and $n_{app,10s} = 1309(26)$ for lifetimes of 0.1 s and 10 s are derived, respectively. These correspond to abundance levels of 8 % and 95 % with respect to the fit saturation level, respectively (Fig. 4, horizontal lines).

In Fig. 5, the application of the field-emission approach (blue curves) to the measured data (black symbols) is shown for the charge states $5 \leq z \leq 10$. For each z, the cluster-size range used for the fit is limited by $n_{min}(z)$ and by the cluster size, at which the next higher charge state reaches the 4 %-abundance, as described above. A variation of this abundance-limit to e.g. 2 % causes shifts of the appearance sizes of less than 1 %, which is covered by the uncertainties given for $n_{app,\tau}$ in Table 2.

The semi-logarithmic representation in Fig. 5 highlights data points of low abundance, i.e. those lying close to the minimum cluster sizes, n_{min}. In the present experiments, the lowest measured abundances correspond to lifetimes on the order of 10 ms. Note, that in Fig. 5 the measured cluster-ion abundance of each charge state is normalised to its respective saturation level of the fit. Thus, equal relative abundances correspond to equal lifetimes for all data sets, as illustrated by horizontal lines. As the lifetime of 1 s coincides with the electron-bath duration of the experiment, the corresponding horizontal line is highlighted in black. A point of intersection between a horizontal line and an abundance curve marks the cluster size, whose polyanion can be assigned to the respectively indicated lifetime τ.

As the data set for $z = 10$ does not reach a saturation level (compare Fig. 2), the respective fit curve is compromised.

Table 2
Fit parameters temperature *T*, spill-out δ, and electron-attachment rate k_0, as well as appearance sizes $n_{app,\tau}$ (for $\tau = 0.1$ s, 1 s and 10 s) of aluminium clusters of negative charge states $z = 2$ to 10. Values for $z = 2$, 3, 4 are re-evaluated from previous data [33]. Values written in italics are not reliable, see text for details.

z	*T*[*K*]	δ[Å]	$k_0[s^{-1}]$	$n_{app,\ 0.1\ s}$	$n_{app,\ 1\ s}$	$n_{app,\ 10\ s}$
2	561(5)	0.62(2)	0.98(11)	28(1)	30(1)	32(1)
3	541(6)	0.35(3)	0.56(2)	107(2)	117(2)	129(2)
4	553(25)	0.46(9)	0.48(5)	227(6)	248(7)	273(9)
5	758(8)	1.95(6)	0.77(2)	373(6)	443(8)	535(11)
6	656(9)	1.41(7)	0.54(2)	560(8)	632(9)	716(11)
7	687(19)	1.73(16)	0.47(2)	802(22)	912(28)	1043(35)
8	558(22)	0.98(9)	0.44(2)	1108(17)	1203(20)	1309(26)
9	485(6)	0.84(3)	0.46(2)	1434(6)	1532(6)	1637(7)
10	*560(11)*	*1.34(2)*	*0.17(2)*	*1743(17)*	*1891(22)*	*2057(28)*

Therefore, the appearance sizes of this charge state are calculated, but not included in the further evaluation.

All evaluated appearance sizes $n_{app,\tau}$ are summarised in Table 2 including the respective fit parameters. The uncertainties are discussed in Appendix B. Additionally, the present data analysis has been applied to data sets of di-, tri-, and tetraanionic aluminium clusters from previous work ([33], Appendix C), yielding re-evaluated appearance sizes that are included in Table 2. The corresponding measurements had been taken using the same experimental procedure, but were performed in a Penning trap with hyperbolically shaped electrodes and with a magnetic field of 5 T [33].

A closer inspection of the fit parameters reveals some variation depending on the charge state (Table 2). In the case of the attachment rates k_0, all values correspond to the duration of up to a few seconds required for conversion into higher charge states (Appendix A). While most rates are comparable to each other, the values for di- and pentaanionic clusters exceed the others. Differences in the attachment rate could be linked to variations of the electron-cluster interactions. Although we have taken great care to keep the experimental conditions constant for all charge states, the increased attachment-rate values indicate an increased number of stored electrons or a larger overlap between the reactants.

As mentioned in the discussion of Fig. 4, both fit parameters, spill out δ and temperature T, show some correlation. Therefore, we focus here on the temperature, only. The temperature values are rather a measure of internal cluster excitation than actual cluster temperatures as the model includes energy and temperature concepts valid for bulk matter [22]. A more realistic approach would have to consider the finite-size character of the free clusters. While the temperatures derived from measurements with the 5-T Penning trap tend to be lower than the values based on measurements with the 12-T setup, all fit temperatures are in the same order of magnitude. Furthermore, all values are above room temperature, which is expected due to the energy dissipation caused by the electron-attachment process.

Please note, that while setting a fixed temperature of e.g. 600 K for all charge states results in a change of the other fit parameters, the resulting appearance sizes regarding $\tau = 1$ s, $n_{app,\tau}$, for $z = 2$ to 8 agree within their uncertainties with those in Table 2. For $z = 9$, the appearance size shifts by 2 %, which is not fully covered by the uncertainty values. Overall, despite the variations in the fit parameters, all appearance-size values in Table 2 are treated as one common data set in the further discussion.

5.2. Dependencies between appearance sizes and charge states

For the first time, a comprehensive data set of appearance sizes $n_{app,\tau}$ of free metal gas-phase clusters is available over the charge-state range from $z = 2$ to 9. This allows us to study the dependence of appearance sizes on the charge state. The progression of the appearance sizes with the increasing charge is not intuitively transparent, because the charge state z is involved in the fundamentals of the model with two different dependencies, being the Coulomb barrier (Eq. (1)) and the electron affinity (Eq. (3)).

In Section 3 we fitted a power law to the minimum cluster size n_{min} and to the abundance maxima n_{max} (Fig. 3). Based on the model from Section 4 we learn that the sizes n_{min} are related to a lower mean lifetime than the sizes n_{max}, being approximately on the orders of 10 ms, and 100 s, respectively (Table 3). To analyse the effect of the polyanion lifetime on the relation between critical

Table 3
Parameters a and b of the fit function $n = a \cdot (z-1)^b$ applied to the minimum cluster size of a polyanionic charge state n_{min}, appearance sizes $n_{app,\tau}$ with $\tau = 0.1$ s, 1 s, and 10 s, as well as cluster size n_{max}, in Figs. 3 and 6.

	a	b
$n_{min}(\tau \sim 0.01$ s)	28.10 ± 1.99	1.85 ± 0.04
$n_{app}(\tau = 0.1$ s)	27.62 ± 2.33	1.90 ± 0.04
$n_{app}(\tau = 1$ s)	31.88 ± 1.93	1.86 ± 0.03
$n_{app}(\tau = 10$ s)	35.96 ± 5.07	1.84 ± 0.07
$n_{max}(\tau \sim 100$ s)	56.34 ± 20.44	1.67 ± 0.20

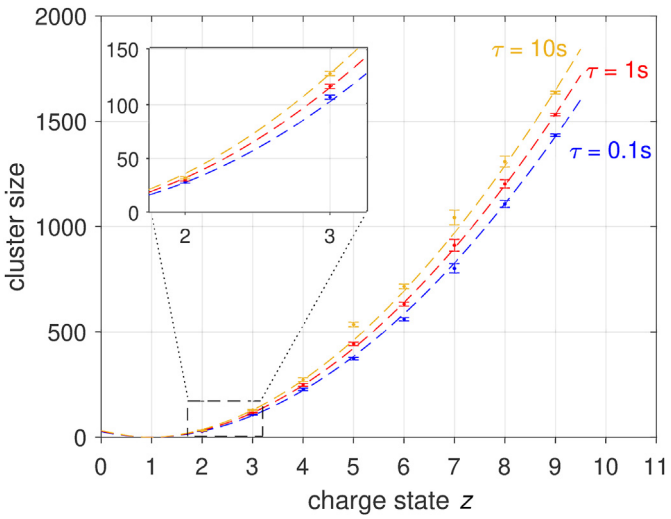

Fig. 6. Lifetime dependent appearance sizes $n_{app,\tau}$ as a function of the charge state z for $\tau = 0.1$ s (blue), 1 s (red) and 10 s (orange), respectively. Dashed lines are fits to the data, see text and Table 3 for details.

cluster sizes and charge state in more detail, the appearance sizes $n_{app,\tau}$ for $z = 2$ to 9 (Table 2) have been fitted with $n(z) = a \cdot (z-1)^b$, as described in Section 3. The resulting fit curves, shown in Fig. 6, reproduce the data points fairly well, except for some discrepancy for $z = 5$ and 7. However, these deviations are most probably due to experimental conditions, as the measurements for $z = 5$ and 7 show also some outlier values for the spill-out value δ and the cluster temperature T in Table 2.

Looking jointly at the fit parameters from Figs. 3 and 6, presented in Table 3, we note some general increase of the prefactor a, while the exponent of the power law remains at a mean value of $b \approx 1.86$, if the value for n_{max} is excluded. Note that the fits for n_{min} and n_{max} have to be considered less reliable than the $n_{app,\tau}$ results since the values n_{min} and n_{max} are basically singular data points being directly read from the abundance curves in Fig. 2. In particular n_{min} depends on the detection sensitivity of the experiment due to the small ion abundances involved. And the position of n_{max} in Fig. 2 is clearly affected by the appearance of the next higher charge state, i.e. representing two consecutive charge states, rather than a single one, which causes the larger uncertainties of the fit-parameters a and b for n_{max} (Table 3). In contrast, a $n_{app,\tau}$ value is an evaluation result of the complete increasing part of an abundance curve, and not only given by a single data point in Fig. 2.

Getting back to the fit parameters in Table 3, the exponent b appears to be constant, irrespective of the lifetime τ considered for

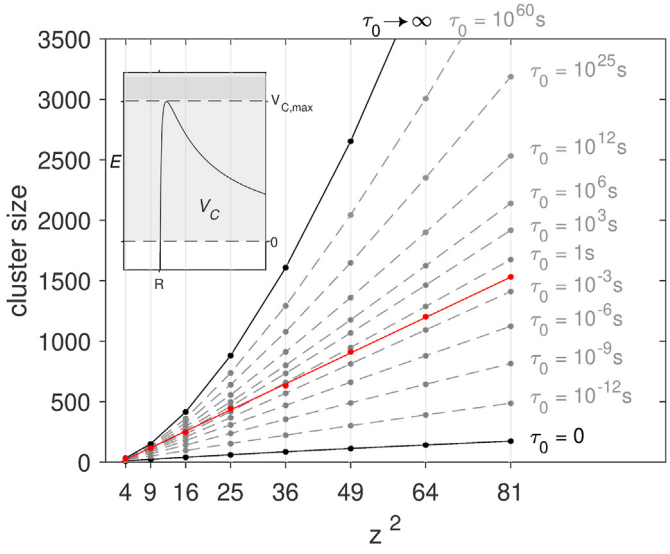

Fig. 7. Appearance sizes of aluminium clusters (grey symbols) as determined from calculated lifetimes τ_0 (Eq. (10)) as a function of z^2. Measured appearance sizes $n_{app,\tau}$ for $\tau = 1$ s from Table 2 (red symbols) and the limiting cases for $\tau_0 = 0$ and $\tau_0 \rightarrow \infty$ (black symbols) are highlighted. The inset shows a Coulomb-barrier potential (Eq. (1)) with different regions for the electron energy E. See text for details.

a certain appearance size, at least within the experimentally accessible time domain. On the other hand, the prefactor a clearly reflects the shift of the $n_{app,\tau}$ values in relation to the chosen lifetime τ. That means, the meta-stability aspect of the polyanions appears to be rather encoded in the prefactor, than in the exponent of the relation between appearance size and charge state.

To continue this line of investigation it is obvious to extend the range of appearance sizes with respect to the lifetime. However, from an experimental point of view, no data are available for sizes below the minimum cluster size, n_{min}. On the other hand, the extraction of $n_{app,\tau}$ values for larger lifetimes becomes less reliable, for three reasons. First, the relative abundances assigned to a given lifetime lie closer and closer to each other with increasing τ (horizontal lines in Fig. 5). Then, the abundance curves become flatter as they approach their saturation levels. And eventually, the appearance of the next charge state may overlay a decreasing effect on the abundance curve (Fig. 2). These effects prevent a proper assignment of appearance size for large lifetimes ($\tau > 100$ s).

Therefore, we continue this study on the ground of calculations, including the limiting cases of $\tau = 0$ and $\tau \rightarrow \infty$. As these limiting cases are clearly defined only for cold clusters, i.e. $T = 0$ K, we will restrict also our calculations of appearance sizes to this special case. The mathematical approach described in Section 4 is not suitable for this idealised case, as the electron-emission rate is $k_n = 0$ for $T \rightarrow 0$ K (Eqs. (4)–(8)). Instead, for a given cluster size the lifetime is calculated directly from the tunneling probability P_{WKB} (Eq. (2)) [12,42]:

$$\tau_0 = \frac{2r_1}{v(E)} \frac{1}{P_{WKB}(E)} \quad . \tag{10}$$

Here, an electron with energy E and velocity $v(E) = \sqrt{2E/m_e}$ hits the inner wall of the Coulomb barrier at distance r_1, similar to the treatment of alpha decays [43,44]. As any thermal excitation is omitted, E is given by the absolute value of the electron affinity $E = |EA|$ (Eq. (3)). Note, that any spill-out has been neglected here as well, because there is almost no data available regarding its role for polyanions, especially when treating a wide range of cluster sizes up to 2000 atoms.

Fig. 7 displays the calculated appearance sizes of polyanionic aluminium clusters as a function of the charge state for a variety of different lifetimes (grey symbols, dashed lines to guide the eye). Note, that the abscissa has been scaled by z^2 in order to facilitate the upcoming discussion.

Before evaluating Fig. 7 with regard to the lifetime of polyanions, we consider the two limiting cases (black symbols and lines). In general, a meta-stable polyanion will emit its electron instantaneously ($\tau = 0$), if the electron energy coincides with the top of the Coulomb barrier, $E = V_{C,max}$ (Fig. 7, inset), because the tunneling probability becomes $P_{WKB} = 1$. For the 0 K-case this limit is also expressed by the condition $|EA| = V_{C,max}$. Regarding the threshold sizes, this limit occurs at small cluster polyanions (Fig. 7, lower black line). Note, that in the experiments this limit cannot be measured, because a finite lifetime $\tau > 0$ is required to detect the polyanionic cluster.

The other limiting case in Fig. 7 is found at large clusters, in particular at the size where the electron affinity changes its sign. In general, if the electron energy E lies below the vacuum level (Fig. 7, inset), no tunneling occurs and the polyanion is stable ($\tau \rightarrow \infty$). The respective threshold is given by $E = 0$, and the corresponding cluster sizes are indicated by the upper black line in Fig. 7. As outlined above, this limit of large lifetimes is in principle accessible in experiments. However, an unambiguous assignment of the respective threshold cluster size is impeded by other constraints.

Appearance sizes $n_{app,\tau}$ for $0 < \tau_0 < \infty$ are exemplarily shown for a number of selected lifetimes as indicated in Fig. 7 (grey symbols and dashed lines). For all these cases, the electron energy is above vacuum level in the range $0 < E < V_{C,max}$ (Fig. 7, inset), with τ_0 decreasing for increasing E (Eq. (10)). For lifetimes around $\tau_0 = 1$ s the sizes seem to follow a straight line in Fig. 7, i.e. indicating a nearly quadratic relation, similar to the findings from Fig. 6. However, looking at the limiting case for $\tau_0 \rightarrow \infty$ (upper black line), the respective relation is clearly of higher order. And indeed, assuming no spill-out, from the special case of $|EA| = 0$ in Eq. (3) immediately follows the relation $n_{app,\ \tau=\infty} \sim (z - 1/2)^3$. For the limiting case $\tau_0 = 0$ (lower black line), the situation is not as obvious, however a closer inspection of the respective sizes (black symbols) yields an approximate relation of $n \sim (z-1)^{1.49}$, i.e. being less than quadratic. These findings show, that our initial assumption from the evaluation of Figs. 3 and 6, having a nearly constant exponent in the power-law dependence, is not valid if expanding the lifetime under consideration to its full range. At this point, it has to be noted that the $(z - 1)$-shift in the fit equations in Figs. 3 and 6, as well as the $(z - 1/2)$-shift for the limiting case of $\tau \rightarrow \infty$ is not expected to compromise the qualitative discussion of the power-law behaviour. Instead, these shifts in the z-dependencies, and in general the array of curves in Fig. 7 indicate, that the stability of polyanionic metal clusters with respect to electron emission constitutes a complex situation, which combines different aspects of polyanion stability in a changing weighting, when going from one lifetime limit to the other.

As the final aspect of this discussion, we focus on the experimentally relevant time range of 10 ms to 10 s (as indicated in Fig. 5) for the determination of appearance sizes. Added to Fig. 7 and

highlighted (red symbols, red line to guide the eye) are the experimentally determined appearance sizes $n_{app,\tau}$ for $\tau = 1$ s from Table 2. These measured sizes also follow roughly a straight line, due to the fit result $n \sim (z-1)^{1.86}$ from Fig. 3, being close to a quadratic relation. However, the experimental data deviate from the theoretical values for $\tau = 1$ s due to the neglect of any temperature- or spill-out effects in these calculations. A spill-out enlarges the effective cluster radius and thus lowers the appearance size. In contrast, thermal excitation of the cluster supports electron emission, resulting in a higher appearance size. Thus, an appropriate balance of both parameters, T and δ, in the model allows to reproduce experimental data, as shown by the fitting procedure in Section 5.1. While the obtained parameters in Table 2 pose reasonable values ($T \approx 600$ K, $\delta \approx 1$ Å), it remains uncertain how reliable these values are. Their accuracy may be improved by further refining the polyanion-stability model with respect to its basic assumptions, currently being a spherical cluster shape, an atomic density based on the Wigner-Seitz radius, a classical calculation of the electron affinity, and the image-charge potential forming the attractive part of the Coulomb barrier.

Nevertheless, the power-law fits of the appearance sizes (Fig. 6, Table 3) add a new aspect to the experimental studies of polyanion stability of metal clusters: They may provide a "short-cut tool" to predict appearance sizes of even higher charge states - at least within the experimentally accessible time domain, and once a certain data base is available. The question of predictability is closely related to the question, how element-specific quantities, like work function and atomic density inside the cluster, act on the parameters of the power-law fits. Thus, an extension of the presented studies to metal clusters of different elements appears to be the next step for continuing this line of research.

6. Conclusion

The appearance of polyanionic aluminium clusters with charge states $z = 5$ to 10 has been investigated as a function of the cluster size n. By a model including a temperature dependence, mean lifetimes τ have been assigned to clusters that form meta-stable polyanions with respect to electron field-emission. For the experimentally accessible lifetimes between 10 ms and 10 s, a systematic relationship of the form $n_{app,\tau} \sim (z-1)^{1.86}$ has been observed between the appearance sizes $n_{app,\tau}$ and the charge state z. Calculations for clusters at temperature $T = 0$ K indicate a continuous change of the functional dependence of $n_{app,\tau}$ and z between the limiting cases of the immediate emission of the electron and stable polyanion formation.

CRediT authorship contribution statement

Steffi Bandelow: Conceptualisation, Investigation, Methodology, Formal analysis, Visualisation, Writing - Original Draft. **Franklin Martinez:** Conceptualisation, Investigation, Methodology, Writing - Review and Editing. **Stephan König:** Formal analysis, Writing - Review and Editing. **Lutz Schweikhard:** Conceptualisation, Writing - Review and Editing, Supervision, Project administration, Funding Acquisition.

Declaration of competing interest

The authors declare that they have no known competing financial interests or personal relationships that could have appeared to influence the work reported in this paper.

Acknowledgements

This work was supported by the German Research Foundation (DFG) within the Collaborative Research Center (SFB) 652, project A03.

Appendix A. Electron attachment in a Penning trap

Fig. A8 displays the evolution of polyanion abundances as a function of the electron-bath duration for an exemplary cluster size of $n = 1250 \pm 8$. In this figure, individual measurements with an electron-bath duration between 1 ms and 8 s are shown. The abundance of each charge state at an individual electron-bath duration is normalised to the sum of all signals of the respective mass spectrum. For example, using an interaction time of clusters and electrons of 1 ms, 62 % of the ions remain in the monoanionic charge state, 36 % of the ions converted to the charge state $z = 2$ and only 1 % reached $z = 3$. Higher charge states were not detected. Please note, that the conversion observed for the electron-bath duration of 1 ms almost exclusively happened within the 20 ms electron pulse prior to the interaction time. While this fact is crucial for short interaction times, it is neglected for the standard electron-bath duration of 1 s.

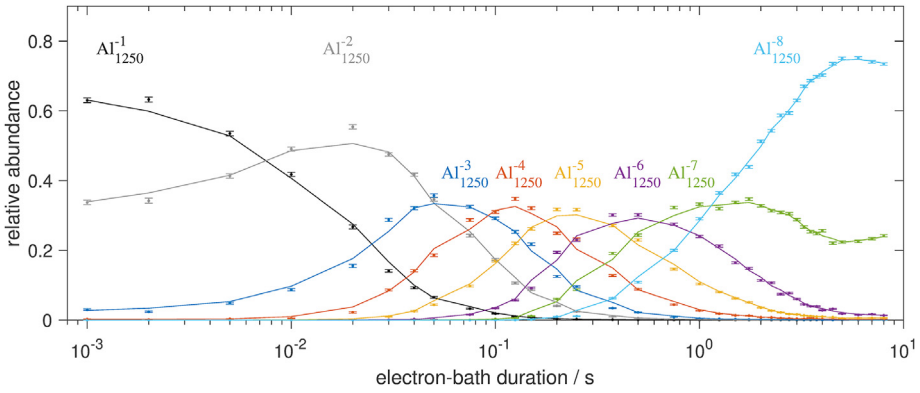

Fig. A.8. Relative abundances of polyanionic aluminium clusters $Al^{-z}_{1250\pm8}$ as a function of electron-bath duration. Moving averages of 5 data points are added as solid lines.

In general, higher negative charge states are reached by use of longer interaction times between electrons and cluster ions until a cluster-size dependent maximum charge state is formed, which is $z = 8$ in case of Al_{1250}. Simultaneously, the abundance of lower charge states decreases, due to ongoing conversions. As the increase of each abundance curve can be linked to the decrease of the previous charge state, a sequential electron attachment process is indicated.

After an interaction-time of about 4s, the abundance increase of octaanionic clusters stops. We believe this effect is linked to an energy loss of the stored electrons. For all measurements, an axial Penning-trap trapping-depth of 23 eV has been used. Thus, electrons with energies up to this limit are captured in the Penning trap. During the electron-cluster interaction-time, electron-energy decreases by radiation due to the radial motion in the magnetic field of 12 T. At the same time, a minimum electron energy is needed for the production of a z-fold negatively charged cluster, as the Coulomb barrier of a cluster with $(z - 1)$ charges has to be overcome for electron attachment. In the present example of $n = 1250$, Coulomb-barrier heights range from 0.4 eV for the production of dianions to 4.3 eV for the attachment of the 8th electron (Eq. (1)). When the maximum electron-energy drops below this level, the production of octaanionic clusters stops.

Appendix B. Uncertainties of n_{min}, n_{max}, and $n_{app,\tau}$

Regarding the definition of appearance sizes and their uncertainties, two cases are distinguished. On the one hand, the minimum n_{min} and maximum n_{max} cluster sizes are considered, which are directly determined with respect to their abundances (Section 3). Here, uncertainties are calculated by the full widths at half maximum (FWHM) of the monoanion signal, as the monoanion-abundance covers a certain size distribution, which is assumed to be maintained during the conversion of charge states.

In contrast, the lifetime-dependent appearance sizes $n_{app,\tau}$ originate from a fit-analysis of the polyanion abundances (Section 5) and thus, depend on the three fit-parameters T, δ, and k_0 as well as their individual uncertainties. Due to the complexity of the underlying math (Section 4 and the references therein), an analytical error propagation to calculate the uncertainties of $n_{app,\tau}$ values was not feasible. Instead, each fit parameter is systematically varied by subdividing its uncertainty range into 10 equal segments, resulting in 11 segment limits for each of the three fit parameter. For every of the 11^3 possible fit-parameter combinations, an individual abundance curve, and thus, an individual value for one and the same appearance size, is calculated. The mean value of this dataset agrees with the original fit value of $n_{app,\tau}$, while the standard deviation σ is used as its uncertainty.

Appendix C. Re-evaluation of appearance sizes of Al^{-z} for z = 2, 3, 4

To increase the available dataset of appearance sizes, relative abundances of aluminium di-, tri-, and tetraanions [33] are re-evaluated. The data were taken at a previous version of the ClusterTrap setup, having a hyperbolic trap in a 5-T field. By changing the trap geometry and replacing the magnet, the mass-to-charge limit of the Penning trap has been increased by a factor of ~ 20 [21], which enabled the investigation of bigger clusters and thus, the present measurements.

Fig. C9 shows the abundance data of polyanions for $z = 2$, 3, 4 [33] as well as re-evaluated fits in the same way as the data for $z = 5$ to 10 in Fig. 5. The abundance progression for each charge state is fitted by use of the present model (Section 4). The values of the three fit parameters as well as appearance sizes for lifetimes of 100 ms, 1 s and 10 s are given in Table 2. Data evaluation in Ref. [33] also used WKB-calculations to estimate lifetimes, based on electron tunneling probabilities through the Coulomb barrier (Eq. (10), Section 5.2), but neglected any thermal excitation of the clusters. Comparing previous and recalculated appearance sizes for lifetimes of 1 s, the value for the dianion $n_{app,1s} = 30$ remains unchanged. Also, for $z = 3$ and 4, only minor changes of the appearance sizes from 113 to 117(2) and from 250 to 248(7) are found, respectively.

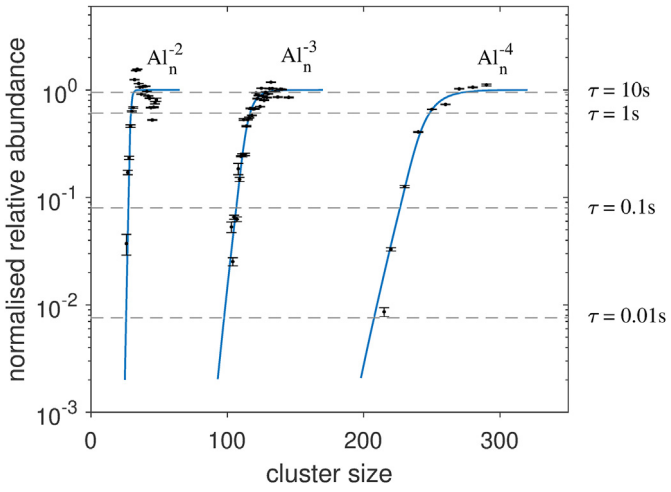

Fig. C.9. Experimental data from Ref. [33] (black symbols) are displayed and processed in the same way as the data in Section 5.1 and Fig. 5, yielding respective fit curves (blue lines) and lifetime assignments (horizontal lines).

References

[1] B.K. Rao, P. Jena, Evolution of the electronic structure and properties of neutral and charged aluminum clusters: A comprehensive analysis, J. Chem. Phys. 111 (5) (1999) 1890–1904, https://doi.org/10.1063/1.479458.

[2] J.A. Alonso. Structure and Properties of Atomic Nanoclusters, 2nd ed., Imperial College Press, 2011. https://doi.org/10.1142/p784.

[3] P. Jena, Q. Sun, Super atomic clusters: Design rules and potential for building blocks of materials, Chem. Rev. 118 (11) (2018) 5755–5870, https://doi.org/10.1021/acs.chemrev.7b00524.

[4] U. Näher, S. Bjørnholm, S. Frauendorf, F. Garcias, C. Guet, Fission of metal clusters, Phys. Rep. 285 (6) (1997) 245–320, https://doi.org/10.1016/s0370-1573(96)00040-3.

[5] M. Vogel, A. Herlert, L. Schweikhard, Photodissociation of small group-11 metal cluster ions: Fragmentation pathways and photoabsorption cross sections, J. Am. Soc. Mass Spectrom. 14 (6) (2003) 614–621, https://doi.org/10.1016/S1044-0305(03)00203-4.

[6] S. König, A. Jankowski, G. Marx, L. Schweikhard, M. Wolfram, Fission of polyanionic metal clusters, Phys. Rev. Lett. 120 (2018), 163001, https://doi.org/10.1103/PhysRevLett.120.163001.

[7] P. Fischer, L. Schweikhard, Photofragmentation of $Bi_n^{+/-}$ clusters (n=2-19) in an electrostatic ion beam trap, Eur. Phys. J. D 73 (105) (2019) 5, https://doi.org/10.1140/epjd/e2019-100027-0.

[8] A. Goldberg, J. Oliva, N. Walsh, F. Martinez, G. Marx, L. Schweikhard, A. Fernández-Barbero, Stability and electron affinities of negatively charged aluminium clusters: a computational study, Afinidad 66 (2009) 285–292.

[9] L.v. Szentpály, Multiply charged anions, maximum charge acceptance, and higher electron affinities of molecules, superatoms, and clusters, Acta Phys. Chim. Sin. 34 (6) (2018) 675, https://doi.org/10.3866/PKU.WHXB201801021.

[10] N. Walsh, F. Martinez, G. Marx, L. Schweikhard, F. Ziegler, Multiply negatively charged aluminium clusters II. - production of Al_n^{3-}, Eur. Phys. J. D 52 (1–3) (2009) 27–30, https://doi.org/10.1140/epjd/e2008-00255-3.

[11] N. Walsh, F. Martinez, G. Marx, L. Schweikhard, F. Ziegler, First observation of a tetra-anionic metal cluster, Al_n^{4-}, J. Chem. Phys. 132 (1) (2010), 014308 https://doi.org/10.1063/1.3270153.

[12] X.-B. Wang, C.-F. Ding, L.-S. Wang, Electron tunneling through the repulsive Coulomb barrier in photodetachment of multiply charged anions, Chem. Phys. Lett. 307 (5–6) (1999) 391–396, https://doi.org/10.1016/s0009-2614(99)00543-6.

[13] A. Dreuw, L.S. Cederbaum, Multiply charged anions in the gas phase, Chem.

Rev. 102 (1) (2002) 181–200, https://doi.org/10.1021/cr0104227.
[14] F. Martinez, N. Iwe, M. Müller, K. Raspe, L. Schweikhard, J. Tiggesbäumker, K.-H. Meiwes-Broer, Cresting the Coulomb barrier of polyanionic metal clusters, Phys. Rev. Lett. 126 (2021), 133001, https://doi.org/10.1103/PhysRevLett.126.133001.
[15] A. Herlert, L. Schweikhard, Production of dianionic and trianionic noble metal clusters in a Penning trap, Int. J. Mass Spectrom. 229 (1) (2003) 19–25, https://doi.org/10.1016/S1387-3806(03)00251-3.
[16] X.-B. Wang, L.-S. Wang, Experimental search for the smallest stable multiply charged anions in the gas phase, Phys. Rev. Lett. 83 (17) (1999) 3402–3405, https://doi.org/10.1103/physrevlett.83.3402.
[17] J. Friedrich, P. Weis, J. Kaller, R.L. Whetten, M.M. Kappes, Alkali halide cluster dianions: Metastability and threshold sizes, Eur. Phys. J. D 9 (1) (1999) 269–272, https://doi.org/10.1007/s100530050438.
[18] A. Herlert, S. Krückeberg, L. Schweikhard, M. Vogel, C. Walther, First observation of doubly charged negative gold cluster ions, Phys. Scripta T80 (B) (1999) 200, https://doi.org/10.1238/physica.topical.080a00200.
[19] L. Schweikhard, S. Krückeberg, K. Lützenkirchen, C. Walther, The Mainz Cluster Trap, Eur. Phys. J. D 9 (1) (1999) 15–20, https://doi.org/10.1007/s100530050391.
[20] F. Martinez, G. Marx, L. Schweikhard, A. Vass, F. Ziegler, The new ClusterTrap setup, Eur. Phys. J. D 63 (2) (2011) 255–262, https://doi.org/10.1140/epjd/e2011-10528-3.
[21] F. Martinez, S. Bandelow, C. Breitenfeldt, G. Marx, L. Schweikhard, A. Vass, F. Wienholtz, Upgrades at ClusterTrap and latest results, Int. J. Mass Spectrom. 365–366 (2014) 266–274, https://doi.org/10.1016/j.ijms.2013.12.018.
[22] F. Martinez, S. Bandelow, G. Marx, L. Schweikhard, A. Vass, Abundances of tetra-, penta-, and hexa-anionic gold clusters, J. Phys. Chem. C 119 (20) (2015) 10949–10957, https://doi.org/10.1021/jp510947p.
[23] H. Weidele, U. Frenzel, T. Leisner, D. Kreisle, Production of “cold/hot” metal cluster ions: A modified laser vaporization source, Z. Physik D Atoms, Mol. Clust. 20 (1991) 411–412, https://doi.org/10.1007/BF01544024.
[24] J. Richards, R. Huey, J. Hiller, A new operating mode for the quadrupole mass filter, Int. J. Mass Spectrom. Ion Phys. 12 (4) (1973) 317–339, https://doi.org/10.1016/0020-7381(73)80102-0.
[25] S. Bandelow, G. Marx, L. Schweikhard, The stability diagram of the digital ion trap, Int. J. Mass Spectrom. 336 (2013) 47–52, https://doi.org/10.1016/j.ijms.2012.12.013.
[26] Z.P. Gotlib, G.F. Brabeck, P.T.A. Reilly, Methodology and characterization of isolation and preconcentration in a gas-filled digital linear ion guide, Anal. Chem. 89 (7) (2017) 4287–4293, https://doi.org/10.1021/acs.analchem.7b00356.
[27] G. Savard, S. Becker, G. Bollen, H.-J. Kluge, R. Moore, T. Otto, L. Schweikhard, H. Stolzenberg, U. Wiess, A new cooling technique for heavy ions in a Penning trap, Phys. Lett. A 158 (5) (1991) 247–252, https://doi.org/10.1016/0375-9601(91)91008-2.
[28] F. Martinez, S. Bandelow, C. Breitenfeldt, G. Marx, L. Schweikhard, F. Wienholtz, F. Ziegler, Lifting of the trapping potential during ion storage for multi-anion production in a Penning trap, Int. J. Mass Spectrom. 313 (2012) 30–35, https://doi.org/10.1016/j.ijms.2011.12.009.
[29] F. Chandezon, S. Tomita, D. Cormier, P. Grübling, C. Guet, H. Lebius, A. Pesnelle, B.A. Huber, Rayleigh instabilities in multiply charged sodium clusters, Phys. Rev. Lett. 87 (15) (2001), https://doi.org/10.1103/physrevlett.87.153402.
[30] C. Harris, A.J. Stace, Coulomb fission in multiply-charged ammonia clusters: Accurate measurements of the Rayleigh instability limit from fragmentation patterns, J. Phys. Chem. A 122 (10) (2018) 2634–2644, https://doi.org/10.1021/acs.jpca.8b00815.
[31] F.R.S. Lord Rayleigh, XX. On the equilibrium of liquid conducting masses charged with electricity, Philos. Mag. 14 (87) (1882) 184–186, https://doi.org/10.1080/14786448208628425.
[32] I. Last, Y. Levy, J. Jortner, Beyond the Rayleigh instability limit for multicharged finite systems: From fission to Coulomb explosion, Proc. Natl. Acad. Sci. U.S.A. 99 (14) (2002) 9107–9112, https://doi.org/10.1073/pnas.142253999.
[33] F. Martinez, S. Bandelow, C. Breitenfeldt, G. Marx, L. Schweikhard, F. Wienholtz, F. Ziegler, Appearance size of poly-anionic aluminum clusters, Al_n^{z-}, z=2-5, Eur. Phys. J. D 67 (39) (2013), https://doi.org/10.1140/epjd/e2012-30265-3.
[34] X.-B. Wang, L.-S. Wang, Photoelectron spectroscopy of multiply charged anions, Annu. Rev. Phys. Chem. 60 (1) (2009) 105–126, https://doi.org/10.1146/annurev.physchem.59.032607.093724.
[35] C. Kittel, Einführung in die Festkörperphysik, fourteenth ed., Oldenbourg Wissenschaftsverlag, London, U.K., 1994.
[36] J.D. Jackson, Classical Electrodynamics, 3rd ed., Wiley, New York, 1998.
[37] J.P. Perdew, Energetics of charged metallic particles: From atom to bulk solid, Phys. Rev. B 37 (11) (1988) 6175–6180, https://doi.org/10.1103/physrevb.37.6175.
[38] M.A. Hoffmann, G. Wrigge, B.v. Issendorff, Photoelectron spectroscopy of mathrm$Al^-_{mathit32000}$: Observation of a “Coulomb staircase” in a free cluster, Phys. Rev. B 66 (2002), 041404, https://doi.org/10.1103/PhysRevB.66.041404.
[39] M.S. Sodha, P.K. Kaw, Field emission from negatively charged solid particles, J. Phys. D 1 (10) (1968) 1303–1307, https://doi.org/10.1088/0022-3727/1/10/310.
[40] H. Bateman, Solution of a system of differential equations occurring in the theory of radioactive transformations, Proc. Camb. Phil. Soc. 15 (1910) 423–427.
[41] J.-V. Kratz, K.H. Lieser, Nuclear and Radiochemistry, Wiley VCH Verlag GmbH, 2013.
[42] L. Schweikhard, A. Herlert, S. Krückeberg, M. Vogel, C. Walther, Electronic effects in the production of small dianionic gold clusters by electron attachment on to stored Au_n, n = 12-28,, Philos. Mag. B 79 (9) (1999) 1343–1352, https://doi.org/10.1080/13642819908216975.
[43] G. Gamow, Zur Quantentheorie des Atomkernes, Z. Phys. 51 (3) (1928) 204–212, https://doi.org/10.1007/BF01343196.
[44] R.W. Gurney, E.U. Condon, Quantum mechanics and radioactive disintegration, Phys. Rev. 33 (1929) 127–140, https://doi.org/10.1103/PhysRev.33.127.

Article II

International Journal of Mass Spectrometry 336 (2013) 47–52

Contents lists available at SciVerse ScienceDirect

International Journal of Mass Spectrometry

journal homepage: www.elsevier.com/locate/ijms

The stability diagram of the digital ion trap

Steffi Bandelow*, Gerrit Marx, Lutz Schweikhard

Institute of Physics, Ernst Moritz Arndt University, 17489 Greifswald, Germany

ARTICLE INFO

Article history:
Received 5 October 2012
Received in revised form
19 December 2012
Accepted 19 December 2012
Available online 3 January 2013

Keywords:
Ion storage
Paul trap
Radio-frequency trap
Digital ion trap
Stability diagram

ABSTRACT

The Paul trap with a rectangular driving field, known as digital ion trap (DIT) has been investigated by mapping the stability diagram, i.e., measuring the relative storage efficiency with respect to the trapping parameters, and comparison to the conventional Paul trap with harmonic guiding field. The results show that the performance of the DIT can be described in terms of the conventional trap, when the trapping parameters are redefined according to the zeroth and first order Fourier component of the driving field. The higher harmonics seem to have only little influence.

1. Introduction

Since the invention of the radio-frequency (RF) trap by Paul in 1953 [1] this principle of ion confinement has been used for a wide range of scientific investigations, from analytical chemistry to fundamental physics and quantum computing [2–4]. The ion motion in a quadrupolar geometrical arrangement of a harmonic electric field, the guiding field, is governed by the Mathieu equation [5]. The solutions of this equation include stable and unstable ion trajectories depending on the storage parameters. The stability regions are visualised best by the so-called stability diagram [6]. The stable motions can be approximated by harmonic modes with well defined frequencies. In addition, instability lines have been found within the stable regions [7].

Already in 1973 Richards introduced an alternative for the temporal function of the guiding field, namely rectangular instead of sinusoidal waveforms [8,9]. Such a digital ion trap (DIT) can be realised by switching between two voltages, which avoids the use of resonant circuits. The DIT allows one to change the driving frequency over a wide range almost without limitations in the height of the voltages, which means one can easily vary the range of storable ions, with respect to their mass-to-charge ratios.

However, this development was not followed up until recently, when analytical [12,13,10,11] and simulation studies [14,15] as well as experimental proofs-of-principle investigations [16–18] of the DIT were reported. In the present study a new description of the digital ion trap is introduced, based on results of Koizumi et al. [13] and Ding et al. [14]. In addition, the stability diagram of the DIT has been mapped and compared to the harmonic case for a three-dimensional Paul trap with hyperbolic ring and endcap electrodes. Furthermore, the frequency of the radial macro motion has been probed for a specific AC-only trapping mode. In addition, the stability diagram has been investigated for the case where the DC component is applied solely by varying the duty cycle. The RF-trap basics and the nomenclature are reviewed in the next section before the experimental setup and results are described in Sections 3 and 4, respectively, along with the corresponding interpretations.

2. Theory

In the following we consider a hyperbolic RF ion trap, consisting of a ring electrode and two endcaps (Fig. 1). The general form of its potential is given by [19]

$$\Phi(r, z, \Omega t) = \frac{\Phi_0(\Omega t)}{2(r_0^2/2 + z_0^2)}(r^2 - 2z^2) \quad (1)$$

and is realised experimentally by application of a temporally-periodic potential difference $\Phi_0(\Omega t)$ between hyperbolic electrodes. Ω is the angular frequency of the guiding field. Beside the AC component (of amplitude V_0) an additional DC component (U_0) may be applied. r_0 and z_0 are defined by the minimal distance between the centre of the trap to the ring electrode and the endcaps, respectively [19].

* Corresponding author. Tel.: +49 03834 864756.
E-mail address: bandelow@physik.uni-greifswald.de (S. Bandelow).

1387-3806/$ – see front matter © 2013 Elsevier B.V. All rights reserved.
http://dx.doi.org/10.1016/j.ijms.2012.12.013

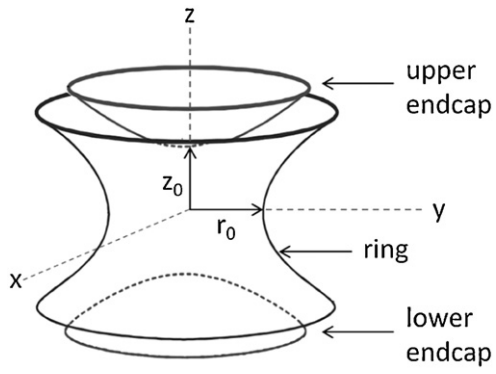

Fig. 1. Hyperbolic Paul trap, consisting of two endcaps and a ring electrode.

2.1. Harmonically driven quadrupole ion trap

In the case of the harmonically driven Paul trap the potential difference $\Phi_0(\Omega t) = \Phi(r = r_0,\ z = 0,\ \Omega t) - \Phi(r = 0,\ z = z_0,\ \Omega t)$ can be written as

$$\Phi_0(\Omega t) = U_0 + V_0 \cos(\Omega t). \tag{2}$$

The equation of motion results in the standard Mathieu equation [5]

$$\frac{d^2\eta}{d\sigma^2} + (a_\eta - 2q_\eta \cos(2\sigma))\eta = 0 \quad \text{with } \eta = r, z \tag{3}$$

by introducing the dimensionless parameters for particles with mass m and charge Q:

$$\begin{aligned} a_z &= -2a_r = -\frac{8QU_0}{m(r_0^2/2 + z_0^2)\Omega^2}, \\ q_z &= -2q_r = \frac{4QV_0}{m(r_0^2/2 + z_0^2)\Omega^2} \\ \text{and} \qquad \sigma &= \frac{\Omega t}{2}. \end{aligned} \tag{4}$$

The combination of a_η and q_η is sufficient to define the stability or instability of the ion trajectory. The $a_\eta - q_\eta$ plane, well known as stability diagram, is divided into regions of stable and unstable solutions.

Trapped ions oscillate with angular frequencies

$$\omega_{k,\eta} = 2\pi\nu_{k,\eta} = (2k \pm \beta_\eta)\frac{\Omega}{2} \quad \text{with } k = 0, \pm1, \pm2, \ldots \tag{5}$$

where the β_η are functions of a_η and q_η only.

When the sum of integer multiples of the motional angular frequencies $k_r\omega_r$, $k_z\omega_z$ is equal to an integer multiple of the angular driving field frequency $k_r\omega_r + k_z\omega_z = k\Omega$, ions can gain energy, and thus, the amplitude of their trajectories increases until they leave the trap. As a result, instability lines are found within stable regions of the stability diagram [7,20].

2.2. Digital ion trap (DIT)

In a DIT the sinusoidal (*AC*) component of the trapping voltage is replaced by a periodic rectangular signal $f(t)$ with $2\pi/\Omega = T$ for $n \in \mathbb{Z}$ (Fig. 2)

$$f(t) = \begin{cases} +V_R \text{ for } nT < t \le nT + \tau \\ -V_R \text{ for } nT + \tau < t \le (n+1)T. \end{cases} \tag{6}$$

In his seminal publication, Richards introduced a "duty cycle" $d = \tau/T$ to describe the relative durations of the positive component of the rectangular driving field (and thus also the negative, $1 - d$) [8].

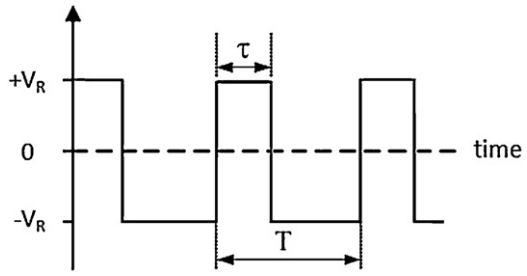

Fig. 2. Rectangular driving voltage used for ion confinement in a digital ion trap.

Table 1
Magnitudes M_n of Fourier components of function Eq. (6).

n	$\Omega/2\pi$	M_n/V_R
0	0	$2d - 1$
1	$1/T$	$\frac{4}{\pi}\lvert\sin(\pi d)\rvert$
2	$2/T$	$\frac{2}{\pi}\lvert\sin(2\pi d)\rvert$
3	$3/T$	$\frac{4}{3\pi}\lvert\sin(3\pi d)\rvert$

Obviously, for $d \neq 0.5$ there is a non-zero DC component given by $(2d - 1) \cdot V_R$ [14]. This is confirmed by a Fourier analysis [21] for the argument t

$$S(t) = \frac{a_0}{2} + \sum_{n=1}^{\infty}\left[a_n \cos(n\Omega t) + b_n \sin(n\Omega t)\right] \tag{7}$$

which also reveals all harmonic components. a_n and b_n are the Fourier coefficients of the order n:

$$\begin{aligned} a_n &= \frac{1}{\pi}\int_0^{2\pi/\Omega} f(t)\cdot \cos(n\Omega t)\Omega\, dt \quad \text{and} \\ b_n &= \frac{1}{\pi}\int_0^{2\pi/\Omega} f(t)\cdot \sin(n\Omega t)\Omega\, dt \end{aligned} \tag{8}$$

for $n = 0, 1, 2, \ldots$ The magnitude M_n of Fourier components

$$\begin{aligned} M_0 &= \frac{a_0}{2} \qquad\qquad \text{and} \\ M_n &= \sqrt{a_n^2 + b_n^2} \quad \text{for } n = 1, 2, 3, \ldots \end{aligned} \tag{9}$$

describes the strength of the guiding field at the corresponding frequency. In Table 1 and Fig. 3 the normalised amplitudes M_n/V_R of the first Fourier components ($n = 0$–3) are listed and plotted, respectively.

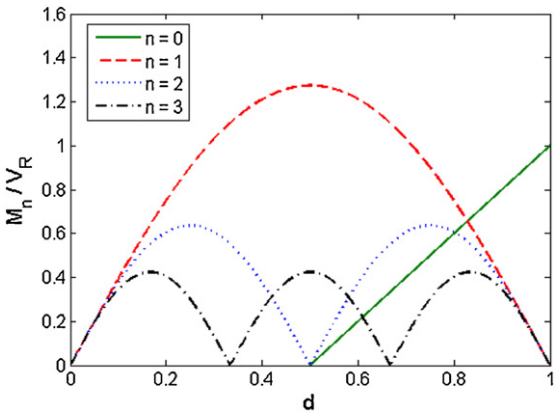

Fig. 3. Normalised magnitudes of Fourier components for $n = 0$ (solid line, not shown for $d < 0.5$, where the linear trend continues for M_0, however with negative sign), $n = 1$ (dashed line), $n = 2$ (dotted line) and $n = 3$ (dashed-dotted line).

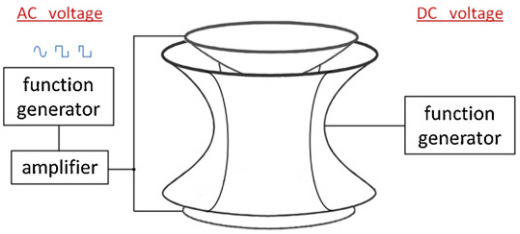

Fig. 4. Application of trapping voltages to the trap electrodes. The sinusoidal or rectangular AC voltages are applied to the endcaps. The DC component is applied to all four segments of the ring electrode.

As the experimental results show (Section 4), the zeroth and the first order magnitude components are sufficient to rewrite Eq. (2) to describe the guiding field potential of the corresponding harmonically driven RF-trap:

$$\Phi_0(\Omega t) \approx U_0 + M_0 + M_1 \cdot \cos(\Omega t). \tag{10}$$

Thus, this description also leads to a reformulation of the dimensionless trapping parameters:

$$\begin{aligned} a_z &= -2a_r = -\frac{8Q \cdot (U_0 + M_0)}{m(r_0^2/2 + z_0^2)\Omega^2} \\ q_z &= -2q_r = \frac{4Q \cdot M_1}{m(r_0^2/2 + z_0^2)\Omega^2}. \end{aligned} \tag{11}$$

These equations are used to transfer a stability diagram, measured in the U_0–V_R plane, into the $a-q$ plane (Figs. 5 and 6). The transfer of the borders of stability from the a–q into the U_0–V_R plane (Figs. 8 and 9), is given by:

$$\begin{aligned} U_0 &= -\frac{a_z}{8Q}\frac{m(r_0^2/2 + z_0^2)\Omega^2}{} - M_0 \\ V_R &= \frac{q_z}{4Q}\frac{m(r_0^2/2 + z_0^2)\Omega^2}{M_1/V_R}. \end{aligned} \tag{12}$$

The ion motional frequencies for a digital ion trap can be calculated by Eq. (5), utilising the redefined trapping parameters (Eq. (11)).

3. Experimental setup and procedure

The experimental setup has been described in [22]. In short, an asymptotically-symmetric [23] hyperbolic Paul trap (Fig. 4) with copper electrodes of size $r_0 = 7$ mm and $z_0 = r_0/\sqrt{2}$ is used for all present measurements. The ring electrode is split into four 90° segments which allow a dipolar excitation for the investigation of the radial resonance frequencies of the macro-motion [22]. All measurements have been performed with singly-charged argon ions, Ar^+, which were created during a 3 ms electron-impact ionisation of argon. The gas was inserted into the vacuum chamber via a leak valve. The pressure was about 1×10^{-4} Pa, i.e., about an order of magnitude above the residual-gas pressure. The frequency of the driving field applied to the endcap electrodes (see Fig. 4) was $\Omega/2\pi = 450$ kHz, provided by a function generator (Stanford Research, DS345) and a voltage amplifier (FLC Electronics, A400DI). The DC voltage, produced by another function generator (Stanford Research, DS345), was applied to the ring segments. The application of the driving voltages in this scheme does not affect the trapping parameters (Eqs. (4) and (11)). After a storage time of 50 ms, the ions were extracted from the trap by an amplitude ramp [24,25] and counted by a channeltron detector with conversion dynode at a distance of 5.0 mm from 3.3-mm diameter central hole of the upper endcap. To create well-defined conditions for the next cycle, the driving field was switched off for 10 ms. The experimental sequence

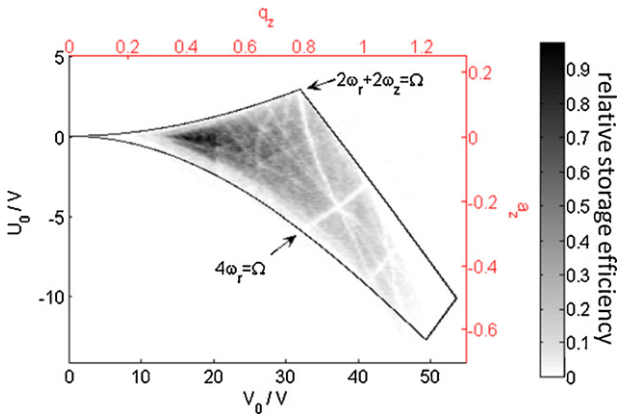

Fig. 5. Measured stability diagram of a harmonically driven ion trap plotted as a function of driving voltages (left and bottom axes) and stability parameters (right and top axes). Solid lines represent the calculated borders of stability. Two instability lines are marked.

was executed by a LabVIEW-based control system [26]. For the device triggering a FPGA card was used as a pulse-pattern generator [27].

In the case of the stability-diagram measurements, the experimental cycle (ionisation, storage, detection, preparation for next cycle) was repeated 250 times for each set of trapping parameters a and q. The amplitudes of the DC and AC voltages were changed in steps of 0.1 V and 0.38 V, respectively.

For the exploration of the radial resonance frequencies (Section 4.3) the storage conditions were kept constant. For the last 5 ms of the storage time, an additional dipolar RF-excitation voltage of frequency f_{ex} was applied to two pairs of adjacent ring segments. When the frequency of this excitation was equal to the radial ion motional frequency $f_{ex} = \nu_r$, resonance effects caused a loss of ions. For normalisation of the ion counts, this cycle with RF excitation was alternated with a second one, in which no excitation was applied. As for the stability diagram, this experimental sequence was repeated 250 times. The excitation frequency was scanned from 1 kHz to 450 kHz in steps of 0.5 kHz.

4. Results and discussion

4.1. Stability diagram of the harmonical RF ion trap

For comparison, the Paul trap described Section 2.1 has been operated in the harmonical mode, i.e., with a sinusoidal driving voltage. The contour plot of Fig. 5 shows the observed stability diagram, where the number of ion counts as a function of the trapping parameters q (on the x-axis) and a (on the y-axis) is indicated by levels of gray on a scale from zero (white) to the maximum number (black). The solid lines mark the predicted borders of the stability region in the a–q plane as discussed by McLachlan ([5], pp. 16–18).

The expectations and measured data are in good agreement. The maximal storage efficiency ($\gtrsim 90\%$) is found in the region from $q_z = 0.40$ to 0.50 and between $a_z = 0.00$ and 0.03. As expected, lines of instabilities are found. The two most dominant are the ones for $2\omega_r + 2\omega_z = \Omega$ and $4\omega_r = \Omega$.

4.2. Stability diagram of the DIT for d = 0.5

As a first example of a stability diagram of a DIT Fig. 6 shows the diagram for a rectangular driving field with a duty cycle $d = 0.5$. As before, the (now rectangular) RF signal $f(t)$ was fed to the endcap electrodes while the DC term is applied to the ring. In analogy to Fig. 5 the relative storage efficiency is plotted in levels of gray as a function of the amplitude of the (rectangular) driving signal and

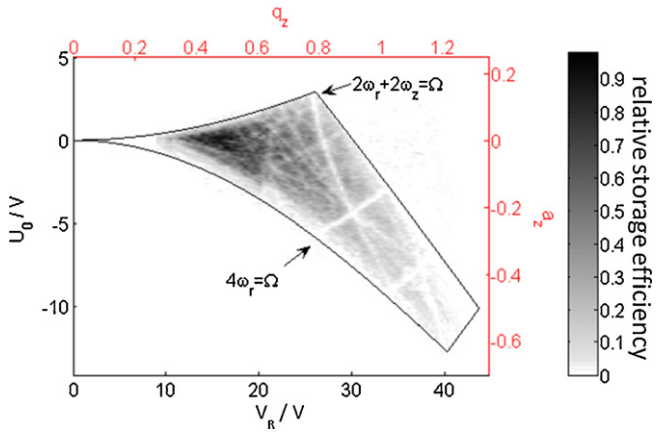

Fig. 6. Measured stability diagram of a digitally driven ion trap with $d = 0.5$ plotted as a function of driving voltages (left and bottom axes) and stability parameters (right and top axes). Solid lines represent the calculated borders of stability. Two instability lines are marked.

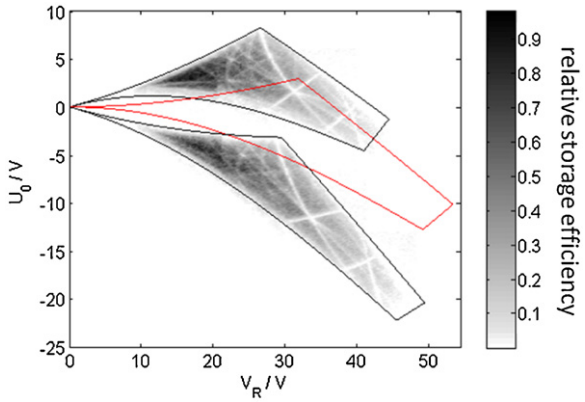

Fig. 8. Measured stability diagrams of a digitally driven ion trap with $d = 0.4$ (top) and $d = 0.6$ (bottom) plotted as function of driving voltages. Solid lines represent the calculated borders of stability for digitally (black) and harmonically (red) driven traps, respectively. (For interpretation of the references to colour in this figure legend, the reader is referred to the web version of the article.)

DC voltage and simultaneously by the a_z and q_z parameters. For the scaling between the driving-signal amplitude V_R and q_z the 1st order Fourier component of the DIT signal has been used, as suggested by Koizumi et al. [13]. Note, however, that $M_1 = 1.23 \cdot V_R$ has been used instead of the value $4/\pi$ for an ideal rectangular function. The experimental value resulted from a Fourier transformation of the measured actual "rectangular" RF signal.

With this scaling of the RF-fields, the measured stability diagrams in the $a_z - q_z$ plane of the conventional Paul trap with sinusoidal RF-field (Fig. 5) and of the DIT (Fig. 6) are practically indistinguishable, both with respect to the borders of the stable regions as well as with respect to the positions and depths of the instability lines.

4.3. Resonances of the radial ion motion

To further investigate this similarity between the sinusoidal and the digital ion trap a radial dipolar excitation (Section 3) has been applied in both trapping modes. The results are presented in Fig. 7.

In both spectra a resonance at the fundamental frequency $\nu_{0,r}$ is detected and fitted by a Gaussian curve for evaluation (not shown). The resulting resonance frequencies 66.80(4) kHz and 66.68(5) kHz for the sinusoidal and digital trapping mode, respectively, agree with theoretical expectations (Eq. (5), $k = 0$). In addition, however much less clearly visible, first order motional frequencies [28] (Eq. (5), $k = 1$) for sinusoidal and digitally driven trap are detected at $\nu_{1,r} = 382.54(34)$ kHz and $\nu_{1,r} = 383.35(28)$ kHz.

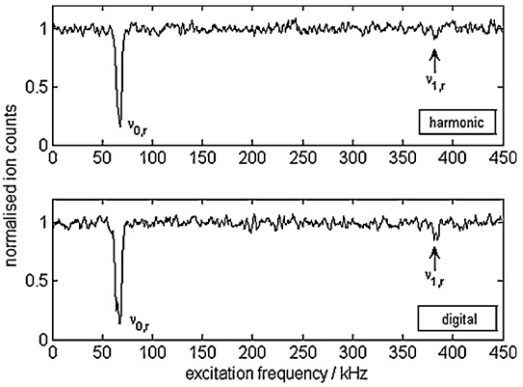

Fig. 7. Resonance spectra (ion counts as a function of excitation frequency) for argon ions confined by harmonic (top) and digital (bottom) trapping fields (a_z, $q_z = 0.00$, 0.81), respectively. The excitation amplitude was about 40 mV.

While additional resonances may have been expected for the digital ion trap as compared to the harmonically driven ion trap no such further resonances have been observed. This confirms the findings from the stability-diagram study that the higher harmonics of the DIT driving field have no significant influence on the ion motion.

4.4. Stability diagrams of the DIT for $d \neq 0.5$

One of the main advantages of the DIT is the possibility to produce a DC component by an uneven application of the positive and the negative polarity of the rectangular signal, i.e., by a duty cycle $d \neq 0.5$. To probe this option, storage efficiency measurements as in Figs. 5 and 6 have been performed for $d = 0.4$ and $d = 0.6$. The respective stability diagrams are shown in Fig. 8.

The stable regions are compressed and rotated with respect to those of the standard diagram. As in the case of the $d = 0.5$ DIT the Fourier components of the rectangular RF signal can be considered. For M_1 this is 1.21 for both $d = 0.4$ and 0.6. Again, the actual signal applied differed slightly and the components were measured to be 1.20, and 1.08. The rotation around the origin of the x, y-plane (see Fig. 8) can be traced back to the d-dependent DC component M_0 (as given in Table 1). This allows one to transform the borders of the stability region from a harmonically driven trap (red lines in Fig. 8) to their positions for $d = 0.4$ and 0.6 (black lines). The respective stability diagrams in the $a_z - q_z$ plane (not shown), are barely distinguishable from those of the sinusoidal and the $d = 0.5$ digitally ion trap (Figs. 5 and 6).

For Fig. 9 the inverse transformation $(a_z, q_z) \rightarrow (U_0, V_R)$ Eq. (12) has been used to calculate the borders for a selection of d values, namely $d = 0.1, 0.2, \ldots, 0.9$. Note, that this procedure assumes that M_2 and higher orders of the Fourier analysis of the rectangular RF field can be neglected. While this is adequate for $d = 0.5$ the other components gain in relative strength further away from the symmetric case (compare Fig. 3). Thus, the validity of the assumption for extreme d values still is to be investigated, which is out of the scope of the present study.

4.5. The d–V_R diagram of the DIT

The previous section has extended the DIT from the symmetric $d = 0.5$ to asymmetric cases. Following the traditional way of mapping the stability diagram for a given d, the RF-amplitude V_R and

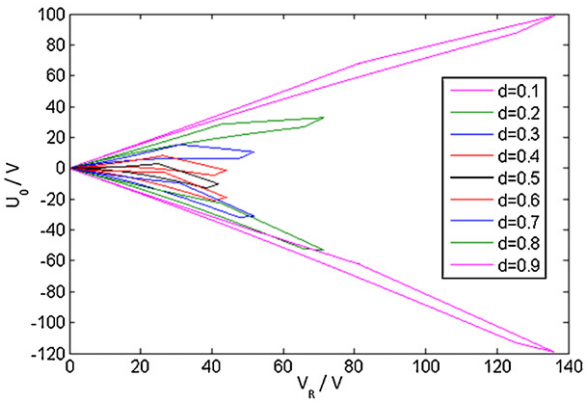

Fig. 9. Calculated borders of stability diagrams for digitally driven ion traps with duty cycles $d = 0.1, 0.2, \ldots, 0.9$ (top to bottom) for argon ions confined in a hyperbolic Paul trap with $r_0 = 7$ mm using $\Omega/2\pi = 450$ kHz.

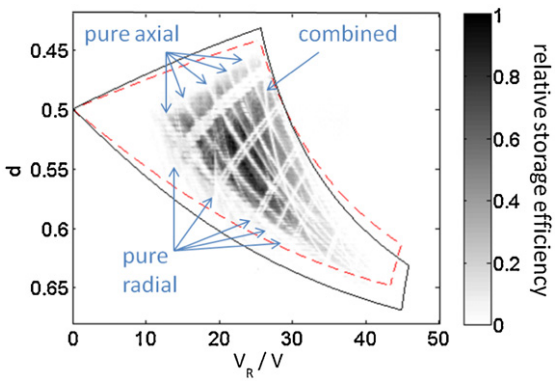

Fig. 11. Measured d–V_R diagram. Solid and dashed lines represent the borders of the stability region, as adapted to the experimental Fourier coefficients and as calculated from the ideal square-well functions, respectively. In blue, pure radial, pure axial and combined instability lines are marked. (For interpretation of the references to colour in this figure legend, the reader is referred to the web version of the article.)

the DC potential U_0 have been varied. However, from Eq. (11) follows that an additional DC-component M_0 is introduced by the RF signal voltage for $d \neq 0.5$. This DC-component can be used to map the whole stability diagram by scanning d and V_R alone, i.e., without an additional DC potential U_0.

Fig. 10 shows on the left the conventional stability diagram. The dashed lines indicate how one proceeds within the diagram for a given d value when the amplitude V_R is increased.

Between $d \cong 0.4425$ and $d \cong 0.6475$ all lines of constant d intersect the stability region. For other values of the duty cycle the DC component is too strong to allow for stable solutions of the Mathieu equation (Eq. (3)). Recalculating the voltages V_R at the points of intersection with the stability borders, the DIT stability diagram can be plotted in a d–V_R representation (Fig. 10, right).

Fig. 11 shows an experimental d–V_R diagram. The dashed lines represent the theoretical borders as described above, the full lines are calculated from the measured Fourier components, i.e., the M_0 and M_1 terms. The data exhibit very strong instability lines. Especially the pure axial and pure radial ones are visible. The latter reveal a double structure, probably an artifact due to the splitting of the ring electrode (see also [22]) for radial dipolar excitation (Section 4.3). This is in contrast to the previous sections. A possible reason may be the modified experimental conditions, as for this measurement the guiding field voltage was applied to the ring electrode to allow ion extraction by a pulsed voltage on the lower endcap.

Thus, for the present measurements the storage efficiency of this DIT operation mode seems to be somewhat lower than for the case of a separate addition of the DC component as performed in the conventional sinusoidal and digital ion trap. However, it still comes with the advantage that both the AC and the DC component of the trapping field are carried by just one signal defined by the parameters V_R and d.

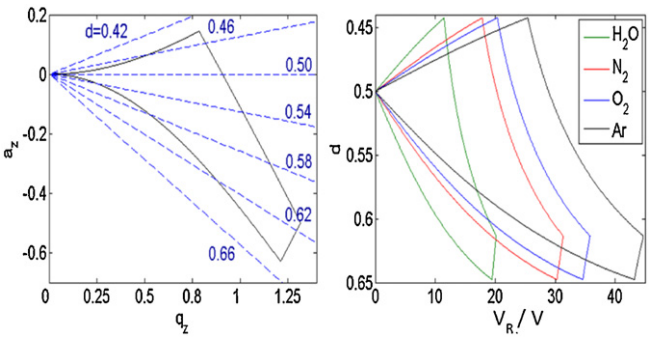

Fig. 10. Relation between a_z, q_z and different duty cycles $d = 0.42, 0.46, \ldots, 0.66$ (left). Calculated stability borders in the d–V_R diagram for H_2O, N_2, O_2 and Ar (from left to right).

5. Conclusion

The digital ion trap has been investigated by a series of experiments, in particular, the mapping of the stability diagram under various conditions. The measurements show that essentially only the zeroth and first order Fourier component of the rectangular guiding field voltage have to been taken into account for the description in terms of the traditional a and q parameters. Stretched and rotated stability diagrams of digital ion traps in the U_0–V_R plane result from the magnitude of the Fourier components. Appropriate implementation of these effects into the trapping parameters results in a common stability diagram in the a_z–q_z plane for harmonic and for digital traps. The new approach, presented in this study, offers a convenient method to calculate storage properties of digital ion traps, like borders of the stability regions, ion motional frequencies and trapping instabilities, fundamental for further research and applications.

Acknowledgements

The project was supported by a Collaborative Research Center of the DFG (SFB 652-TP A03). S. Bandelow acknowledged a postgraduate stipend from the state of Mecklenburg-Vorpommern (Landesgraduiertenförderung).

References

[1] W. Paul, H. Steinwedel, Ein neues Massenspektrometer ohne Magnetfeld, Zeitschrift für Naturforschung 8a (1953) 448.
[2] P. Dawson, Quadrupole Mass Spectrometry and its Applications, AIP Press, Woodbury, New York, 1995.
[3] G. Werth, V. Gheorghe, F. Major, Charged Particle Traps II, Springer-Verlag, Berlin, Heidelberg, 2009.
[4] R.E. March, J.F.J. Todd, Practical Aspects of Trapped Ion Mass Spectrometry V, CRC Press, Boca Raton, Florida, 2010.
[5] N. McLachlan, Theory and Application of Mathieu Functions, 1st ed., Oxford University Press, Oxford, 1951.
[6] W. Paul, O. Osberghaus, E. Fischer, Forschungsberichte des Wirtschafts- und Verkehrsministeriums Nordrhein-Westfalen 415 (1958).
[7] R. Alheit, S. Kleineidam, F. Vedel, M. Vedel, G. Werth, Higher order non-linear resonances in a Paul trap, International Journal of Mass Spectrometry and Ion Processes 154 (1996) 155.
[8] J.A. Richards, R.M. Huey, J. Hiller, A new operating mode for the quadrupole mass filter, International Journal of Mass Spectrometry and Ion Physics 12 (1973) 317.

[9] J.A. Richards, Quadrupole mass filter spectrum control using pulse width modulation, International Journal of Mass Spectrometry and Ion Physics 24 (1977) 219.
[10] M. Sudakov, E. Nikolaev, Ion motion stability diagram for distorted square waveform trapping voltage, European Journal of Mass Spectrometry 8 (2002) 191.
[11] N.V. Konenkov, M. Sudakov, D.J. Douglas, Matrix methods for the calculation of stability diagrams in quadrupole mass spectrometry, Journal of the American Society for Mass Spectrometry 13 (2002) 597.
[12] L. Ding, S. Kumashiro, Ion motion in the rectangular wave quadrupole field and digital operation mode of a quadrupole ion trap mass spectrometer, Rapid Communications in Mass Spectrometry 20 (2006) 3.
[13] H. Koizumi, W.B. Whitten, P.T.A. Reilly, E. Koizumi, Derivation of mathematical expressions to define resonant ejection from square and sinusoidal wave ion traps, International Journal of Mass Spectrometry 286 (2009) 64.
[14] L. Ding, M. Sudakov, S. Kumashiro, A simulation study of the digital ion trap mass spectrometer, International Journal of Mass Spectrometry 221 (2002) 117.
[15] J. Lee, M.A. Marino, H. Koizumi, P.T.A. Reilly, Simulation of duty cycle-based trapping and ejection of massive ions using linear digital quadrupoles: the enabling technology for high resolution time-of-flight mass spectrometry in the ultra high mass range, International Journal of Mass Spectrometry 304 (2011) 36.
[16] L. Ding, F.L. Brancia, Electron capture dissociation in a digital ion trap mass spectrometer, Analytical Chemistry 78 (2006) 1995.
[17] A. Berton, P. Traldi, L. Ding, F.L. Brancia, Mapping the stability diagram of a digital ion trap (DIT) mass spectrometer varying the duty cycle of the trapping rectangular waveform, Journal of the American Society for Mass Spectrometry 19 (2008) 620.
[18] F.L. Brancia, B. McCullough, A. Entwistle, J.G. Grossmann, L. Ding, Digital asymmetric waveform isolation (DAWI) in a digital linear ion trap, Journal of the American Society for Mass Spectrometry 21 (2010) 1530.
[19] F. Major, V. Gheorghe, G. Werth, Charged Particle Traps, Springer-Verlag, Berlin, Heidelberg, 2005, pp. 3–4.
[20] Y. Wang, J. Franzen, K.P. Wanczek, The non-linear resonance ion trap. Part 2. A general theoretical analysis, International Journal of Mass Spectrometry and Ion Processes 124 (1993) 125.
[21] I.N. Bronstein, K.A. Semendjajew, G. Musiol, H. Mühlig, Taschenbuch der Mathematik, 5th ed., Verlag Harri Deutsch, Frankfurt am Main, 2001, 436.
[22] S. Bandelow, G. Marx, L. Schweikhard, A split-ring Paul trap for dipolar excitation of the radial ion motion and ellipticity studies, European Physical Journal D 61 (2011) 315.
[23] R.D. Knight, The general form of the quadrupole ion trap potential, International Journal of Mass Spectrometry and Ion Physics 51 (1983) 127.
[24] R.L. Alfred, F.A. Londry, R.A. March, Resonance excitation of ions stored in a quadrupole ion trap. Part IV. Theory of quadrupolar excitation, International Journal of Mass Spectrometry and Ion Processes 125 (1993) 171.
[25] D.E. Goeringer, R.I. Crutcher, S.A. McLuckey, Ion remeasurement in the radio frequency quadrupole ion trap, Analytical Chemistry 67 (1995) 4164.
[26] D. Beck, K. Blaum, H. Brand, F. Herfurth, S. Schwarz, A new control system for ISOLTRAP, Nuclear Instruments & Methods in Physics Research Section A 527 (2004) 567.
[27] F. Ziegler, D. Beck, H. Brand, H. Hahn, G. Marx, L. Schweikhard, A new pulse-pattern generator based on LabVIEW FPGA, Nuclear Instruments & Methods in Physics Research Section A 679 (2012) 1.
[28] X.Z. Chu, M. Holzki, R. Alheit, G. Werth, Observation of high-order motional resonances of an ion cloud in a Paul trap, International Journal of Mass Spectrometry and Ion Processes 173 (1998) 107.

Article III

International Journal of Mass Spectrometry 353 (2013) 49–53

Contents lists available at ScienceDirect

International Journal of Mass Spectrometry

journal homepage: www.elsevier.com/locate/ijms

The 3-state digital ion trap

Steffi Bandelow*, Gerrit Marx, Lutz Schweikhard

Institute of Physics, Ernst Moritz Arndt University, 17487 Greifswald, Germany

ARTICLE INFO

Article history:
Received 23 April 2013
Received in revised form 3 June 2013
Accepted 3 June 2013
Available online 14 June 2013

Keywords:
Ion storage
Paul trap
Radio-frequency trap
Digital ion trap
3-State digital ion trap
Stability diagram

ABSTRACT

A new type of digital ion trap is introduced, namely a Paul trap with 3-state digital driving voltages. The stability diagram has been mapped, i.e. the relative storage efficiency with respect to the trapping parameters has been measured. The results show, that the performance of the 3-state digital ion trap can be described in terms of the conventional (2-state) digital ion trap, where the trapping parameters are defined, again, according the zeroth and first order Fourier component of the driving field.

1. Introduction

Interaction studies of molecules with electrons are of importance in modern biochemistry and medicine, as phenomena like electron attachment [1,2] and electron capture/transfer dissociation [3–5] serve as the base for peptide sequencing [6,7] and analysis of DNA damages [8–10].

The experiments can be performed by overlapping molecule and electron beams in crossed beam experiments with well defined energies, or by use of ion traps. The latter method allows one to observe delayed reactions on extended time scales and to store charged reaction products. Unfortunately, the commonly used Paul traps [11,12] do not allow the storage of molecules and electrons at the same time due to their different masses [13,14]. This is in contrast to the storage behaviour of Penning traps which have only an upper mass limit [15] and thus can be employed to, e.g., simultaneously store large metal clusters and electrons for the production of polyanionic systems [16–18]. In order to provide electrons for the interaction with ions in Paul traps, two different procedures have been developed. In both approaches, a low-energy electron beam is guided through the Paul trap, while the ions are stored by AC fields.

In the first case [19,20] linear Paul traps, driven by sinusoidal AC voltages are used. Electrons pass this trap type along the symmetry axis, where the amplitude of the quadrupolar electric guiding field is zero. A superimposed magnetic field enhances the transfer efficiency of the electrons. However, all electrons that are not exactly on the trap axis are influenced by the radio-frequency field.

Alternatively, interaction studies are performed within hyperbolic Paul traps driven by rectangular AC voltages (digital ion trap), which are applied to the ring electrode only [21]. Aside from the actual switching periods, the potential is constant in time. An electron beam with an energy of several eV above the respective trap centre potential is guided axially through the trap. While the electron interaction energy is well defined for each position along the axis, it varies with position. As the radio-frequency voltage is generally rather high this introduces a large spread of interaction energies.

In the present study a new scheme for the operation of linear as well as hyperbolic Paul traps is introduced, in which field-free interaction studies with defined energies of the reactants will be possible. To this end, digital AC trapping voltages with three different voltage levels are introduced. One of them is a *zero*-volt level, for potential-free periods within every AC-cycle. Stability diagrams have been measured for different types and lengths of zero-volt level implementation to study the influence of this operation scheme to the ion trapping. The theoretical description of the 3-state digital ion trap is presented in the next section before the experimental setup and results are described in Sections 3 and 4, respectively, along with the corresponding interpretations.

2. Theory

2.1. The 2-state digital ion trap

In preparation for the new development we first review the hyperbolic radio-frequency (RF) ion trap operated with a rectangular driving signal $f(t)$ of amplitude V_R and fundamental frequency $\Omega/2\pi = 1/T$ (Fig. 1) as introduced by Richards et al. [22,23]. The "duty

* Corresponding author. Tel.: +49 3834 864756.
E-mail address: bandelow@physik.uni-greifswald.de (S. Bandelow).

1387-3806/$ – see front matter © 2013 Elsevier B.V. All rights reserved.
http://dx.doi.org/10.1016/j.ijms.2013.06.003

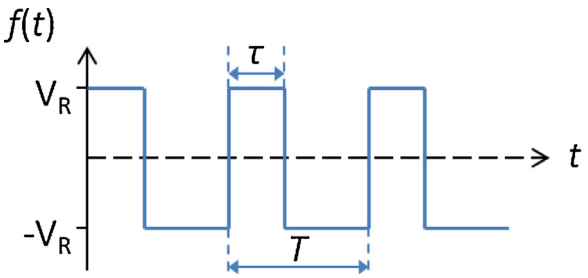

Fig. 1. Rectangular AC component of the driving signal used for ion confinement in a 2-state digital ion trap.

cycle" d describes the relative duration of the positive component $d = \tau/T (0 \le d \le 1)$ of the rectangular driving signal, and therefore also of the negative component $(T-\tau)/T = 1-d$. For duty cycles $d \neq 0.5$ a DC-component (M_0) is generated by the AC driving signal, with an amplitude depending on d [24]. In addition to this M_0-component, a further DC voltage U_0 might be applied, as well known from the conventional, harmonically driven RF ion trap.

By application of the AC and DC driving voltages between the ring and the endcap electrodes a potential

$$\Phi(r,z,t) = \frac{\Phi_0(t)}{2(r_0^2/2 + z_0^2)}(r^2 - 2z^2) \tag{1}$$

is generated to confine particles with mass m and charge Q. The potential difference Φ_0 is specified further below (Eq. (4)). r_0 and z_0 are the minimal distances from the trap centre to the ring and endcap electrodes, respectively (compare Fig. 4).

The trajectories of charged particles trapped in a conventional RF ion trap are described by the Mathieu equation [25]. The same mathematical description can be applied to the 2-state digital ion trap (2S-DIT) [26]: A Fourier analysis decomposes the rectangular driving signal $f(t)$ into a DC-component of amplitude

$$M_0 = (2d-1)\cdot V_R \tag{2}$$

and n ($n = 1, 2, 3, \ldots$) AC-components of frequencies $\Omega/2\pi = n/T$ and magnitudes

$$M_n = \frac{4}{n\pi}\cdot\left|sin(n\pi d)\right|\cdot V_R. \tag{3}$$

Only the magnitudes of the zeroth and first order Fourier components, M_0 and M_1 respectively, are of importance for the trapping potential of the 2S-DIT [26]. Thus, in the following the potential $\Phi_0(t)$ is approximated by

$$\Phi_0(t) = U_0 + f(t) \simeq U_0 + M_0 + M_1\cdot\cos(\Omega t), \tag{4}$$

which results in the dimensionless stability parameters

$$a_z = -2a_r = -\frac{8Q\cdot(U_0+M_0)}{m(r_0^2/2+z_0^2)\Omega^2}$$
$$q_z = -2q_r = \frac{4Q\cdot M_1}{m(r_0^2/2+z_0^2)\Omega^2} \quad . \tag{5}$$

Using these definitions, the stability diagram, which characterises the storage conditions [27], is identical for all duty cycles d, when plotted in the $a-q$ plane [26]. In contrast, for every duty cycle d there is a different stability diagram when plotted as a function of the driving voltages U_0 and V_R.

2.2. The 3-state digital ion trap

By including a third potential ($\neq \pm V_R$) in the time-pattern of the digital driving signal $f(t)$ we now introduce a 3-state digital ion trap (3S-DIT) (Fig. 2). In the following, for simplicity, this third level will be a *zero*-volt potential. It may either follow both, the positive and negative components $\pm V_R$, i.e. occur twice during each period (Fig. 2, top), or follow just one of the components, i.e. occur only once during a period of the driving signal (Fig. 2, bottom). In the following, the first case is referred to as being a "symmetric implementation" of zero-volt levels in the time pattern of the driving signal, the latter as being an "asymmetric implementation".

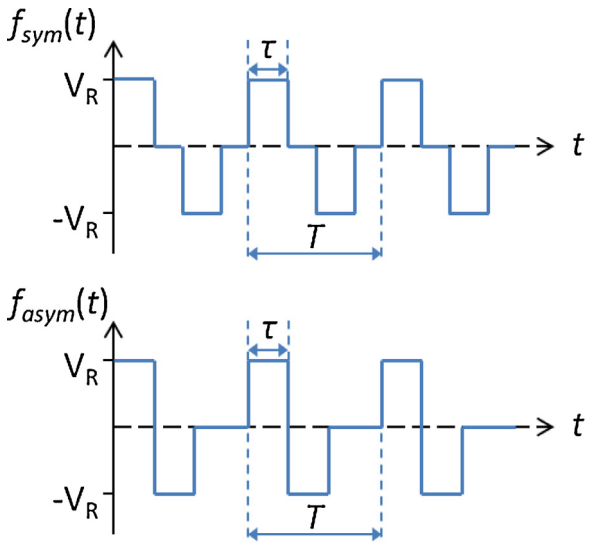

Fig. 2. Rectangular AC component of the driving signals used for ion confinement in the 3S-DIT. Top: symmetric implementation of zero-volt potentials in the time-pattern of the driving signal. Bottom: asymmetric implementation of zero-volt potential.

Table 1
Magnitudes M_n of Fourier components for symmetric and asymmetric time-patterns

	n	M_n
Symmetric time-pattern	0, 2, 4... 1, 3, 5...	0 $\frac{4}{n\pi}\cdot\lvert sin(n\pi d)\rvert\cdot V_R$
Asymmetric time-pattern	0 1, 2, 3...	0 $\frac{4}{n\pi}\cdot sin^2(n\pi d)\cdot V_R$

We restrict the present investigation to the case that both, the positive and the negative component ($\pm V_R$) have the same duration τ. Hence, no DC-component M_0 is generated by the AC driving signals. We keep the duty-cycle definition of the 2S-DIT, $d = \tau/T$. Obviously, its range is now restricted to $0 \le d \le 0.5$. For a duty cycle of $d = 0$, the driving signal has no AC components. The storage of particles is not possible. The maximum duty cycle of $d = 0.5$ of the 3S-DIT is identical with a $d = 0.5$ 2S-DIT.

As stated above, for the description of the 2S-DIT, the definition of the potential and the trapping parameters can be approximated by the zeroth and first order Fourier component of the driving signal (Eqs. (1), (4) and (5)). We assume the same for the 3S-DIT which will be justified by the experimental results (Section 4). Thus, the magnitudes of the Fourier components of the 3S-DIT with symmetric and asymmetric implementation of the zero-volt levels in the time-pattern of the driving signals are given as listed in Table 1.

In Fig. 3 the (non-zero) normalised magnitudes M_n/V_R ($n = 1$, 3, 5) and M_n/V_R ($n = 1$–5) of the 3S-DIT with symmetric (top) and asymmetric implementation (bottom) of the zero-volt levels in the time-pattern of the driving signals, respectively, are plotted as a function of the duty cycle d.

3. Experimental setup and procedure

The experimental setup and the sequence for measuring stability diagrams have already been described in detail, elsewhere

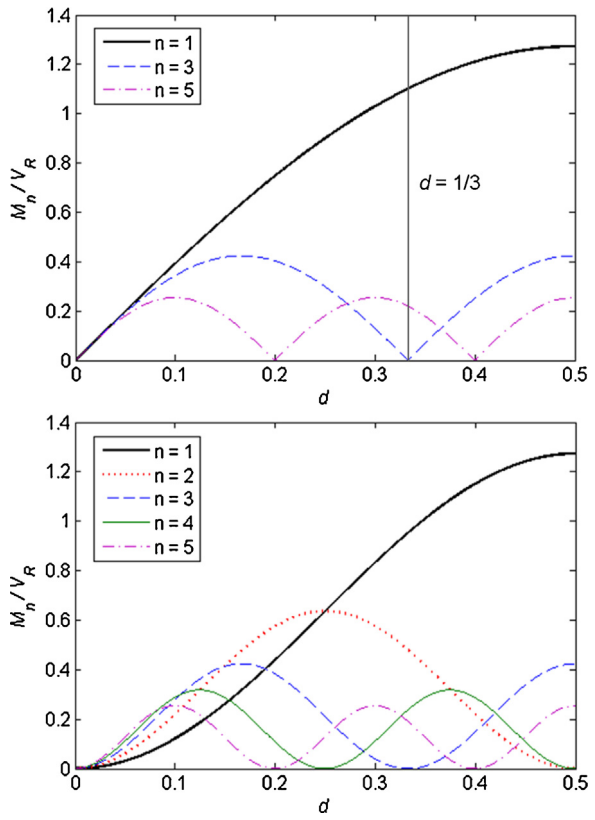

Fig. 3. Normalised magnitudes of the Fourier components M_n/V_R of the 3S-DIT with symmetric (top) and asymmetric implementation (bottom) of zero-volt levels in the time-pattern of AC component of the driving signal $f(t)$, respectively. $n=1$ (thick solid line), $n=2$ (dotted line), $n=3$ (dashed line) $n=4$ (thin solid line) and $n=5$ (dashed-dotted line). The vertical line marks the duty cycle $d=1/3$ for the symmetric implementation, which has a low ratio of higher harmonics ($M_{2-4}=0$).

[26,28]. All measurements have been performed with singly-charged argon ions, Ar^+, created by a 3 ms electron-impact ionisation of argon in an asymptotically-symmetric, hyperbolic Paul trap of size $r_0=7$ mm [29] (Fig. 4). The AC voltage, with the fixed fundamental frequency $\Omega/2\pi=1/T=450$ kHz, applied to the end-caps only, is provided by a function generator (Stanford Research Systems, DS345) and a voltage amplifier (FLC Electronics, A400DI). The DC voltage, also produced by a function generator (Stanford Research Systems, DS345), is applied to the ring electrode. This experimental scheme of voltage application does not affect the trapping parameters beside a change of sign in the a parameter (Eq. (5)). After a storage time of 50 ms, the ions are extracted from the trap by an amplitude ramp [30,31] and counted by a Channeltron detector with conversion dynode.

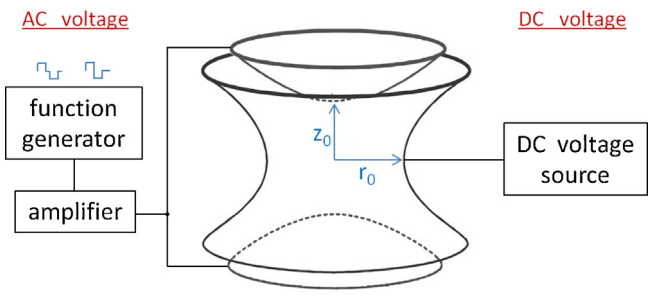

Fig. 4. Application of driving voltages to the trap electrodes.

Table 2
Magnitudes $M_{n,sym}$ of Fourier components of $f_{sym,1/3}(t)$ (Eq. (6) and Table 1).

n	$\Omega/2\pi$	M_n/V_R
1	$1/T$	$2\sqrt{3}/\pi \simeq 1.103$
2	$2/T$	0
3	$3/T$	0
4	$4/T$	0
5	$5/T$	$2\sqrt{3}/(5\pi) \simeq 0.221$

The experimental cycle (ionisation, storage, detection) has been repeated 250 times for each set of trapping parameters a and q, i.e. amplitudes U_0 and V_R, respectively. The amplitudes of the DC and AC voltages have been scanned in steps of 0.10 V and 0.19 V, respectively.

4. Results and discussion

4.1. Stability diagram of the 3S-DIT with symmetric time pattern

As a first example of operating the 3S-DIT, a driving signal with a low ratio of higher harmonics ($M_{2-4}=0$) is chosen, i.e. a driving signal with symmetric zero-volt components and a duty cycle of $d=1/3$ (compare Fig. 3). The magnitudes of the Fourier components $M_{n,sym}$ of the respective function

$$f_{sym,1/3}(t)=\begin{cases}+V_R & \text{for } nT < t \le nT+1/3T\\ 0 & \text{for } nT+1/3T < t \le nT+1/2T\\ -V_R & \text{for } nT+1/2T < t \le nT+5/6T\\ 0 & \text{for } nT+5/6T < t \le (n+1)T\end{cases} \quad (6)$$

are given in Table 2.

Fig. 5 shows a stability diagram of the 3S-DIT, with the axes being scaled by U_0 and V_R (left and bottom) and the corresponding trapping parameters a and q (right and top). For each U_0-V_R pair the number of trapped ions has been measured and is plotted normalised to the maximum number of detected ions as indicated by levels of gray on a scale from zero (white) to the maximum number (black). The predicted borders of stability [25] have been added for comparison (solid lines).

For the scaling between the AC driving signal amplitude V_R and the parameter q_z the 1st order Fourier component is used. Note, however, that the actual scaling factor ($M_n/V_R=1.100$) resulted from a Fourier transformation of the measured driving signal,

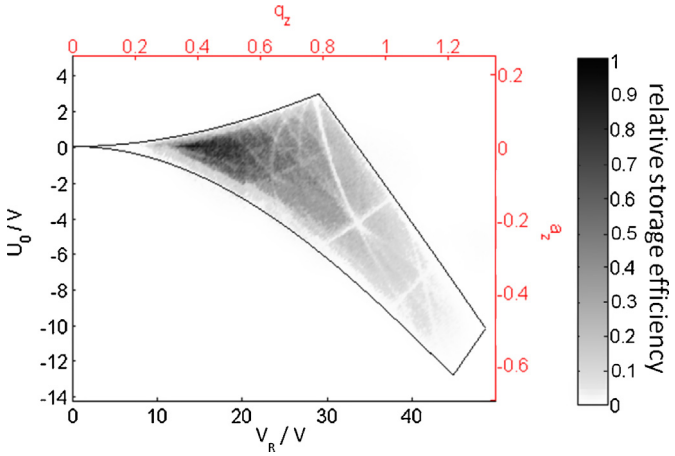

Fig. 5. Measured stability diagram of the 3S-DIT with symmetric implementation of zero-volt levels in the time-pattern of the driving signal $f(t)$ and a duty cycle of $d=1/3$, plotted as a function of driving voltages (left and bottom axes) and stability parameters (right and top axes). Solid lines represent the calculated borders of stability.

Table 3
Magnitudes $M_{n,sym}$ and $M_{n,asym}$ of Fourier components of $f_{sym,0.4}(t)$ and $f_{asym,0.4}(t)$ (Eqs. (7) and (8), Table 1).

n	$\Omega/2\pi$	$M_{n,sym}/V_R$	$M_{n,asym}/V_R$
1	$1/T$	$\frac{\sqrt{2}\sqrt{5+\sqrt{5}}}{\pi} \simeq 1.211$	$\frac{5+\sqrt{5}}{2\pi} \simeq 1.152$
2	$2/T$	0	$\frac{5-\sqrt{5}}{4\pi} \simeq 0.220$
3	$3/T$	$\frac{\sqrt{2}\sqrt{5-\sqrt{5}}}{3\pi} \simeq 0.249$	$\frac{5-\sqrt{5}}{6\pi} \simeq 0.147$
4	$4/T$	0	$\frac{5+\sqrt{5}}{8\pi} \simeq 0.288$
5	$5/T$	0	0

which deviated slightly from the calculated one. The highest storage efficiency is found for $q_z = 0.38$–0.50 and between $a_z = -0.01$ and 0.03. Comparable values have been observed previously in stability diagrams measured with a harmonically driven RF ion trap and 2S-DIT [26]. Furthermore, instability lines of comparable depths and positions are crossing the stable region of ion confinement. Here, ions gain energy out of the driving field as the sum of integer multiples of their motional frequencies equals an integer multiple of the driving field frequency. This leads to the loss of ions [32,26]. Thus, as in the case of the 2S-DIT, the $a-q$ stability diagram is practically indistinguishable from that of a harmonically driven Paul trap. For a direct comparison see reference [26].

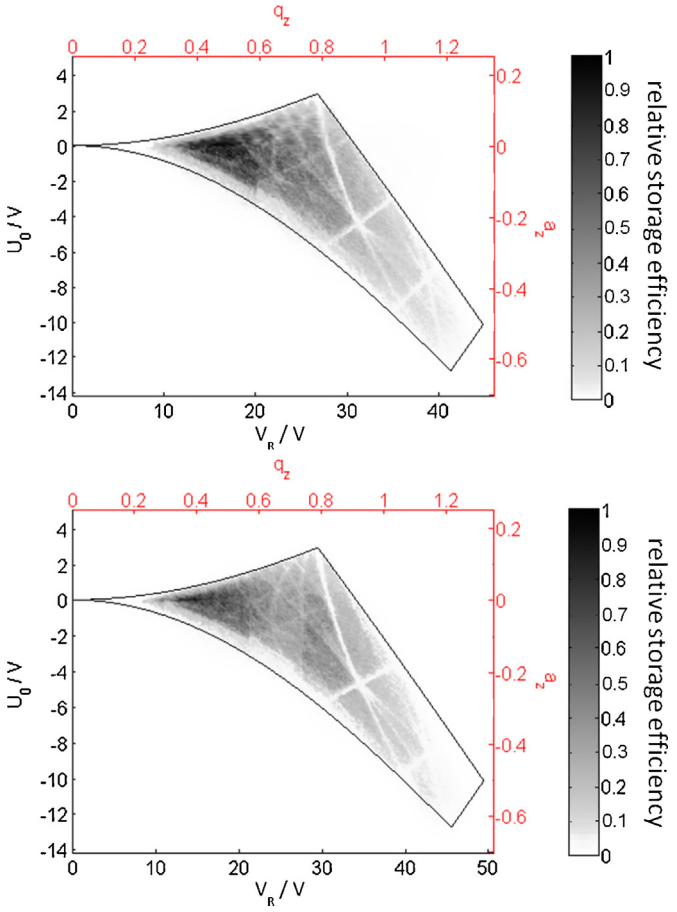

Fig. 6. Measured stability diagram of the 3S-DIT with symmetric (top) and asymmetric implementation (bottom) of zero-volt levels in the time-pattern of the driving signal $f(t)$ and a duty cycle of $d = 0.4$ plotted as a function of driving voltages (left and bottom axes) and stability parameters (right and top axes), respectively. Solid lines represent the calculated borders of stability.

4.2. Symmetric vs. asymmetric time pattern of the 3S-DIT

For comparison of 3S-DITs operated by driving signals with symmetric and asymmetric implementation of zero-volt levels (see Section 2.2), stability diagrams have been measured for both cases with a duty cycle of $d = 0.4$, where most higher-order Fourier components of the asymmetric 3S-DIT are relatively small. Their magnitudes for the respective functions

$$f_{sym,0.4}(t) = \begin{cases} +V_R & \text{for } nT < t \le nT + 0.4T \\ 0 & \text{for } nT + 0.4T < t \le nT + 0.5T \\ -V_R & \text{for } nT + 0.5T < t \le nT + 0.9T \\ 0 & \text{for } nT + 0.9T < t \le (n+1)T \end{cases} \quad (7)$$

$$f_{asym,0.4}(t) = \begin{cases} +V_R & \text{for } nT < t \le nT + 0.4T \\ -V_R & \text{for } nT + 0.4T < t \le nT + 0.8T \\ 0 & \text{for } nT + 0.8T < t \le (n+1)T \end{cases} \quad (8)$$

are given in Table 3.

In Fig. 6 the stability diagrams for the symmetric (top) and asymmetric implementation (bottom) of zero-volt potentials in the time-pattern of the driving signal are shown, respectively. Note, that in all Figs. 5 and 6, the a_z and q_z axes are scaled equally, resulting in optically identical regions of stability. But while the U_0 axis is also unchanged (Eq. (5) with $M_0 = 0$), the scaling of the V_R axis changes for different values of the duty cycle d (Figs. 5 and 6, top) as well as for different implementation of zero-volt potentials (Fig. 6, top and bottom) due to the different magnitudes of their first order Fourier component M_1 (Eq. (5), Tables 2 and 3).

The normalised magnitudes M_1/V_R, used as scaling factors in the q-parameter, are calculated to be 1.211 (symmetric) and 1.152 (asymmetric), respectively (see Table 3). The Fourier component of the actually applied signal has been measured to be 1.190 and 1.080. The reduced values M_1/V_R of the measured signals are caused by imperfections (e.g. steepness of edges) in the driving signal, generated by the voltage amplifier (compare Section 3). In any case, the impact of higher harmonics is too small to be observed in the present stability diagrams.

5. Conclusion

The 3-state digital ion trap has been introduced and investigated experimentally by mapping stability diagrams for different duty cycles and different schemes of zero-volt level implementation in the time pattern of the driving signal $f(t)$. As expected, the stability diagrams are identical in the $a_z - q_z$ plane and along the U_0 axis, but scaled differently along the V_R axis. The measured borders of stability agree well with the ones calculated from the first order Fourier components. The restriction to the driving signal assumed in this investigation, namely to define $M_0 = 0$, and the implementation of *zero*-volt periods in the time pattern of the driving signal were chosen for the specific aim of interaction studies with trapped particles. Both, the symmetric and asymmetric zero-volt implementation offer the possibility to send a beam of charged particles (electrons or ions) through the trap volume, e.g. for the study of interactions with stored ions. While the symmetric option has the advantage of a reduced number of higher harmonics in the Fourier analysis, the asymmetric implementation provides a sustained field-free period within one cycle of the driving field. To extend the study of the 3S-DIT performance to more general 3-level pattern of the driving field is out of scope of the present study. However, we expect that further pattern will be found to be useful for specific applications.

Note added in proof

After acceptance of this manuscript we learnt that related studies have been performed in another context, namely the investigation of ion-beam properties by "simulation" experiments in Paul traps. In the corresponding publications, instead of "digital ion trap" or "digital driving signal" other terms such as "pulse-excited trap" or "periodic step-function waveform" are used [33–38].

Acknowledgement

The project was supported by a Collaborative Research Center of the DFG (SFB 652-TP A03). S. Bandelow acknowledges a postgraduate stipend from the state of Mecklenburg-Vorpommern (Landesgraduiertenförderung).

References

[1] E. Illenberger, B.M. Smirnov, Electron attachment to complex molecules, High Temperature 38 (2000) 829.
[2] S. Feil, T.D. Märk, A. Mauracher, P. Scheier, C.A. Mayhew, Investigations of electron attachment to the perfluorocarbon molecules c-C_4F_8, 1,3 C_4F_6 and c-C_5F_8, International Journal of Mass Spectrometry 277 (2008) 41.
[3] R.A. Zubarev, N.L. Kelleher, F.W. McLafferty, Electron capture dissociation of multiply charged protein cations. A nonergodic process, Journal of the American Chemical Society 120 (1998) 3265.
[4] J.E.P. Syka, J.J. Coon, M.J. Schroeder, J. Shabanowitz, D.F. Hunt, Peptide and protein sequence analysis by electron transfer dissociation mass spectrometry, Proceedings of the National Academy of Sciences of the United States of America 101 (2004) 9528.
[5] D. Neff, S. Smuczynska, J. Simons, Electron shuttling in electron transfer dissociation, International Journal of Mass Spectrometry 283 (2009) 122.
[6] K.L. Krivos, P.A. Limbach, Sequence analysis of peptide: oligonucleotide heteroconjugates by electron capture dissociation and electron transfer dissociation, Journal of the American Society for Mass Spectrometry 21 (2010) 1387.
[7] H.B. Hamidane, D. Chiappe, R. Hartmer, A. Vorobyev, M. Moniatte, Y.O. Tsybin, Electron capture and transfer dissociation peptide structure analysis at different ion internal levels, Journal of the American Society for Mass Spectrometry 20 (2009) 567.
[8] S. Denifl, S. Ptasinska, M. Probst, J. Hrusak, P. Scheier, T.D. Märk, Electron attachment to the gas-phase DNA bases cytosine and thymine, Journal of Physics A 108 (2004) 6562.
[9] S. Ptasinska, S. Denifl, P. Scheier, E. Illenberger, T.D. Märk, Bond- and site-selective loss of H atoms from nucleobases by very-low energy electrons (<3 eV), Angewandte Chemie International Edition 44 (2005) 6941.
[10] B. Boudaiffa, P. Cloutier, D. Hunting, M.A. Huels, L. Sanche, Resonant formation of DNA strand breaks by low-energy (3 to 20 eV) electrons, Science 287 (2000) 1658.
[11] W. Paul, H. Steinwedel, Ein neues Massenspektrometer ohne Magnetfeld, Zeitschrift für Naturforschung 8a (1953) 448.
[12] W. Paul, O. Osberghaus, E. Fischer, Ein Ionenkäfigs, Forschungsberichte des Wirtschafts- und Verkehrsministeriums Nordrhein-Westfalen 415 (1958).
[13] P.H. Dawson, Quadrupole Mass Spectrometry and its Applications, AIP Press, Woodbury, New York, 1995.
[14] R.E. March, J.F.J. Todd, Practical Aspects of Trapped Ion Mass Spectrometry V, CRC Press, Boca Raton, Florida, 2010.
[15] L. Schweikhard, J. Ziegler, H. Bopp, K. Lützenkirchen, The trapping condition and a new instability of the ion motion in the ion cyclotron resonance trap, International Journal of Mass Spectrometry and Ion Processes 141 (1995) 77.
[16] A. Herlert, S. Krückeberg, L. Schweikhard, M. Vogel, C. Walther, First observation of doubly charged negative gold cluster ions, Physica Scripta T80 (1999) 200.
[17] A. Herlert, L. Schweikhard, Production of dianionic and trianionic noble metal clusters in a Penning trap, International Journal of Mass Spectrometry 229 (2003) 19.
[18] F. Martinez, S. Bandelow, C. Breitenfeldt, G. Marx, L. Schweikhard, F. Wienholtz, F. Ziegler, Appearance size of poly anionic aluminium clusters, Al_n^{z-}, $z = 2–5$, The European Physics Journal D 67 (2013) 39.
[19] T. Baba, Y. Hashimoto, H. Hasegawa, A. Hirabayashi, I. Waki, Electron capture dissociation in a radio frequency ion trap, Analytical Chemistry 76 (2004) 4263.
[20] X. Liang, J.W. Hager, S.A. McLuckey, Transmission mode ion/ion electron-transfer dissociation in a linear ion trap, Analytical Chemistry 79 (2007) 3363.
[21] L. Ding, F.L. Brancia, Electron capture dissociation in a digital ion trap mass spectrometer, Analytical Chemistry 78 (2006) 1995.
[22] J.A. Richards, R.M. Huey, J. Hiller, A new operating mode for the quadrupole mass filter, International Journal of Mass Spectrometry and Ion Processes 12 (1973) 317.
[23] J.A. Richards, Quadrupole mass filter spectrum control using pulse width modulation, International Journal of Mass Spectrometry and Ion Processes 24 (1977) 219.
[24] L. Ding, M. Sudakov, S. Kumashiro, A simulation study of the digital ion trap mass spectrometer, International Journal of Mass Spectrometry 221 (2002) 117.
[25] N. McLachlan, Theory and Application of Mathieu Functions, 1st ed., Oxford University Press, Oxford, 1951.
[26] S. Bandelow, G. Marx, L. Schweikhard, The stability diagram of the digital ion trap, International Journal of Mass Spectrometry 336 (2013) 47.
[27] G. Werth, V.N. Gheorghe, F.G. Major, Charged Particle Traps II, Springer-Verlag, Berlin, Heidelberg, 2009, pp. 5.
[28] S. Bandelow, G. Marx, L. Schweikhard, A split-ring Paul trap for dipolar excitation of the radial ion motion and ellipticity studies, The European Physics Journal D 61 (2011) 315.
[29] R.D. Knight, The general form of the quadrupole ion trap potential, International Journal of Mass Spectrometry and Ion Processes 51 (1983) 127.
[30] R.L. Alfred, F.A. Londry, R.A. March, Resonance excitation of ions stored in a quadrupole ion trap. Part IV. Theory of quadrupolar excitation, International Journal of Mass Spectrometry and Ion Processes 125 (1993) 171.
[31] D.E. Goeringer, R.I. Crutcher, S.A. McLuckey, Ion remeasurement in the radio frequency quadrupole ion trap, Analytical Chemistry 67 (1995) 4164.
[32] R. Alheit, S. Kleineidam, F. Vedel, M. Vedel, G. Werth, Higher order non-linear resonances in a Paul trap, International Journal of Mass Spectrometry and Ion Processes 154 (1996) 155.
[33] R.C. Davidson, H. Qin, G. Shvets, A Paul trap configuration to simulate intense non-neutral beam propagation over large distances through a periodic focusing quadrupole magnetic field, Physics of Plasmas 7 (2000) 1020.
[34] N. Kjærgaard, M. Drewsen, Crystalline beam emulations in a puls-excited linear Paul trap, Physics of Plasmas 8 (2001) 1371.
[35] N. Kjærgaard, K. Mølhave, M. Drewsen, Stability of Coulomb crystals in a linear Paul trap with storage-ring-like confinement, Physical Review E 66 (2002) 015401(R).
[36] R. Takai, K. Ito, Y. Iwashita, H. Okamoto, S. Taniguchi, Y. Tomita, Design and fabrication of a linear Paul trap for the study of space-charge-dominated beams, Nuclear Instruments and Methods in Physical Research Section A 532 (2004) 508.
[37] E.P. Gilson, R.C. Davidson, P.C. Efthimion, R. Majeski, Pault Trap Simulator Experiment to model intense-beam propagation in alternating-gradient transport systems, Physical Review Letters 92 (2004) 155002.
[38] E.P. Gilson, R.C. Davidson, M. Dorf, P.C. Efthimion, R. Majeski, M. Chung, M.S. Gutierrez, A.N. Kabcenell, Studies of emittance growth and halo particle production in intense charged particle beams using the Paul Trap Simulator Experiment, Physics of Plasmas 17 (2010) 056707.

Article IV

Hyperfine Interact (2015) 236:19–27
DOI 10.1007/s10751-015-1194-0

Electron attachment to anionic clusters in ion traps

Franklin Martinez[1] · Steffi Bandelow[2] · Gerrit Marx[2] · Lutz Schweikhard[2] · Albert Vass[2]

Published online: 28 May 2015

Abstract Ion traps are versatile tools for the investigation of gas-phase cluster ions, allowing, e.g., cluster-size selection and extended reaction times. Taking advantage of their particular storage capability of simultaneous trapping of electrons and clusters, Penning traps have been applied for the production of clusters with high negative charge states. Recently, linear radio-frequency quadrupole traps have been demonstrated to be another candidate to produce polyanionic clusters. Operation with rectangular, rather than harmonic, radio-frequency voltages provides field-free time slots for unhindered electron passage through the trap. Several aspects of electron-attachment techniques by means of Penning and radio-frequency traps are addressed and recent experimental results are presented.

Keywords Polyanions · Metal clusters · Penning trap · Radio-frequency trap · Digital ion trap

1 Introduction

Multiply negatively charged atoms, molecules and clusters in the gas phase have been subject to experimental and theoretical investigation for a long time [1–3]. For example, doubly charged anions of carbon and metal clusters were produced either in ion sources by sputtering [4], laser ablation [5–7], and electrospray ionization [8], or by electron-transfer reactions [9, 10], and in crossed-beam experiments [11]. While also tri-anionic lead clusters were

Proceedings of the 6th International Conference on Trapped Charged Particles and Fundamental Physics (TCP 2014), Takamatsu, Japan, 1–5 December 2014.

✉ Franklin Martinez
franklin.martinez@uni-rostock.de

[1] Institute of Physics, University of Rostock, Rostock, Germany

[2] Institute of Physics, Ernst-Moritz-Arndt University, Greifswald, Germany

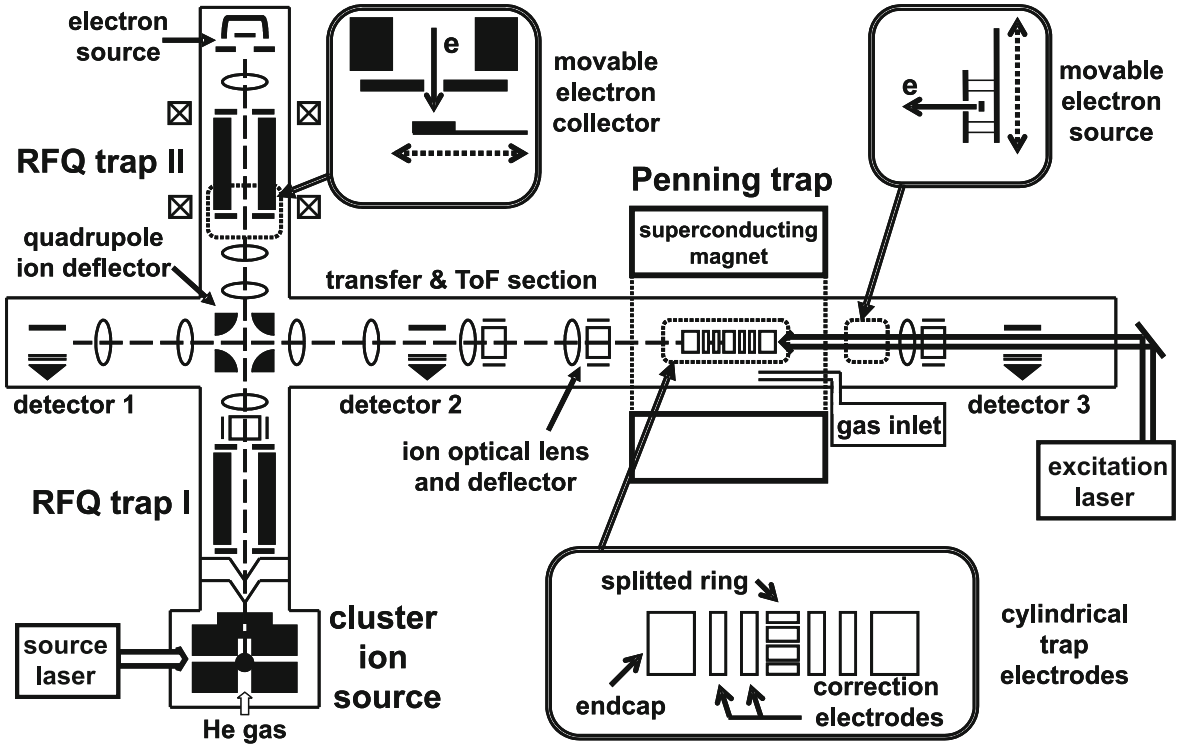

Fig. 1 Schematic of the present ClusterTrap setup, with cluster ion source, RFQ traps and Penning trap. Details of the electron collector at the RFQ trap II, of the cylindrical Penning trap, and of the electron source at the Penning trap are shown in insets

observed by laser ablation [7], even higher charge states have been produced of gold and of aluminum clusters by their simultaneous storage with electrons inside a Penning trap [12–18]. Recently, production of di- and trianionic gold clusters in a linear radio-frequency quadrupole (RFQ) trap has been demonstrated by exposing stored monoanions to an electron beam [16, 17]. In the present report, methods for electron attachment to trapped cluster anions are characterized for both Penning and RFQ traps. Gold cluster dianions have been produced in an RFQ trap that has been operated in a digital-ion-trap (DIT) mode [19–22], including field free time-periods [23].

2 Experimental setup

The experiments have been performed at the ClusterTrap, a setup designed for production and investigation of gas-phase cluster ions [17, 24–26]. For the present studies, metal clusters have been produced by laser irradiation of a metal wire and subsequent expansion of the vapor into vacuum by means of a helium gas pulse [27]. By variation of the laser and gas-pulse parameters, the cluster distribution is shifted with respect to the cluster size, i.e. the number of atoms. Of the neutral and singly charged clusters produced in the source, the mono-anionic ones are captured and accumulated in a linear radio-frequency quadrupole ion trap (RFQ trap I in Fig. 1). After ejection from this trap, they are guided by an electrostatic quadrupole deflector and other ion-optical elements into a 12-T cylindrical Penning trap (inset in Fig. 1) [17, 24]. During in-flight capture and storage, cluster ions are mass-over-charge selected and exposed to interaction steps of interest. The latter involve an electron beam from a movable, heated rhenium filament (inset in Fig. 1), and a laser beam with pulse durations in the nanosecond range. Charged reaction products remain stored and are

subsequently analyzed by time-of-flight (ToF) mass spectrometry, for the present study by ejection from the Penning trap and drift to detector 1 (Fig. 1).

In an alternative experimental sequence, cluster monoanions accumulated in RFQ trap I are transferred into another linear ion trap (RFQ trap II, Fig. 1), which is particularly designed and equipped for the investigation of polyanion production in a radio-frequency trap [17]. The heated filament of a small, cut-open halogen lamp is located behind the RFQ trap II and provides an electron beam along the trap axis, which can be monitored by a movable electron collector plate (inset in Fig. 1). For unhindered passage of electrons through the RFQ trap II, it is operated as a three-state digital ion trap [23], i.e. the radio-frequency voltage is realized by well-tailored, fast (kHz) switching between three electric potentials, instead of the usual harmonic voltage signals. One of the three potential steps corresponds to zero-volt potential differences between the RFQ rods, i.e. few-microsecond intervals of a field-free trap volume [23]. The passage of the electron beam is supported by a low magnetic field of about 20 mT, orientated parallel to the trap axis. It is provided by two induction coils located outside the vacuum vessel (Fig. 1).

3 Electron attachment in RFQ trap II

Production of polyanionic metal clusters in a linear radio-frequency trap is realized by attachment of electrons to stored cluster monoanions. For this purpose, an electron beam is guided along the trap axis during the field-free time slots of the digital radio-frequency trapping voltage, i.e. the clusters are exposed to a sequence of microsecond electron-beam pulses.

From the many collisions between cluster anions and electrons, only some will result in the attachment of an electron, i.e. in the increase of the negative charge state of the cluster. However, this will be the case only if the cluster is large enough to accept and (meta-)stably bind another electron [3, 13, 18, 28]. The relative yield of polyanionic clusters is mainly determined by the electron energy during the interaction process. For very high electron energies, a collision might result in ”kicking out” an electron from the anionic cluster, i.e. electron loss, rather than electron attachment. However, for attachment, the approaching electron has to overcome the repulsing Coulomb potential of the already negatively charged cluster, i.e. it has to exceed a minimum energy value. The Coulomb-barrier height, and hence the required electron energy, increases with the negative charge state of the cluster. Thus, the energy distribution of the incident electron beam is crucial not only for the yield of polyanionic clusters, but also for the reachable charge state. Note, that a more technical criterion, due to the trapping conditions, may limit the reachable charge state even stronger: while some higher charge state might be produced by electron attachment, the mass-over-charge ratio of the resulting cluster polyanion may prevent it from being further trapped, i.e. in the present experimental setup those clusters are lost from the RFQ-trap before being detected. This is different from the Penning trap where there is no lower storage limit of the mass-over-charge range.

The energy of the attaching electrons is to first order approximated by the difference between the filament floating potential and the offset potential of the ion trap, assuming the stored clusters are cooled into the axial trapping well, e.g. by application of buffer gas. Then, the mean energy is easily controlled by varying the filament float potential. However, the width of the electron-energy distribution depends on the type of electron source. In the present case of a resistively heated filament, it is determined by the voltage drop between both ends of the filament, caused by the heating current. Figure 2 shows the emitted current

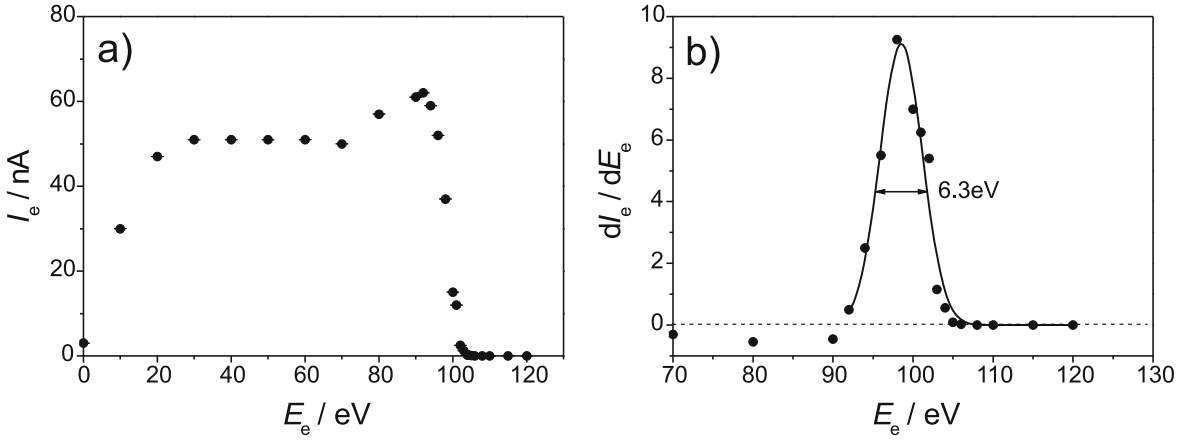

Fig. 2 **a** Electron current I_e emitted from a heated filament source as a function of the electron energy E_e. **b** The derivative dI_e/dE_e reflects the distribution of the electron energy (*symbols*), and is fitted with a Gaussian function (*solid line*) yielding a mean energy of 98.5 eV and a FWHM of 6.3 eV

of such a type of filament electron source as a function of the electron energy. The latter is determined by a blocking potential applied to a grid in front of an electron collector. (Note, that this analysis has been realized in a separate setup, i.e. without the RFQ trap II.) From the derivative of the measured current, the full width at half maximum of the energy distribution is determined to be about 6 eV, while the energy width at the base level reflects the voltage drop along the filament of about 10 eV.

It is planned for future experiments to determine the Coulomb potential height for a given cluster size and charge state by measuring the yield of ions with the next higher charge state as a function of electron energy. However, such a task requires energy distributions in the few meV range to resolve, e.g., the potential heights of clusters with the same charge state, but with different sizes. Respective electron-energy distributions may be obtained either by more suitable types of electron sources, e.g. indirectly heated ones, or by combining the present source with an electron energy selector with meV-resolving power.

In particular low-energy electrons are easily diverted from their initial direction of motion by weak electric fields. However, at the same time they are well guided by magnetic fields low enough to keep the motion of atomic ions, let alone of cluster ions, undisturbed. The magnetic field superimposed on the RFQ trap II [17] has been analyzed prior to installation of the induction coils at the ClusterTrap setup. The axial magnetic field inside the vacuum vessel (but under atmospheric pressure) has been measured by use of a Hall probe (Fig. 3a). The two circular coils produce maxima of the magnetic field strength close to the positions where the electrons enter and leave the trapping volume through holes in the endcaps (EC1 and EC2 in Fig. 3a). Between the endcaps the field strength drops to about 80 % of the maximum, still sufficient to guide the electrons.

After installation of the coils at the setup, the electron current through the trap has been monitored as a function of magnetic field strength B (Fig. 3b) by means of the movable collector located between the electrostatic ion deflector and the RFQ trap II (Fig. 1). While no electron current is detected behind the trap without any magnetic field, about 30 μA are measured for $B = 20$ mT.

In recent experiments, electron attachment in the RFQ trap II operated in the 2-state DIT mode (Fig. 4a), i.e. without field-free time intervals in the RF-signal, had been realized. As a result, production of gold cluster di- and trianions [16], as well as combined polyanion production with attachment first in the RFQ and then in the Penning trap, has been demonstrated [17].

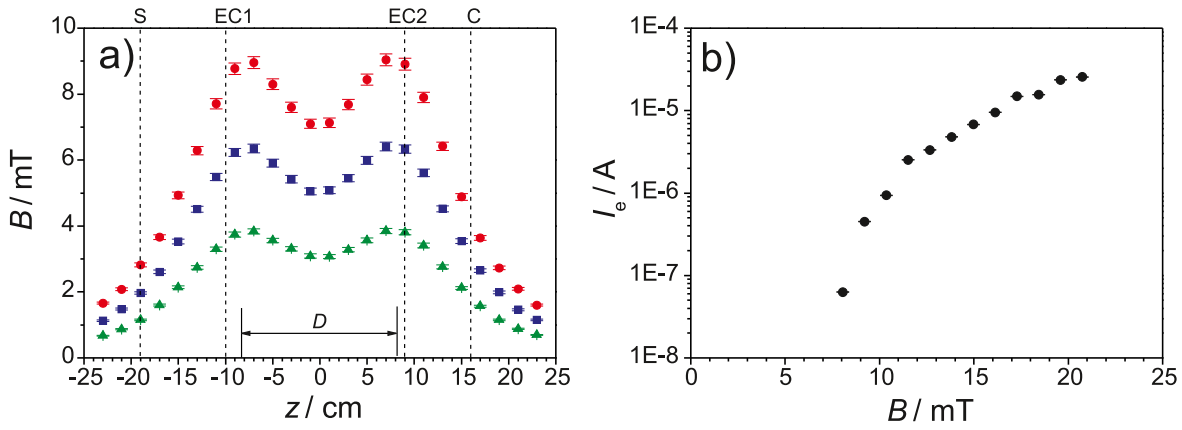

Fig. 3 **a** Magnetic field inductivity B as a function of the z-position along the axis of RFQ trap II for different coil currents (1.4A/24.5V red circles; 1.0A/17.4V blue squares; 0.6A/10.4V green triangles). The coil separation D=16.5 mm and the positions of trap endcaps (EC), electron source (S) and electron collector (C) are indicated. **b** Current on the electron collector (C) at the RFQ trap II (without application of an RF-field) as a function of the applied magnetic field

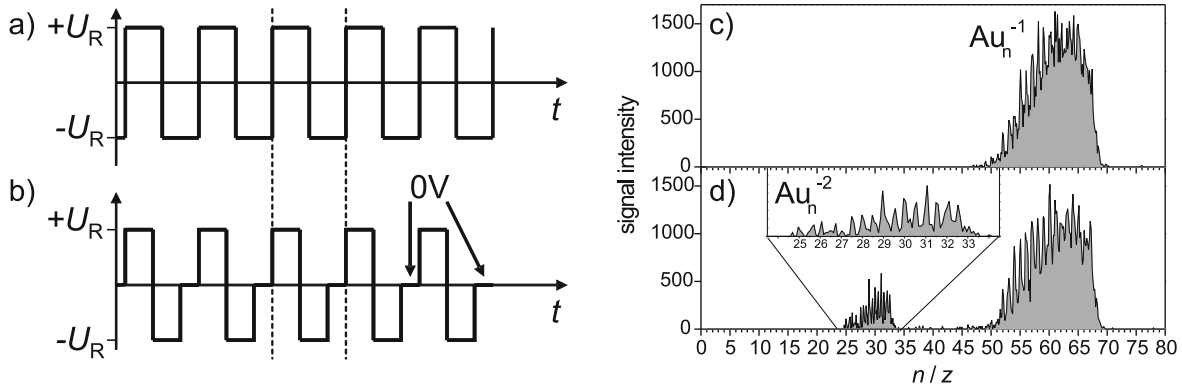

Fig. 4 **a**-**b** Schematic of the rectangular radio-frequency potential of a 2-state (**a**), and of a 3-state digital ion trap (**b**) with a duty cycle of 0.4 [23], i.e. 20 % of the period are at 0-V level. **c**-**d** Mass-spectra of gold clusters after accumulation in RFQ trap I, transfer to RFQ trap II and irradiation with an electron-beam, transfer to the Penning trap and ejection from there towards detector 1. **c** Reference spectrum of monoanions Au_n^{-1} (n = 50 to 70) stored for 2.6 s in RFQ trap II operated in the 3-state DIT-mode (f_R = 65 kHz, U_R = 70 V), without application of an electron-beam. **d** Dianions Au_n^{-2} produced after exposing the gold monoanions to 17-eV electron pulses of 2 μs duration over a period of 20,000 RF-cycles

Production of dianionic gold clusters in the RFQ trap II operated in the 3-state DIT mode (Fig. 4b) has been realized for the first time. Gold cluster monoanions, Au_n^{-1}, produced by the cluster source were trapped in the RFQ trap II for 2.6 s (Fig. 4c). Application of electron pulses of 2 μs duration over about 20,000 RF-cycles (i.e. total interaction time of 40 ms) results in the appearance of dianionic gold clusters, Au_n^{-2}, in the spectrum (Fig. 4d). The inset shows signals at half integers of the size-over-charge ratio n/z due to the negative charge state $z = 2$. While the previous experiments with the 2-state DIT required an electron energy of several electronvolts to traverse the RFQ trap, the application of the 3-state DIT with intermediate field-free time periods prepares experiments for electron attachment with sub-electronvolt energies.

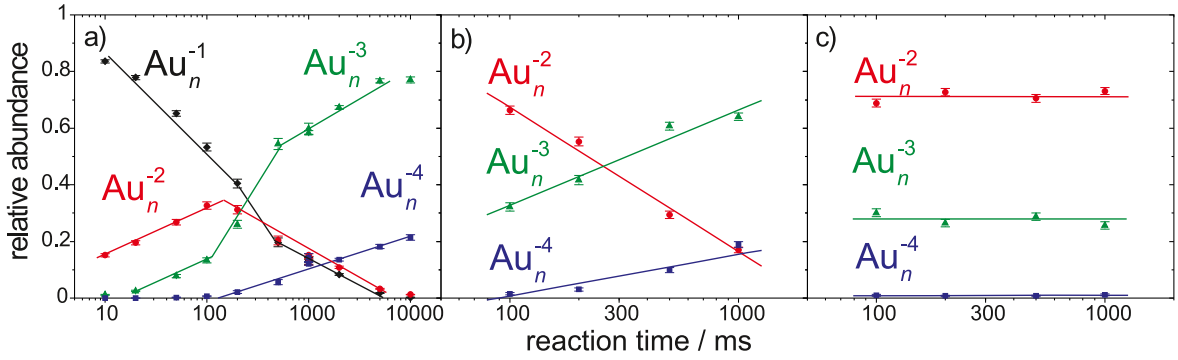

Fig. 5 **a** Relative abundance of gold anions Au_n^{-z}, $n = 127 \pm 15$, $z = 1 - 4$, as a function of the reaction time in the Penning trap, after application of an electron beam for 20 ms. **b-c** Relative abundance of gold polyanions, Au_n^{-z}, $n = 135 \pm 15$, $z = 2 - 4$, as a function of storage time, after application of an electron beam for 20 ms, without (**b**) and with removal of electrons (**c**) after a reaction time of 100 ms by pulsing the endcap electrodes for 1 μs. The *lines* are included to guide the eyes

4 Electron attachment in a Penning trap

First production of gas-phase polyanionic metal clusters in a 5-T Penning ion trap was reported for di- and tri-anions of gold, silver and titan [3, 12, 13, 29]. Later, di-, tri-, tetra-, and penta-anions of aluminum clusters were observed [14, 15, 30, 31]. With the recent upgrade of the ClusterTrap setup to a 12-T Penning trap, higher charge states for gold clusters have been reported, reaching from tetra- up to hexa-anions [17, 18]. Electron attachment in the Penning trap is realized by the electron-bath technique, i.e. the simultaneous trapping of cluster monoanions and electrons [12]. In short, during the storage of cluster monoanions, an electron beam and argon gas are simultaneously pulsed into the trap volume. Low-energy secondary electrons are produced by electron-impact ionization of argon gas atoms and remain trapped, while the argon cations and the high-energy primary electrons leave the trap. During a reaction time of typically 1 s polyanionic clusters are formed and remain stored until they are extracted and analyzed.

Besides the cluster-size criterion [3, 13, 18, 28], the maximum charge state and the relative yields of the polyanionic species are to some extent controlled by the trapping potential depth, which limits the energy of trapped electrons [14, 31–34], and by the reaction time [31, 34] as shown for the case of gold clusters (Fig. 5a). While the distribution is dominated by dianions and non-converted monoanions after 10 ms, those species disappear after a few seconds in favor of tri- and tetra-anions. For application of further experimental steps on a given charge-state distribution, the reaction time is intentionally terminated by removing the stored electrons from the trap without affecting the stored cluster anions. It is realized by a 1-μs pulsing of the endcap electrodes (Fig. 5b-c), a technique known as suspended trapping [35, 36]. Thus, lifetime measurements on meta-stable polyanionic clusters may become feasible.

In the present setup, the electron source, made of a resistively heated stripe of rhenium foil, is mounted on a horizontally movable support and is located just outside the 12-T superconducting magnet, i.e. in the region of a strong magnetic-field gradient. Thus, electrons are guided close to the axis of the Penning trap, even if they are emitted from an off-axis position, as monitored by the production of polyanionic gold clusters (Fig. 6a). Thus, production and subsequent laser excitation of polyanionic clusters [34, 37–39] can be combined in an experimental sequence, where the electron beam and the laser beam enter the trap from the

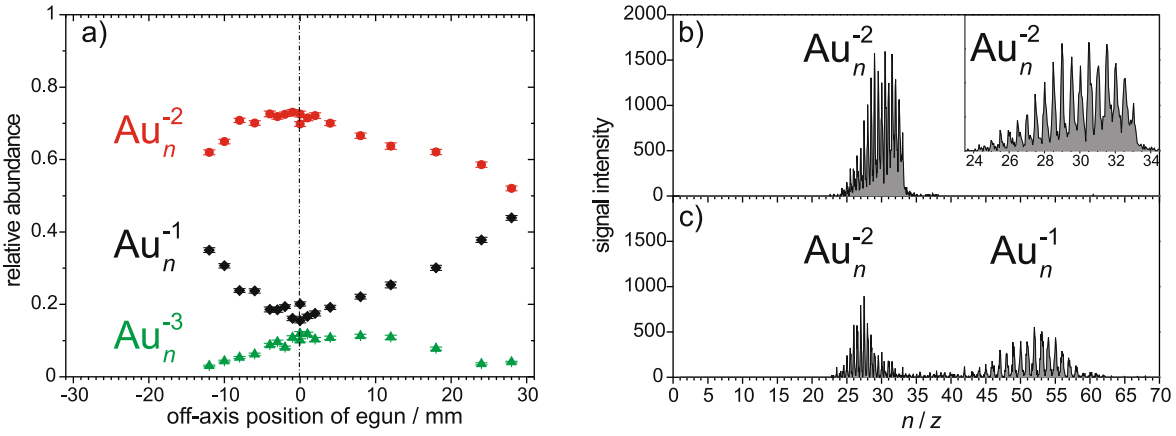

Fig. 6 **a** Relative yield of gold cluster polyanions (Au_n^{-z}, $n = 64 \pm 8$, $z = 1 - 3$) as a function of the radial filament position relative to the Penning trap axis. **b** ToF-spectrum of gold cluster dianions (Au_n^{-2}, $n = 48 - 68$) as produced in the RFQ II trap and subsequently stored in the Penning trap for 10 s. The distribution shows signals at full and at half-integer values of n/z due to the dianionic charge state $z = 2$ (inset). **c** ToF-spectrum of gold cluster anions after laser excitation of the dianions for 5 s (Nd:YAG laser, 532 nm, 30 Hz, 5 ns, 2.67 mJ). Monoanions are produced by photo-activated electron emission from the dianions

same side of the magnet, leaving the other side available for undisturbed cluster capture and time-of-flight analysis (Fig. 1) [17].

An example for laser excitation of gold cluster dianions is shown in Fig. 6. Here, the dianions were produced in the RFQ trap II prior to transfer into and storage in the Penning trap (Fig. 6b). After application of a pulsed Nd:YAG laser (repetition rate 30 Hz, wavelength 532 nm, pulse energy 2.67 mJ) for 5 s, monoanions are formed by electron emission from the dianions (Fig. 6c). Note that, in general, there is a size-dependent decay-pathway competition of electron emission and neutral-atom evaporation for dianions as well as further (possibly multiple) decay of the monoanions [37, 39]. In order to disentangle the details of the decay sequences, future experiments will include size and charge-state separation prior to the laser irradiation.

5 Summary and outlook

Different aspects of electron attachment to clusters in ion traps have been discussed with respect to polyanion production. Recent studies in a linear radio-frequency trap have been extended to the 3-state digital ion trap. This mode includes time slots with zero voltage between the RFQ rods, i.e. electrons encounter a field-free trapping volume. Thus, polyanion production with well-controlled low-energetic electrons will provide means for studying the repulsive Coulomb potential of negatively charged metal clusters.

While simultaneous storage of cluster monoanions and electrons in a Penning trap results in the formation of polyanionic clusters, the controlled removal of electrons from the trap will allow future lifetime studies of meta-stable polyanionic species. Moreover, an electron source located off the trap axis still provides an electron beam close to this axis due to the presence of the magnetic field of the Penning trap. Thus, the limited access to the trap volume inside the bore of the superconducting magnet remains available for application of, e.g., a laser beam.

Experimental results on gold clusters for polyanion production in both types of traps have been presented. In conclusion, ion traps are versatile and flexible tools for the investigation of size-selective metal clusters, in particular for studies on formation and stability of polyanions.

Acknowledgments The project was supported by the Collaborative Research Center of the DFG (SFB 652, TP A03). F. Martinez and S. Bandelow acknowledge postgraduate stipends from the state of Mecklenburg-Vorpommern (Landesgraduiertenförderung) in the framework of the International Max Planck Research School on Bounded Plasmas.

References

1. Scheller, M.K., Compton, R.N., Cederbaum, L.S.: Gas-phase multiply charged anions. Science **270**, 1160–1166 (1995)
2. Wang, X.-B., Wang, L.-S.: Experimental search for the smallest stable multiply charged anions in the gas phase. Phys. Rev. Lett. **83**, 3402–3405 (1999)
3. Yannouleas, C., Landman, U., Herlert, A., Schweikhard, L.: Multiply charged metal cluster anions. Phys. Rev. Lett. **86**, 2996–2999 (2001)
4. Schauer, S.N., Williams, P., Compton, R.N.: Production of small doubly charged negative carbon cluster ions by sputtering. Phys. Rev. Lett. **65**, 625–628 (1990)
5. Limbach, P.A., Schweikhard, L., Cowen, K.A., McDermott, M.T., Marshall, A.G., Coe, J.V.: Observation of the Doubly Charged Gas-Phase Fullerene Anions C_{60}^{2-} and C_{70}^{2-}. J. Am. Chem. Soc. **113**, 6795–6798 (1991)
6. Hettich, R.L., Compton, R.N., Ritchie, R.H.: Doubly charged negative ions of carbon C-60. Phys. Rev. Lett. **67**, 1242–1245 (1991)
7. Stoermer, C., Friedrich, J., Kappes, M.M.: Observation of Multiply Charged Cluster Anions upon Pulsed UV Laser Ablation of Metal Surfaces under High Vacuum. Int. J. Mass Spectrom. **206**, 63–78 (2001)
8. Hampe, O., Neumaier, M., Blom, M.N., Kappes, M.M.: On the generation and stability of isolated doubly negatively charged fullerenes. Chem. Phys. Lett. **354**, 303–309 (2002)
9. Liu, B., Hvelplund, P., Brøndsted Nielsen, S., Tomita, S.: Formation of C_{60}^{2-} dianions in collisions between C_{60}^{-} and Na atoms. Phys. Rev. Lett. **92**, 168301 (2004)
10. Hvelplund, P., Liu, B., Brøndsted Nielsen, S., Tomita, S.: Formation of higher-order fullerene dianions in collisions with Na atoms. Eur. Phys. J. D **43**, 133–136 (2007)
11. Hartig, J., Blom, M.N., Hampe, O., Kappes, M.M.: Electron attachment to negative fullerene ions: A fourier transform mass spectrometric study. Int. J. Mass Spectrom. **229**, 93–98 (2003)
12. Herlert, A., Krückeberg, S., Schweikhard, L., Vogel, M., Walther, C.: First observation of doubly charged negative gold cluster ions. Phys. Scr. T **80**, 200–202 (1999)
13. Schweikhard, L., Herlert, A., Krückeberg, S., Vogel, M., Walther, C.: Electronic effects in the production of small dianionic gold clusters by electron attachment on to stored Au_n^-, $n = 12 - 28$. Philos. Mag. B **79**, 1343–1352 (1999)
14. Walsh, N., Martinez, F., Marx, G., Schweikhard, L., Ziegler, F.: First observation of a tetra-anionic metal cluster, Al_n^{4-}. J. Chem. Phys. **132**, 014308–8 (2010)
15. Martinez, F., Bandelow, S., Breitenfeldt, C., Marx, G., Schweikhard, L., Wienholtz, F., Ziegler, F.: Appearance Size of Poly-Anionic Aluminum Clusters, Al_n^{z-}, $z = 2 - 5$. Eur. J. Phys. D **67**, 39–8 (2013)
16. Martinez, F., Bandelow, S., Marx, G., Schweikhard, L.: Production of multiply-charged metal-cluster anions in Penning and radio-frequency traps. AIP Conf. Proc. **1521**, 230–239 (2013)
17. Martinez, F., Bandelow, S., Breitenfeldt, C., Marx, G., Schweikhard, L., Vass, A., Wienholtz, F.: Upgrades at ClusterTrap and latest results. Int. J. Mass Spectrom. **365–366**, 266–274 (2014)
18. Martinez, F., Bandelow, S., Marx, G., Schweikhard, L., Vass, A.: Abundances of Tetra-, Penta- and Hexa-Anionic Gold Clusters. J. Phys. Chem. C (2015). doi:10.1021/jp510947p
19. Richards, J.A., Huey, R.M., Hiller, J.: On the time varying potential in the quadrupole mass spectrometer. Proc. IREE Aust. **32**, 321–322 (1971)
20. Richards, J.A., Huey, R.M., Hiller, J.: A new operating mode for the quadrupole mass filter. Int. J. Mass Spectrom. Ion Process. **12**, 317–339 (1973)
21. Ding, L., Sudakov, M., Kumashiro, S.: A simulation study of the digital ion trap mass spectrometer. Int. J. Mass Spectrom. **221**, 117–138 (2002)

22. Bandelow, S., Marx, G., Schweikhard, L.: The stability diagram of the digital ion trap. Int. J. Mass Spectrom. **336**, 47–52 (2013)
23. Bandelow, S., Marx, G., Schweikhard, L.: The 3-state digital ion trap. Int. J. Mass Spectrom. **353**, 49–53 (2013)
24. Martinez, F., Marx, G., Schweikhard, L., Vass, A., Ziegler, F.: The new ClusterTrap setup. Eur. Phys. J. D **63**, 255–262 (2011)
25. Schweikhard, L., Hansen, K., Herlert, A., Marx, G., Vogel, M.: New approaches to stored cluster ions. The determination of dissociation energies and recent studies on dianionic metal clusters. Eur. Phys. J. D **24**, 137–143 (2003)
26. Schweikhard, L., Krückeberg, S., Lützenkirchen, K., Walther, C.: The Mainz Cluster Trap. Eur. Phys. J. D **9**, 15–20 (1999)
27. Weidele, H., Frenzel, U., Leisner, T., Kreisle, D.: Production of "cold/hot" metal cluster ions: A modified laser vaporization source. Z. Phys. D **20**, 411–412 (1991)
28. Seidl, M., Perdew, J.P., Brajczewska, M., Fiolhais, C.: Ionization energy and electron affinity of a metal cluster in the stabilized jellium model: Size effect and charging limit. J. Chem. Phys. **108**, 8182–8189 (1998)
29. Herlert, A., Hansen, K., Schweikhard, L., Vogel, M.: Multiply charged titanium cluster anions: Production and photodetachment. Hyp. Int. **127**, 529–532 (2000)
30. Walsh, N., Martinez, F., Marx, G., Schweikhard, L., Ziegler, F.: Multiply negatively charged aluminium clusters II. Production of Al_n^{3-}. Eur. Phys. J. D **52**, 27–30 (2009)
31. Walsh, N., Martinez, F., Marx, G., Schweikhard, L.: Multiply negatively charged aluminium clusters. Production of Al_n^{2-} in a Penning trap. Eur. Phys. J. D **43**, 241–245 (2007)
32. Herlert, A., Jertz, R., Alonso Otamendi, J., Gonzalez Martinez, A.J., Schweikhard, L.: The influence of the trapping potential on the attachment of a second electron to stored metal cluster and fullerene anions. Int. J. Mass Spectrom. **218**, 217–225 (2002)
33. Martinez, F., Bandelow, S., Breitenfeldt, C., Marx, G., Schweikhard, L., Wienholtz, F., Ziegler, F.: Lifting of the trapping potential during ion storage for multi-anion production in a Penning trap. Int. J. Mass Spectrom. **313**, 30–35 (2012)
34. Walsh, N., Herlert, A., Martinez, F., Marx, G., Schweikhard, L.: Atomic clusters in a Penning trap: Investigation of their properties and utilization as diagnostic tools. J. Phys. B **42**, 154024-10 (2009)
35. Laude, D.A., Beu, S.C.: Suspended trapping pulse sequence for simplified mass calibration in Fourier transform mass spectrometry. Anal. Chem. **61**, 2422–2427 (1989)
36. Cooper, B.T., Buckner, S.W.: Simplified electron ejection in Fourier transform ion cyclotron resonance mass spectrometry by suspended trapping. Org. Mass Spectrom. **28**, 914–918 (1993)
37. Schweikhard, L., Hansen, K., Herlert, A., Herráiz Lablanca, M.D., Marx, G., Vogel, M.: Laser investigations of stored metal cluster ions. Hyp. Int. **146/147**, 275–281 (2003)
38. Herlert, A., Schweikhard, L.: First observation of delayed electron emission from dianionic metal clusters. Int. J. Mass Spectrom. **252**, 151–156 (2006)
39. Herlert, A., Schweikhard, L.: Two-electron emission after photoexcitation of metal-cluster dianions. New J. Phys. **14**, 055015-24 (2012)

9 Publications

2022

Production of polyanionic aluminium clusters with up to 10 excess electrons
S. Bandelow, F. Martinez, S. König, L. Schweikhard, *Int. J. Mass Spectrom.* **473**, 116780 (2022)

2020

Photodissociation of mono- and di-anionic tin clusters
M. Wolfram, S. Bandelow, A. Jankowski, S. König, G. Marx, L. Schweikhard, *Eur. Phys. J. D* **74**, 135 (2020)

2018

Interaction of anionic tin clusters Sn_n^-, $n = 7 - 75$, with electrons: Polyanion production and cluster decay
S. König, M. Wolfram, S. Bandelow, G. Marx, L. Schweikhard, *Eur. Phys. J. D* **72**, 153 (2018)

Disentangling the photodissociation pathways of small lead clusters by time-resolved monitoring of their delayed decays: The case of Pb_{31}^+
M. Wolfram, S. König, S. Bandelow, P. Fischer, A. Jankowski, G. Marx, L. Schweikhard, *J. Phys. B* **51**, 044005 (2018)

2017

Interaction of anionic lead clusters Pb_n^-, $n = 10, 12 - 102$, with electrons - polyanion production and cluster decay
S. König, S. Bandelow, L. Schweikhard, M. Wolfram, *Int. J. Mass Spectrom.* **421**, 129-134 (2017)

2015

Electron Attachment to Anionic Clusters in Ion Traps
F. Martinez, S. Bandelow, G. Marx, L. Schweikhard, A. Vass, *Hyperfine Interact.* **236**, 19-27 (2015)

Abundances of Tetra-, Penta- and Hexa-Anionic Gold Clusters
F. Martinez, S. Bandelow, G. Marx, L. Schweikhard, A. Vass, *J. Phys. Chem. C* **119**, 10949-10957 (2015)

2014

Upgrades at ClusterTrap and latest results
F. Martinez, S. Bandelow, C. Breitenfeldt, G. Marx, L. Schweikhard, A. Vass, F. Wienholtz, *Int. J. Mass Spectrom.* **365-366**, 266-274 (2014)

2013

The stability diagram of the digital ion trap
S. Bandelow, G. Marx, L. Schweikhard, *Int. J. Mass Spectrom.*, **336**, 47-52 (2013)

The 3-state digital ion trap
S. Bandelow, G. Marx, L. Schweikhard, *Int. J. Mass Spectrom.*, **353**, 49-53 (2013)

Production of Multiply-Charged Metal-Cluster Anions in Penning and Radio-Frequency Traps
F. Martinez, S. Bandelow, G. Marx, L. Schweikhard, *NON-NEUTRAL PLASMA PHYSICS VIII, AIP Conf. Proc.* **1521**, 230-239 (2013)

Appearance size of poly-anionic aluminium clusters, Al_n^{z-}, $z = 2 - 5$
F. Martinez, S. Bandelow, C. Breitenfeldt, G. Marx, L. Schweikhard, F. Wienholtz, F. Ziegler, *Eur. Phys. J. D* **67**(2), 39 (2013)

2012

Lifting of the trapping potential during ion storage for multi-anion production in a Penning trap
F. Martinez, S. Bandelow, C. Breitenfeldt, G. Marx, L. Schweikhard, F. Wienholtz, F. Ziegler, *Int. J. Mass Spectrom.* **313**, 30-35 (2012)

2011

A split-ring Paul trap for dipolar excitation of the radial ion motion and ellipticity studies
S. Bandelow, G. Marx, L. Schweikhard, *Eur. Phys. J. D*, **61**(2), 315-320 (2011)

Eigenständigkeitserklärung

Hiermit erkläre ich, dass diese Arbeit bisher von mir weder an der Mathematisch - Naturwissenschaftlichen Fakultät der Universität Greifswald noch einer anderen wissenschaftlichen Einrichtung zum Zwecke der Promotion eingereicht wurde.

Ferner erkläre ich, dass ich diese Arbeit selbständig verfasst und keine anderen als die darin angegebenen Hilfsmittel und Hilfen benutzt und keine Textabschnitte eines Dritten ohne Kennzeichnung übernommen habe.